Title

Constraining Dark Matter and Dark Energy Models using Astrophysical Surveys

Permalink

https://escholarship.org/uc/item/2806n8qq

Author

Cieplak, Agnieszka M.

Publication Date

2013

Peer reviewed|Thesis/dissertation

UNIVERSITY OF CALIFORNIA, SAN DIEGO

**Constraining Dark Matter and Dark Energy Models using
Astrophysical Surveys**

A dissertation submitted in partial satisfaction of the
requirements for the degree
Doctor of Philosophy

in

Physics

by

Agnieszka M. Cieplak

Committee in charge:

    Professor Kim Griest, Chair
    Professor Michael Norman
    Professor Adam Burgasser
    Professor Dariusz Stramski
    Professor Bruce Driver

2013

The dissertation of Agnieszka M. Cieplak is approved, and it is acceptable in quality and form for publication on microfilm and electronically:

_____

_____

_____

_____

_____
Chair

University of California, San Diego

2013

DEDICATION

To my dad, who was the first to teach me about atoms and the twin paradox,

who taught me that there is more to the world than what the eye can see.

To my mom, for her love and inspiration, and her example in always striving

forward.

To my brother, for his constant support.

And to Michael, for his love and support, for always being by my side, my source

of strength and joy.

The important thing is not to stop questioning. Curiosity has its own reason for existing. One cannot help but be in awe when he contemplates the mysteries of eternity, of life, of the marvelous structure of reality. It is enough if one tried merely to comprehend a little of this mystery every day. Never lose a holy curiosity.

- Albert Einstein

TABLE OF CONTENTS

LIST OF FIGURES

LIST OF TABLES

NOMENCLATURE

Microlensing Symbols

G	gravitational constant
c	speed of light
M	mass of lens
R_*	radius of source star
T_{eff}	effective temperature of the source star
L	distance to the source star
x	ratio of the distance to the lens to the distance to the star
x_{max}	maximum x to which the lens is detectable
A_{ps}	magnification in the point-source model
A_{fs}	magnification in the finite-source model
A_{limb}	magnification in the limb-darkened model
A_{thresh}	threshold magnification for detection
A_{max}	maximum magnification
b	impact parameter of lens
r_{E}	Einstein ring radius
u	impact parameter in terms of r_{E}
u_{thresh}	u when the magnification is equal to A_{thresh}
u_{min}	u at closest approach of the lens to the line of sight
U_*	projected star radius in terms of r_{E}
t_0	time at closest approach of the lens to the line of sight
t_{E}	time it takes the lens to cross r_{E}
$\hat{t}$	time it takes for the lens to cross the projected star radius
t_{event}	duration of the microlensing event
v_{t}	velocity of the lens transverse to the line of sight
v_{c}	the circular velocity of the Sun
ρ	local dark matter density
I_{b}	linear limb-darkening profile
u_λ	linear limb-darkening coefficient
Γ	rate of detection
τ	optical depth
N_{exp}	number of expected microlensing events

Cosmology Symbols

a	scale factor of the universe (with the present value $a_0 = 1$)
t	cosmic time
z	redshift: $z = a_0/a - 1$
d_A	angular diameter distance
H	Hubble parameter: $H = \dot{a}/a$
H_0	present Hubble parameter
ρ	energy density
P	pressure
w	equation of state: $w = P/\rho$
K	curvature of the universe
Ω	density parameter at the present epoch ($z = 0$)
c_s	sound speed
r_s	sound horizon
T	temperature
k	comoving wavenumber
$P(k)$	power spectrum of perturbations
r	comoving scale
$\xi(r)$	correlation function of perturbations
δ	density contrast
b	bias (ratio of flux to total matter perturbations)
β	redshift space distortion parameter

Lyman-Alpha Forest Symbols

v	peculiar velocity of absorbing atom projected along the line of sight
$P(v)$	velocity distribution of absorbing atoms
σ	velocity dispersion
b	Doppler parameter: $b = \sqrt{2}\sigma$
k_{B}	Boltzmann constant
m	mass of an absorbing atom
ν	photon frequency
$L(\nu)$	Lorentzian absorption profile
$V(\nu)$	Voigt line profile
τ	optical depth
n_{HI}	proper number density of the HI gas
$\sigma_{Ly\alpha}$	Lyman-alpha absorption cross section
F	observed flux: $F = e^{-\tau}$
α_{H+}	recombination rate coefficient
$\Gamma_{\gamma,HI}$	photoionization rate
Γ	polytropic index
A_{21}	spontaneous transition coefficient

ACKNOWLEDGEMENTS

<div align="center">VITA</div>

2008	B.S., *cum laude* in Physics (*Major*) and Chemistry (*Minor*), University of California, San Diego
2010	M. S. in Physics, University of California, San Diego
2013	Ph. D. in Physics, University of California, San Diego

<div align="center">PUBLICATIONS</div>

A. M. Cieplak, K. Griest, Improved Theoretical Predictions of Microlensing Rates for the Detection of Primordial Black Hole Dark Matter, The Astrophysical Journal 767, 145 (2013)

K. Griest, M. J. Lehner, **A. M. Cieplak**, and Bhuvnesh Jain, Microlensing of Kepler Stars as a Method of Detecting Primordial Black Hole Dark Matter, Phys. Rev. Lett. 107, 231101 (2011).

Wozniak, S. B., D. Stramski, M. Stramska, R. A. Reynolds, V. M. Wright, E. Y. Miksic, M. Cichocka, and **A. M. Cieplak** (2010), Optical variability of seawater in relation to particle concentration, composition, and size distribution in the nearshore marine environment at Imperial Beach, California, J. Geophys. Res., 115, C08027, doi:10.1029/2009JC005554.

Stramska, M., D. Stramski, M. Cichocka, **A. Cieplak**, and S. B. Wozniak (2008), Effects of atmospheric particles from Southern California on the optical properties of seawater, J. Geophys. Res., 113, C08037, doi10.1029/2007JC004407.

ABSTRACT OF THE DISSERTATION

Constraining Dark Matter and Dark Energy Models using Astrophysical Surveys

by

Agnieszka M. Cieplak

Doctor of Philosophy in Physics

University of California, San Diego, 2013

Professor Kim Griest, Chair

This thesis addresses astrophysical probes to constrain dark matter (DM) and dark energy models. Primordial black holes (PBHs) remain one of the few DM candidates within the Standard Model of Particle Physics. This thesis presents a new probe of this PBH DM, using the microlensing of the source stars monitored by the already existing Kepler satellite. With its photometric precision and the large projected cross section of the nearby stars, it is found that previous constraints on PBH DM could theoretically be extended by two orders of magnitude. Correcting a well-known microlensing formula, a limb-darkening analysis is included, and a new approximation is calculated for future star selection. A preliminary prediction is calculated for the planned Wide-Field Infrared Survey Telescope.

A preliminary study of the first two years of publicly available Kepler data is presented. The investigation yields many new sources of background error not predicted in the theoretical calculations, such as stellar flares and comets in the field of view. Since no PBH candidates are detected, an efficiency of detection is therefore calculated by running a Monte Carlo with fake limb-darkened finite-source microlensing events. It is found that with just the first 8 quarters of data, a full order of magnitude of the PBH mass range can be already constrained.

Finally, one of the astrophysical probes of dark energy is also addressed - specifically, the baryon acoustic oscillations (BAO) measurement in the gas distribution, as detected in quasar absorption lines. This unique measurement of dark energy at intermediate redshifts is being measured by current telescope surveys. The last part of this thesis therefore focuses on understanding the systematic effects in such a detection. Since the bias between the underlying dark matter distribution and the measured gas flux distribution is based on gas physics, hydrodynamic simulations are used to understand the evolution of neutral hydrogen over time. It is found the location of the peak is a dependable measurement, but more robust simulations will have to be run for a full understanding of the shape and size of the peak.

Chapter 1

Introduction

The mathematical description of cosmology, the study of the origins of the Universe, was first enabled by the introduction of General Relativity by Albert Einstein (1917). Linking the energy density of matter to the space-time geometry, it was realized that his theory could be applied as a description of the Universe as a whole. Friedmann (1922) and Lemaître (1927) wrote down the solutions to Einstein's equations for both a static and expanding universe. However, it was the discovery by Hubble (1929) of an expanding Universe that kickstarted observational cosmology. Measuring recession velocities of galaxies, he discovered that their velocities were linearly related to their distances, thus demonstrating that the Universe is in fact expanding, and not static. Building on these discoveries, Alpher et al. (1948) suggested that since the Universe is now expanding, it should have been denser and hotter at earlier times, thus allowing for the right conditions for primordial nucleosynthesis to occur. They therefore suggested that chemical elements were created in the early Universe, and the residual heat should be visible as a background radiation. This in fact was discovered, by Penzias & Wilson (1965) as a background microwave radiation, called the cosmic microwave background (CMB). There were a few surprises with this measurement, one of which was the fact that the CMB was very isotropic, suggesting that different regions of the Universe, now separated by large distances, were in fact in causal contact at earlier times. This prompted Guth (1981) to suggest the concept of inflation, where the Universe underwent a period of rapid expansion before the photons decoupled from

the background matter to form the CMB, therefore ensuring causal contact at very early times.

The question of course arises how the first structure would have formed from this isotropic background. Sachs & Wolfe (1967), Harrison (1970) and Zeldovich (1972) predicted, based on the measurements of structure at the time, that there should be initial density perturbations in the plasma which is probed by the CMB, with an amplitude that is the same on all scales. This scale-invariant spectrum is also close to that predicted by the theory of inflation, in which quantum fluctuations of an underlying scalar field give rise to density perturbations in the primordial plasma (Guth & Pi, 1982). These fluctuations should then grow into the structure of the Universe that we see today. Since these initial perturbations in the CMB were predicted to be very small, they were not discovered until COBE measured the CMB temperature with great precision, detecting temperature variations of one part in 10,000 (Smoot et al., 1992). These temperature maps have since been measured to even better precision by WMAP (Bennett et al., 2012; Hinshaw et al., 2012), and most recently, by Planck (Planck Collaboration et al., 2013).

However, with these measurements of the primordial perturbations, it was realized that if the initial perturbations were due to baryonic matter only, they would not have enough time to grow over the age of the Universe into the structures we see today. This was a further confirmation of already existing measurements of the local galactic motions, which were pointing to the possibility that there is some unknown matter in the Universe that is unaccounted for, and cannot be explained with just visible matter. Zwicky (1933) first suggested that there is some form of "dark matter" after measuring galaxy velocity dispersions in the Coma cluster. He found that in order to explain the motions of the galaxies in the cluster, he would have to add 400 times more matter than what was visible. Since then the presence of such "dark matter" has been confirmed from various observations, such as rotation curves in spiral galaxies, stellar motions in the Milky Way, or gravitational lensing. Furthermore, measurements of Big Bang nucleosynthesis have constrained the matter to be nonbaryonic, not made of ordinary atomic matter. During this

nucleosynthesis most of the baryonic mass was in the form of protons and neutrons, which were taking part in this process of forming deuterium, helium, and lithium. The amount of these primordial elements measured infers the total baryonic mass at the time of nucleosynthesis, which, according to observations, is well below that needed to account for the dark matter.

If the initial quantum fluctuations of the Universe form a primordial plasma with overdensities in dark matter, radiation, and baryonic matter, the dark matter can decouple from the photons much earlier than baryonic matter. Its overdensities can therefore grow much earlier, providing for dark matter halos into which baryonic matter can fall into at later times, allowing for faster structure formation. Statistical measurements of structure in the Universe constrain the thermal velocities of the dark matter particles at the time of their decoupling, since their free streaming length has to be small enough to allow for growth of overdensities on galactic scales (warm dark matter and cold dark matter) or smaller (cold dark matter).

In addition, to explain the rate of structure formation, cosmological simulations point to an extra density component which is dominant at later times, causing a late acceleration of the Universe. The detection of this late-time acceleration by measuring supernovae at various distances has resulted in the Nobel prize awarded to two competing teams (Riess et al., 1998; Perlmutter et al., 1999). This additional energy density causing this acceleration is what is known as dark energy.

The resulting current cosmology paradigm is therefore the ΛCDM model in which the dark energy accounts for 68% of the energy content of the Universe, cold dark matter for 27%, and baryonic matter for 5% (Planck Collaboration et al., 2013).

The goal of this thesis is to address the nature of the hidden component, the dark matter and dark energy sectors, of the energy composition of the Universe.

1.1   Outline of Dissertation

In Chapters 2 and 3, I first address predictions and preliminary constraints for a dark matter candidate that is the only candidate of the Standard Model of Particle Physics - Primordial Black Holes (PBHs). Unlike other dark matter candidates, they do not require the invention of a new particle, and they would be produced in the early Universe, before the time probed by nucleosynthesis limits. They could therefore be dark matter composed of radiation and baryons, and escape the nucleosynthesis limits described above. Although much effort has been put into the search for new particle dark matter candidates, we find that we can look for PBHs with an already existing satellite, not needing additional resources. The description of this new method to look for PBHs, as well as some preliminary constraints, are the topics of Chapter 2 and Chapter 3.

In Chapter 4 I address the major component of the energy content of the Universe that is still unknown - the dark energy. In particular I look into the possible systematic effects of an important method of measuring the rate of expansion of the Universe. This method uses matter distribution statistics to understand how this acceleration has changed over time. Using the gas distribution of neutral hydrogen through the measurement of absorption lines allows us to probe further back in time, between the time that is measured by the CMB, and the time that is probed by galaxy distributions locally. However, there is much to be understood in the physics of this gas evolution, and the possible systematic effects that could possibly limit these measurements are the topic of Chapter 4.

References

Alpher, R. A., Bethe, H., & Gamow, G. 1948, Physical Review, 73, 803

Bennett, C. L., Larson, D., Weiland, J. L., Jarosik, N., Hinshaw, G., Odegard, N., Smith, K. M., Hill, R. S., Gold, B., Halpern, M., Komatsu, E., Nolta, M. R., Page, L., Spergel, D. N., Wollack, E., Dunkley, J., Kogut, A., Limon, M., Meyer, S. S., Tucker, G. S., & Wright, E. L. 2012, ArXiv e-prints

Cieplak, A. M. & Griest, K. 2013, The Astrophysical Journal, 767, 145

Einstein, A. 1917, Sitzungsberichte der Königlich Preußischen Akademie der Wissenschaften (Berlin), Seite 142-152., 142

Friedmann, A. 1922, Zeitschrift fur Physik, 10, 377

Griest, K., Lehner, M. J., Cieplak, A. M., & Jain, B. 2011, Physical Review Letters, 107, 231101 (Paper I)

Guth, A. H. 1981, Physical Review D, 23, 347

Guth, A. H. & Pi, S.-Y. 1982, Physical Review Letters, 49, 1110

Harrison, E. R. 1970, Physical Review D, 1, 2726

Hinshaw, G., Larson, D., Komatsu, E., Spergel, D. N., Bennett, C. L., Dunkley, J., Nolta, M. R., Halpern, M., Hill, R. S., Odegard, N., Page, L., Smith, K. M., Weiland, J. L., Gold, B., Jarosik, N., Kogut, A., Limon, M., Meyer, S. S., Tucker, G. S., Wollack, E., & Wright, E. L. 2012, ArXiv e-prints

Hubble, E. 1929, Proceedings of the National Academy of Science, 15, 168

Lemaître, G. 1927, Annales de la Societe Scietifique de Bruxelles, 47, 49

Penzias, A. A. & Wilson, R. W. 1965, The Astrophysical Journal, 142, 419

Perlmutter, S., Aldering, G., Goldhaber, G., Knop, R. A., Nugent, P., Castro, P. G., Deustua, S., Fabbro, S., Goobar, A., Groom, D. E., Hook, I. M., Kim, A. G., Kim, M. Y., Lee, J. C., Nunes, N. J., Pain, R., Pennypacker, C. R.,

Quimby, R., Lidman, C., Ellis, R. S., Irwin, M., McMahon, R. G., Ruiz-Lapuente, P., Walton, N., Schaefer, B., Boyle, B. J., Filippenko, A. V., Matheson, T., Fruchter, A. S., Panagia, N., Newberg, H. J. M., Couch, W. J., & Supernova Cosmology Project. 1999, The Astrophysical Journal, 517, 565

Planck Collaboration, Ade, P. A. R., Aghanim, N., Armitage-Caplan, C., Arnaud, M., Ashdown, M., Atrio-Barandela, F., Aumont, J., Baccigalupi, C., Banday, A. J., & et al. 2013, ArXiv e-prints

Riess, A. G., Filippenko, A. V., Challis, P., Clocchiatti, A., Diercks, A., Garnavich, P. M., Gilliland, R. L., Hogan, C. J., Jha, S., Kirshner, R. P., Leibundgut, B., Phillips, M. M., Reiss, D., Schmidt, B. P., Schommer, R. A., Smith, R. C., Spyromilio, J., Stubbs, C., Suntzeff, N. B., & Tonry, J. 1998, The Astronomical Journal, 116, 1009

Sachs, R. K. & Wolfe, A. M. 1967, The Astrophysical Journal, 147, 73

Smoot, G. F., Bennett, C. L., Kogut, A., Wright, E. L., Aymon, J., Boggess, N. W., Cheng, E. S., de Amici, G., Gulkis, S., Hauser, M. G., Hinshaw, G., Jackson, P. D., Janssen, M., Kaita, E., Kelsall, T., Keegstra, P., Lineweaver, C., Loewenstein, K., Lubin, P., Mather, J., Meyer, S. S., Moseley, S. H., Murdock, T., Rokke, L., Silverberg, R. F., Tenorio, L., Weiss, R., & Wilkinson, D. T. 1992, The Astrophysical Journal Letters, 396, L1

Zeldovich, Y. B. 1972, Monthly Notices of the Royal Astronomical Society, 160, 1P

Zwicky, F. 1933, Helvetica Physica Acta, 6, 110

Chapter 2

Improved Theoretical Predictions of Microlensing Rates for the Detection of Primordial Black Hole Dark Matter

2.1   Introduction

Dark Matter (DM) has been the topic of extensive research and remains one of the long standing mysteries in cosmology. Recent technological developments have aided the search for DM particle candidates (Feng, 2010) with little success, so increased attention is now focused on closing the window of one of the few DM candidates left in the Standard Model of particle physics - primordial black holes (PBHs) (Frampton et al., 2010; Carr et al., 2010). As opposed to regular black holes, PBHs are much smaller and would only be able to form during the early universe, when perturbations could collapse to form stable PBHs whose mass would be on the order of the mass of the horizon at the time of their collapse. PBHs can form due to density fluctuations during different inflation scenarios, such as double

inflation (Frampton et al., 2010), as well as due to phase transitions in the early universe causing a soft equation of state, bubble collisions, collapse of cosmic loops, or domain walls (Khlopov, 2010). First proposed by Zel'dovich & Novikov (1966) and Hawking (1971), PBHs would form during the radiation-dominated era, and therefore would be non-baryonic, satisfying the big bang nucelosynthesis limits on baryons, and would thus be classified as cold dark matter in agreement with the current paradigm.

The discovery of Hawking evaporation (Hawking, 1974, 1975), led to a theoretical lower limit on their mass scale of $5 \times 10^{-19} M_\odot$, with any black holes smaller than this having evaporated by the current age of the Universe. There are no theoretical limits on the rest of the mass range, however higher masses have been progressively ruled out by various experiments (Carr et al., 2010) (Alcock et al., 1998), leaving one major unconstrained window left, covering $5 \times 10^{-14} M_\odot$ to $2 \times 10^{-8} M_\odot$. The lower mass end of this window is set due to femtolensing observations of gamma-ray bursts (see Barnacka et al. (2012) for a recent analysis of the Fermi Gamma-ray Burst Monitor data), while the higher mass end is constrained by the combined MACHO/EROS results due to microlensing (Alcock et al., 1998). Kesden & Hanasoge (2011) recently suggested that this unconstrained mass range could be addressed by using stars as seismic detectors of PBHs passing through them, while Luo et al. (2012) proposed a mechanism to search for PBHs transiting near Earth by studying Earth's seismic waves. In Griest et al. (2011, hereafter Paper I), we proposed to extend the previous microlensing constraints into this mass range by using the NASA Kepler satellite, which has the capability to close a significant part of the window.

The Kepler satellite is a 1 m aperture telescope with a 115 deg^2 field-of-view in an Earth trailing heliocentric orbit (see Koch et al. (2010); Borucki et al. (2010) for a description of the Kepler mission). It takes photometric measurements of around 150,000 stars every 30 minutes in the Cygnus-Lyra region. The telescope was launched in March 2009 and the mission has recently been extended to the

year 2016. With planet-finding as its main science interest, it measures changes in stellar flux down to one part in a thousand or lower. This proves very beneficial in microlensing searches as well, where flux magnification is measured in the stellar light curves.

Here we fill in details and expand on our previous analysis of this exciting possibility, analyzing the importance of limb-darkening on tightening our constraints, as well as calculating the probability for various lens parameters if any events are detected. We also improve our numerical estimate over the previous use of a 5000 star sample, by including all the third quarter Kepler stars being monitored ($\sim$156,000 stars), and project this as representative of the majority of the mission. We introduce new notation for the limb-darkened microlensing curves, which will be used to fit any future observed events. We correct an error in a well-known finite-source limb-darkening microlensing formula and derive a limb-darkened microlensing detection efficiency in our framework. Finally, we show that the PBH DM mass window can be extended further to lower masses using this improved analysis, and provide an approximation which can be used to predict microlensing rates in future surveys, such as the planned WFIRST space mission.

2.2 Formulas

2.2.1 Point-Source Microlensing

Paczynski (1986) first proposed microlensing as a way to search for DM in the Milky Way. In doing so, he assumed a point-source, point-lens model, in which a lens, such as a PBH, would cause a magnification of this source when crossing in front of it, described by

$$A_{\mathrm{ps}} = \frac{u^2 + 2}{u\sqrt{u^2 + 4}} \tag{2.1}$$

where $u = b/r_{\mathrm{E}}$ and b is the impact parameter of the lens, that is the transverse

distance between the lens and the line-of-sight to the source. The Einstein ring radius $r_{\rm E}$ is given by

$$r_{\rm E} = \sqrt{\frac{4GMLx(1-x)}{c^2}} \qquad (2.2)$$

where x is the ratio of the lens distance to the source distance, L is the distance to the source star, and M is the mass of the lens. As the PBH passes in front of the star, the amplitude becomes time-dependent, $A(t) = A[u(t)]$, and

$$u(t) = \left\{ u_{\rm min}^2 + \left[\frac{2(t-t_0)}{t_{\rm E}} \right]^2 \right\}^{1/2}. \qquad (2.3)$$

Here t_0 is the time of the peak magnification, $u_{\rm min} = u(t_0)$, and $t_{\rm E} = 2r_{\rm E}/v_{\rm t}$ is the time for a lens to cross the Einstein ring with a velocity $v_{\rm t}$ transverse to the line of sight (see Figure 2.1 for an example light curve).
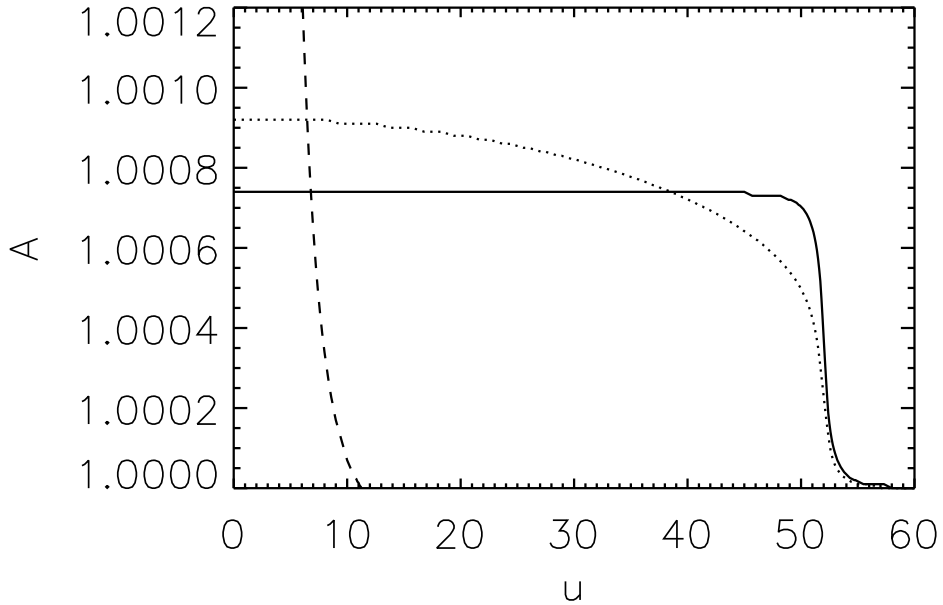
Figure 2.1 An example microlensing light curve for the three microlensing models: point-source (dashed line), finite-source with $U_* = 52$ (solid line), and finite-source with limb-darkening with $U_* = 52$ and $u_\lambda = 0.6$ (dotted line), plotted in terms of the impact parameter u.

This is the standard point-source limit, in which the lens produces a 34 percent magnification when it is within one Einstein radius of the projected source star. This approximation is valid for a source that is much smaller than the Einstein radius and is not directly aligned with the lens. However, for the relatively nearby Kepler source stars and the relative low mass PBHs, the projected star radius needs to be taken into account.

2.2.2   Finite-Source Microlensing

When the projection of the radius of the star is comparable to the lens impact parameter, one needs to take into account finite-source effects on the detectability of events. The projected star radius is given by

$$U_* = \frac{R_* x}{r_{\rm E}(x)},$$ (2.4)

where R_* is the radius of the source star. For a constant surface brightness, equation 2.1 now becomes (Witt & Mao, 1994, eqns 9-11)

$$A_{\rm fs}(U_*) = \frac{2}{\pi U_*} + \frac{1 + U_*^2}{U_*^2}\left(\frac{1}{2} + \frac{1}{\pi}\arcsin\frac{U_*^2 - 1}{U_*^2 + 1}\right)$$ (2.5)

for $u = U_*$, and

$$\begin{aligned}
A_{\rm fs}(u, U_*) = {} & \frac{2(u - U_*)^2}{\pi U_*^2 (u + U_*)}\frac{1 + U_*^2}{\sqrt{4 + (u - U_*)^2}}\Pi\left(\frac{\pi}{2}, n, k\right) \\
& + \frac{u + U_*}{2\pi U_*^2}\sqrt{4 + (u - U_*)^2}E\left(\frac{\pi}{2}, k\right) \\
& - \frac{u - U_*}{2\pi U_*^2}\frac{8 + (u^2 - U_*^2)}{\sqrt{4 + (u - U_*)^2}}F\left(\frac{\pi}{2}, k\right)
\end{aligned}$$ (2.6)

for $u \neq U_*$, where

$$n = \frac{4uU_*}{(u + U_*)^2}$$ (2.7)

and

$$k = \sqrt{\frac{4n}{4 + (u - U_*)^2}}.$$ (2.8)

F, E, and Π are elliptic integrals of the first, second, and third kind. As opposed to the point-source approximation, there is now a maximum amplitude for the magnification, which is equal to (Witt & Mao, 1994, eqn 13)

$$A_{\mathrm{max_{fs}}} = \frac{\sqrt{4 + U_*^2}}{U_*}. \tag{2.9}$$

The duration of the event t_{event} will now be the time during which the event is detectable, starting when the lens crosses the threshold impact parameter u_{thresh} at which the microlensing light curve magnification reaches the minimum detectable threshold $A_{\mathrm{thresh}} = A(u_{\mathrm{thresh}}, U_*)$ (see Figure 2.2). The duration of the event is then described by

$$t_{\mathrm{event}} = \left(u_{\mathrm{thresh}}^2 - u_{\mathrm{min}}^2\right)^{1/2} t_{\mathrm{E}} \tag{2.10}$$

(see Figure 2.1 for an example lightcurve).
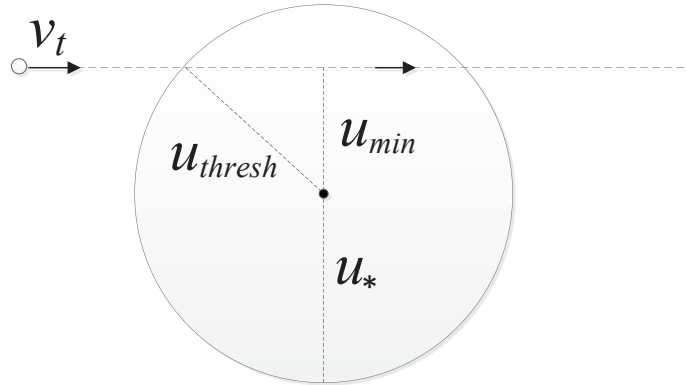
Figure 2.2 The microlensing geometry in the lens plane. A PBH with a small Einstein radius equal to r_E pictured as the small circle crosses in front of the large projected star, with a projected star radius U_*. The microlensing event is detected when the PBH's impact parameter reaches u_{thresh}. For a finite-source model this is approximately U_*, however for a limb-darkened finite-source model, this could be slightly less than U_*. The impact parameter when the PBH reaches its closest approach to the star center is labeled as u_{min}.

As the ratio of the distance to the lens to the distance to the star, x,

approaches 1, the projected star radius in terms of the Einstein radius, U_*, approaches ∞, thereby suppressing the maximum magnification $A_{\mathrm{max_{fs}}}$. Therefore there is some x_{max} beyond which $A_{\mathrm{max_{fs}}}$ is lower than the detectable magnification, A_{thresh} and no events are detected. This effect decreases the detection efficiency of the PBHs. However, the duration of the event increases, since the PBH does not have to be one Einstein radius away from the center, but from the edge of the projected star, for the beginning of a microlensing event. This effect increases the detection efficiency. As seen in Paper I, this dominates the detectability of events, increasing the number of expected microlensing events in the Kepler light curves. This finite-source model, however, assumes a constant brightness of the star, and does not take into account limb-darkening of the source star. In this paper we extend our analysis of the detectability of events to include this more physical model of the stars being lensed.

2.2.3   Finite-Source Microlensing with Limb-Darkening

For microlensing of nearby Kepler stars, where the Einstein radii of detectable PBHs is very small, limb-darkening is anticipated to be an important effect on the rate of detection. The effect is such that the star appears to be brighter towards the center, producing a more concentrated source brightness, mimicking a model in between the point-source and the finite-source approximations. The limb-darkening profile we use to study this is the linear limb-darkening described by Witt and Mao, projected into the lens plane where (Witt & Mao, 1994, eqn 15)

$$I_{\mathrm{b}}(U_*') = 1 - u_\lambda + u_\lambda \sqrt{1 - (U_*'/U_*)^2}. \tag{2.11}$$

Here, U_*' is now the distance from the center of the projected star in terms of the Einsten radius and u_λ is the linear limb-darkening coefficient. As discussed later, we also calculated results using a quadratic limb-darkened formula. Witt and Mao calculated a limb-darkened profile numerically using a weighted surface brightness

(Witt & Mao, 1994, eqn 16),

$$A_{\text{limb}}(u, U_*) = \left(\int_0^{U_*} 2\pi U_*' I_{\text{b}}(U_*') dU_*' \right)^{-1} \int_0^{U_*} \frac{\partial (A_{\text{fs}}(u, U_*')\pi U_*'^2)}{\partial U_*'} I_{\text{b}}(U_*') dU_*'. \quad (2.12)$$

The integrand in the second integral of equation 2.12 has a peak at $u = U_*'$, which causes some problems with convergence when integrating numerically. Witt and Mao provided another form of equation 2.12, (Witt & Mao, 1994, first half of eqn 16) but recommended against its use due to, they said, the presence of a singularity. We find in fact, that there is an error in their equation, due to the treatment of the integral boundaries. Integrating equation 2.12 by parts (see Appendix A.1) we find the correct magnification for a linear limb-darkened profile to be

$$A_{\text{limb}}(u, U_*) = \left(\pi U_*^2 (1 - u_\lambda/3) \right)^{-1} \times$$
$$\left[A_{\text{fs}}(u, U_*)\pi U_*^2 (1 - u_\lambda) + (\pi u_\lambda/U_*) \int_0^{U_*} A_{\text{fs}}(u, \sqrt{U_*^2 - z^2})(U_*^2 - z^2) dz \right], \quad (2.13)$$

where

$$A_{\text{fs}}(y)\pi y^2 = 2y + (1 + y^2) \left(\frac{\pi}{2} + \arcsin \frac{y^2 - 1}{y^2 + 1} \right) \quad (2.14)$$

for $u = y$, and

$$\begin{aligned} A_{\text{fs}}(u, y)\pi y^2 &= \frac{2(u - y)^2}{(u + y)} \frac{1 + y^2}{\sqrt{4 + (u - y)^2}} \Pi \left(\frac{\pi}{2}, n, k \right) \\ &+ \frac{u + y}{2} \sqrt{4 + (u - y)^2} E \left(\frac{\pi}{2}, k \right) \\ &- \frac{u - y}{2} \frac{8 + (u^2 - y^2)}{\sqrt{4 + (u - y)^2}} F \left(\frac{\pi}{2}, k \right) \end{aligned} \quad (2.15)$$

for $u \neq y$. Here $y = U_*$ or $y = \sqrt{U_*^2 - z^2}$, where appropriate in equation 2.13. Use of this equation removes the problem of numerical convergence in equation 2.12.

As stated above, the limb-darkening of the source star produces a more concentrated source brightness, thereby changing the shape of the microlensing light

curve (see Figure 2.1). There will therefore be a higher maximum magnification than that produced by a pure finite-source light curve. Agol (2002) calculated this maximum amplification for a quadratic limb-darkening model. Here we present the result for the linear limb-darkening profile using equation 2.13 when $u = 0$:

$$
\begin{aligned}
A_{\mathrm{max}} = {} & \frac{A_{\mathrm{max_{fs}}}}{1 - u_\lambda/3} \\
& \times \left\{ 1 - u_\lambda + (2u_\lambda/3U_*^2) \left[(2 + U_*^2)E\left[\sqrt{U_*^2/(4+U_*^2)}\right] \right. \right. \\
& \left. \left. \qquad\qquad\qquad - 2K\left[\sqrt{U_*^2/(4+U_*^2)}\right] \right] \right\},
\end{aligned}
\tag{2.16}
$$

where K and E are the complete elliptic integrals of the first and second kind (see Appendix A.1.1 for a derivation).

Therefore, there is a new, higher x_{max} below which the magnification is detected, allowing more PBHs to be observed. At the same time, since the brightness of the star is more concentrated, the impact parameter for which an event is detected will be closer to the projected center of the star, decreasing the duration of the event. Since this is an effect in between the point-source and finite-source model, there should be an overall decrease in the number of expected events in the Kepler data which we explore in Section 2.4. We use the linear limb-darkening model to calculate the number of expected events, as having the largest effect on this number compared to other limb-darkening models, thereby demonstrating the largest effect limb-darkening could have. The difference between the quadratic and linear limb-darkening models on the number of expected events is less than 4% for the lowest-mass PBHs explored.

2.3 Improved Numerical Estimate of Expected Number of Events using the Finite-Source Microlensing Model

In Paper I we used the finite-source microlensing model to calculate the expected number of PBH microlensing events in the Kepler data based on a subset of the third quarter light curves that were then publicly available. Here we make a more accurate estimate of this number. As in Paper I we require 4 sequential measurements of 3-sigma above average, equivalent to a microlensing event of a minimum 2 hour duration. Since the Kepler source stars are just out of the plane of the Milky Way disk, moving in almost the same direction around the Galactic center as the Sun, we assume a negligible transverse velocity between the observer and the sources. While the velocity dispersion of stars such as the Sun perpendicular to the plane of the Galaxy is on the order of 20 km/s, the expected rms velocity of the primordial black holes is 270 km/s, which is an order of magnitude higher. Since the source stars are at the same distance as the Sun from the Galactic Center, we also assume the local dark matter density $\rho_{\mathrm{DM}} \approx 0.3$ GeV cm^{-3}. The nearness of the source stars and the Kepler field being about 90° from the direction of the Galactic Center means that a model of the Galactic DM halo is not required. There is probably a factor of two uncertainty in the value of ρ_{DM} which translates directly into our possible limits. We calculate the stellar distances and the magnification thresholds A_{thresh} (below which an event would not be detected) for each star as described in Paper I. To calculate the number of expected events, we'd like to calculate the rate of detection per star-year, which can be thought of as $\Gamma = \tau / <t_{event}>$, where τ is the optical depth (the total number of PBHs inside a microlensing tube as defined in Griest (1991)) and $<t_{event}>$ is the average event duration. Since we require a minimum 2 hour event duration, we use the differential event rate (Paper I, eqn 1),

$$\frac{d\Gamma}{dt_{\text{event}}} = \frac{\rho}{M}Lv_c^2 \int_0^{x_{\text{max}}} dx\beta'^2 g(\beta') \tag{2.17}$$

where $g(\beta') = \int_0^1 dy y^{3/2}(1-y)^{-1/2}e^{-\beta'y} = \frac{\pi}{2}e^{-\beta'/2}[I_0(\beta'/2) - (1+1/\beta')I_1(\beta'/2)]$, I_0 and I_1 are modified Bessel functions of the first kind, $\beta' = 4r_E^2 u_{\text{thresh}}^2/(t_{\text{event}}^2 v_c^2)$, $y = v_t^2/(\beta'v_c^2)$, $v_c \approx 220$ km/s is the halo circular velocity, and v_t is the transverse lens velocity. Following Paper I, we use this equation for the calculation of the number of expected events for the finite-source microlensing model. However, we improve upon our Paper I calculation in several ways.

First, we extend the calculation to include the full set of third quarter light curves being monitored ($\sim$ 156,000 stars), reflecting a more accurate sample of the stars monitored during the full Kepler mission. This increases the detectable mass range predicted by one fifth order of magnitude below our previous estimate. Second, whereas before we discarded 25% of the Kepler stars as variable, irrelevant of stellar classification, we next assume a more accurate number of variable stars in the Kepler mission, with 25% of the observed dwarf stars and 95% of the observed giant stars assumed to be variable (Ciardi et al., 2011). In the sample of third quarter light curves we find about 12% of the total stars being monitored to be giant stars. With many of the giant stars being unusable, the distribution consists of mainly dwarf stars. This changes the shape of the curve, however it does not reduce the observable mass range. While the mostly discarded giant stars' peak PBH DM mass sensitivity is at around $10^{-8}M_\odot$, which dominated the earlier curve in Paper I, the dwarf stars' sensitivity is better at lower PBH masses, peaking at around $5 \times 10^{-9}M_\odot$, since a higher fraction of the stellar intensity is magnified. Therefore, discarding 95% of the giant stars does not affect our sensitivity at lower PBH masses. Finally, building upon our calculation, we scale the observation time to 7.5 years to include the extended Kepler mission, which has been approved and is already in progress. This results in a total of 780,000 star-years being observed. This final result is plotted in Figure 2.3 as the solid line. The larger amount of
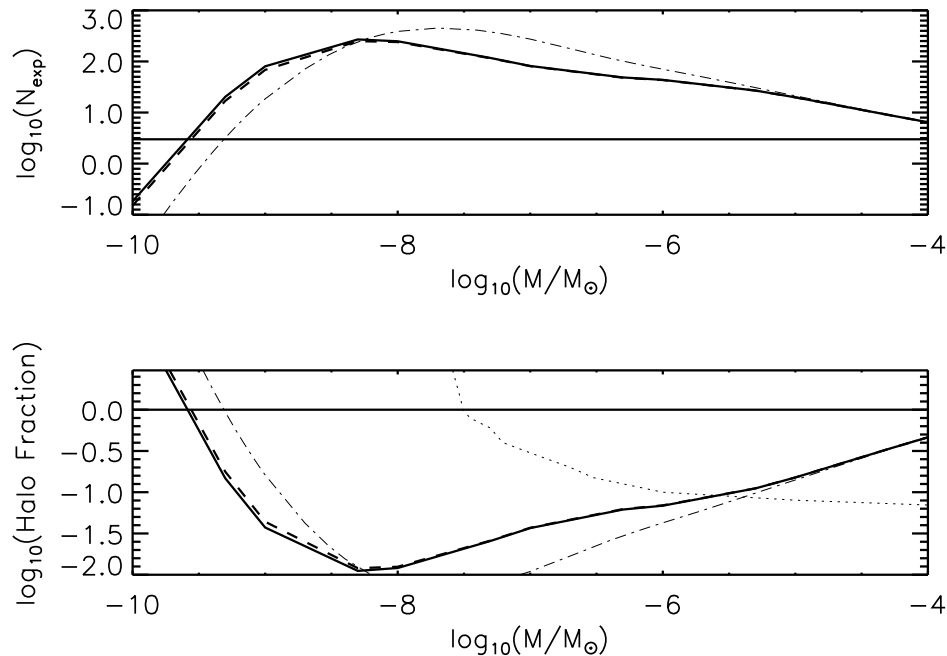
Figure 2.3 *Top panel:* Expected number of events, N_{exp}, scaled to 780,000 star-years of Kepler observing time for a finite-source microlensing model with no limb-darkening (solid line) and with limb-darkening (dashed line). We assume 4 sequential measurements with 3-sigma above average measurements of the flux. The dash-dotted line represents N_{exp} from our previous estimate of Paper I. The horizontal line shows the 95% confidence level limit if no events are detected. *Bottom panel:* The potential 95% confidence level exclusion of PBH dark matter. The area above the solid line for the finite-source model (dashed line when limb-darkening is included) would be ruled out if no events are detected in the 7.5 year Kepler observation lifetime. The dash-dotted line represents the previous estimate of Paper I, while the dotted line represents the current limits from the combined MACHO/EROS LMC microlensing surveys (Alcock et al., 1998). The horizontal line depicts a DM halo consisting entirely of PBHs.

star-years, dominated by monitoring of dwarf stars, increases the sensitivity to lower mass PBHs. This final, more accurate estimate shows a potential closing of the PBH DM window down to $2 \times 10^{-10} M_{\odot}$, compared to the 5×10^{-10} previously estimated in Paper I.

2.4 Effect of Limb Darkening on the Numerical Estimate of Expected Number of Events

In addition to these calculations, we now consider the effect of limb-darkening on the predicted number of detectable events. As seen in Section 2.2.3, limb-darkening increases $A_{\max}$, but decreases the duration of the event, since the total stellar flux remains the same. $A_{\max}$ determines $x_{\max}$, the distance to which a PBH would be detectable, with $x_{\max} = 1$ being the maximum value. A higher $A_{\max}$ would naively increase this value, increasing the range of masses that PBHs would be detectable, however, calculating $x_{\max}$ for a typical Kepler star (with radii between $0.9 R_{\odot}$ and $1.5 R_{\odot}$), without limb-darkening, one can see that $x_{\max}$ is already approaching the maximum value of 1. Therefore, increasing this further when limb-darkening is added, does not produce much of an effect on the total number of events that could be detected. The only other effect then is to reduce the possible duration of an event, therefore decreasing the total expected number. In Paper I, we showed that the naive point source optical depth is proportional to u_{thresh}^2 (the detectable impact parameter value) and thus replacing this with the projected star radius, changes the optical depth by a factor of U_*^2. Extending this naive calculation to limb-darkening, we can see that any effect on the projected star radius will directly impact the optical depth in quadrature. Therefore, limb-darkening, which effectively reduces the radius of the star, could drastically limit how far we can extend the current PBH mass range, since lower PBH masses would not be as detectable.

Here we explore this effect by repeating the above calculation for the expected number of PBH microlensing events, however now including the limb-darkening effect for each star. In order to do this, we used the linear limb-darkening model as described in Section 2.2.3, calculating the linear limb-darkening coefficients using the (Sing, 2010) model grid to find Kepler limb-darkening coefficients as a function of the effective temperature, surface gravity, and metallicity of each

of the 150,000 Kepler source stars. This enables us to calculate a new detectable magnification threshold A_{thresh} using the magnification formula in equation 2.13 for linear limb-darkening. The number of expected events including this linear limb-darkening effect is plotted in Figure 2.3 as the dashed line.

Surprisingly, Figure 2.3 does not show a significant effect of limb-darkening on the number of expected events. This can be understood as being due to the extreme precision of Kepler. Since Kepler light curves allow a magnification threshold of $A_{\text{thresh}} = 1.001$ or lower to be set, the median Kepler star (with a small stellar radius), will allow for a detection as soon as a PBH is within one Einstein radius of the projected star radius, where the limb-darkening does not play much of an effect yet on the light curve. On stars with bigger stellar radii, as well as models with smaller PBH masses, this limb-darkening will have some effect, since the magnification reaches A_{thresh} only when the PBH's impact parameter is inside the projected star radius, where the limb-darkening plays a role. However, even then, the duration is shortened by just a small amount. In Figure 2.4 we plot the percent change between the finite-source model with and without limb-darkening and we in fact see that there is a decrease of up to 17% for the lower lens masses. Moving towards higher PBH masses, almost all the Kepler stars which have radii on the order of a solar radius, will be able to have a detectable event within one Einstein radius of their projected radius, therefore, making the limb-darkening effects negligible. As a side-note, we found that if we did not discard 95% of the giant stars as variable, we would see an increase in the overall number of expected events due to limb-darkening at higher mass ranges. A_{max} is significantly lower for stars with large radii, and therefore the detectable value of x will be close to 0. We found that introducing limb-darkening in giant stars increases this A_{max}, increasing the possible detectable range of x, drastically increasing the number of detectable events. Also, the higher the mass of the PBH, the lower the projected star radius, and the more pronounced this effect will be, increasing the x ratio by a higher amount when introducing limb-darkening. Therefore the biggest effect of

limb-darkening on the number of events seems to be in these large-radii stars and on the lower lens masses. The effect of limb-darkening will also be crucial in the fitting of potential PBH events as well as in calculating the experimental detection efficiency.
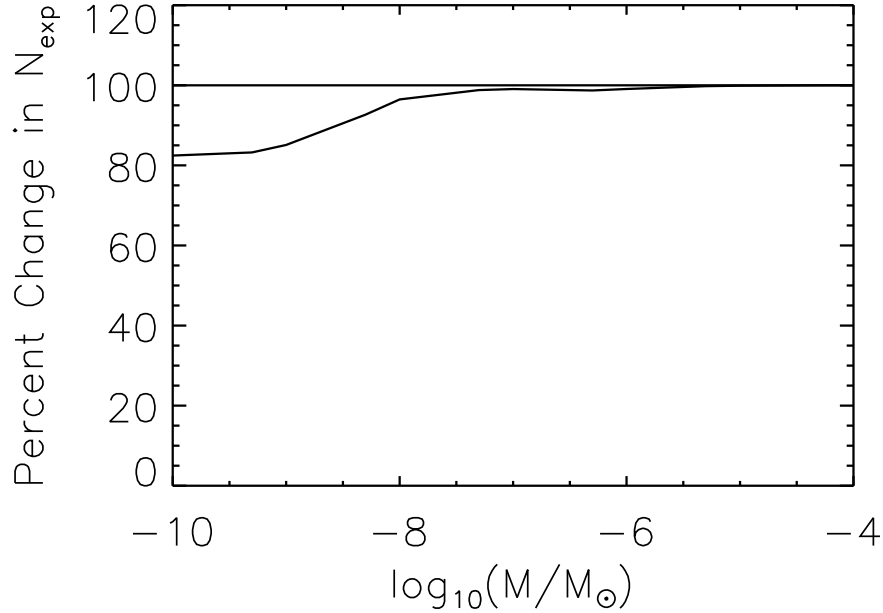
Figure 2.4 Percent change in the number of expected microlensing events due to limb-darkening for 780,000 star-years of Kepler observing time, defined as N_{exp} with limb darkening divided by N_{exp} without limb-darkening included. The horizontal line depicts 100%, representing no change, for comparison.

2.5   Detection Efficiency

In order to turn either detection or non-detection of microlensing into a statement about Galactic dark matter, one must calculate the efficiency at which the experiment finds PBH microlensing. This is done by performing a Monte Carlo simulation with randomly generated microlensing events and using the same selection criteria used to select microlensing light curves. One thus calculates the

detection efficiency ϵ, which is just the fraction of simulated events recovered. Using ϵ one can calculate the expected number of detectable events as

$$N_{\text{exp}} = \int_0^{x_{\text{max}}} \int_0^{u_{\text{thresh}}(x)} \int_0^\infty \epsilon(x, u_{\text{min}}, v_{\text{t}}) \frac{d\Gamma}{dx du_{\text{min}} dv_{\text{t}}} dv_{\text{t}} du_{\text{min}} dx, \qquad (2.18)$$

where

$$\frac{d\Gamma}{dx du_{\text{min}} dv_{\text{t}}} = 4 r_{\text{E}}(x) L \frac{\rho}{M} \frac{v_{\text{t}}^2}{v_{\text{c}}^2} e^{-v_{\text{t}}^2/v_{\text{c}}^2} \qquad (2.19)$$

as derived in Appendix A.2.

As before, we are making the approximation that the DM density is constant between the Earth and the source stars, valid for the relatively nearby Kepler stars, and using the fact that the Kepler field is nearly in the direction of the Sun's motion around the Galaxy. Previous microlensing experiments sampled the DM through long lines-of-sights through the halo requiring use of DM models that fall off as a function of galactic distance. Our distances of one or two kpc to the Kepler source stars (compared to 8 kpc to the Galactic Center) coupled with the fact that the Kepler stars are also at $\simeq 8$ kpc from the Center means that we need not use a halo model. Since the Milky Way DM distribution is quite uncertain this makes Kepler microlensing results more robust than results requiring the use of a halo model.

Without limb-darkening, ϵ is a function of only x and v_{t}, and the integral over u_{min} can be performed since that distribution is well-known due to a uniform stellar intensity across the projected star radius. This is not true when limb-darkening is included, since a lower u_{min} produces a higher amplitude in a limb-darkened light curve as well as decreases the duration of an event. The effect of limb-darkening on the efficiency is calculated by adding the parameter u_{min} to the Monte Carlo simulation. Thus the two competing effects can both influence this probability of detection.

2.6　Detectable Parameters

Also of interest is what we can say about a potential PBH if we do detect microlensing events. Assuming the measured light curve parameters are U_* and t_{event} found by fitting a limb-darkened finite-source microlensing light curve to any events of 2 hours or more, one can then calculate the mass probability and the distance probability of the lens in terms of these measured parameters. Uncertainty in the fit parameters, due for instance to having only 4 data points, will translate into uncertainties in the distributions, which could be characterized by Monte Carlo. Performing a change of variables in terms of the observable parameters, the mass and distance likelihood functions can be derived. We find the mass likelihood function by making the substitution $dx = R_*^2 c^2 U_*/(2GML)(R_*^2 c^2/4GML + U_*^2)^{-2} dU_*$ in Equation 2.17 to obtain the following expression independent of x:

$$\frac{d\Gamma}{dt_{\text{event}} dU_*} = \frac{\rho v_c^2 c^2}{2G} \frac{R_*^2 U_*}{M^2} \left(\frac{c^2 R_*^2}{4GML} + U_*^2 \right)^{-2} \beta^2 g(\beta), \qquad (2.20)$$

where

$$\beta = \frac{4 u_{\text{thresh}}(U_*, u_\lambda)^2 R_*^2 U_*^2}{t_{\text{event}}^2 v_c^2} \left(\frac{c^2 R_*^2}{4GML} + U_*^2 \right)^{-2} \qquad (2.21)$$

and

$$g(\beta) = \int_0^1 dy\, y^{3/2} (1-y)^{-1/2} e^{-\beta y}. \qquad (2.22)$$

In Figure 2.5 we plot this likelihood for $t_{\text{event}} = 2$ hours, $R_* = 1 R_\odot$, $L = 0.73$ kpc, $u_\lambda = 0.61$, and $A_{\text{thresh}} = A_{\text{limb}}(u_{\text{thresh}}, U_*) = 1.0007$, values typical of a median star in the Kepler field being monitored. The different curves represent the range of different values of U_* that could be measured for such a star undergoing a microlensing event. The distributions are normalized to have unit area under each curve so that each curve can be thought of as a probability density, that is for a measured duration of 2 hours and the given U_*, the curves give the relative likelihood of the event being caused by a PBH of mass shown on the abscissa. The rise of each curve at low mass is dominated by the β^2 term, which increases with

increasing U_*. The event duration is proportional to this projected star radius U_*, the PBH Einstein radius, r_E, and inversely proportional to the PBH transverse velocity, v_t. For a lower mass PBH only small transverse velocities will give rise to events longer than 2 hours. If U_* is decreased, then for the lower mass PBHs the transverse velocities have to be smaller, with the number of possible events for these mass ranges approaching zero. This is the reason that the distributions tend to zero for the smaller values of U_* for the smaller PBH masses in Figure 2.5. On the other hand, the decrease in each curve at larger PBH masses is caused by the lower number density of PBHs as their mass increases. The bigger the PBH lenses, the lower the number density needed to explain the local dark matter density. This in turn corresponds to less potential microlensing events. If microlensing events were to be observed in the Kepler data, we would then be able to, using distributions such as these, estimate the mass of the PBH making up the DM. The product of these likelihood functions would give us an estimate of the PBH DM mass range. We could also use these distributions to exclude some range of masses that the microlensing lenses could represent by measuring their t_{event} and U_* parameters.

In a similar way, we can calculate the lens distance likelihood function, with a change of variables where $M = c^2 R_*^2/(4GLU_*^2) \times x/(1-x)$ in Equations 2.20 - 2.22,

$$\frac{d\Gamma}{dt_{\text{event}}dU_*} = 8G\rho \frac{v_c^2}{c^2} \frac{L^2}{R_*^2} U_*(1-x)^2\beta^2 g(\beta), \tag{2.23}$$

where

$$\beta = 4\frac{R_*^2}{t_{\text{event}}^2 v_c^2}\frac{u_{\text{thresh}}(U_*, u_\lambda)^2}{U_*^2}x^2. \tag{2.24}$$

These distribution functions are plotted normalized to unit area under each curve in Figure 2.6. We see that the distance to the lens is not very dependent on the value of U_* measured. The distance probability distribution is dominated by the transverse velocities that are detectable at each distance to the lens (closer
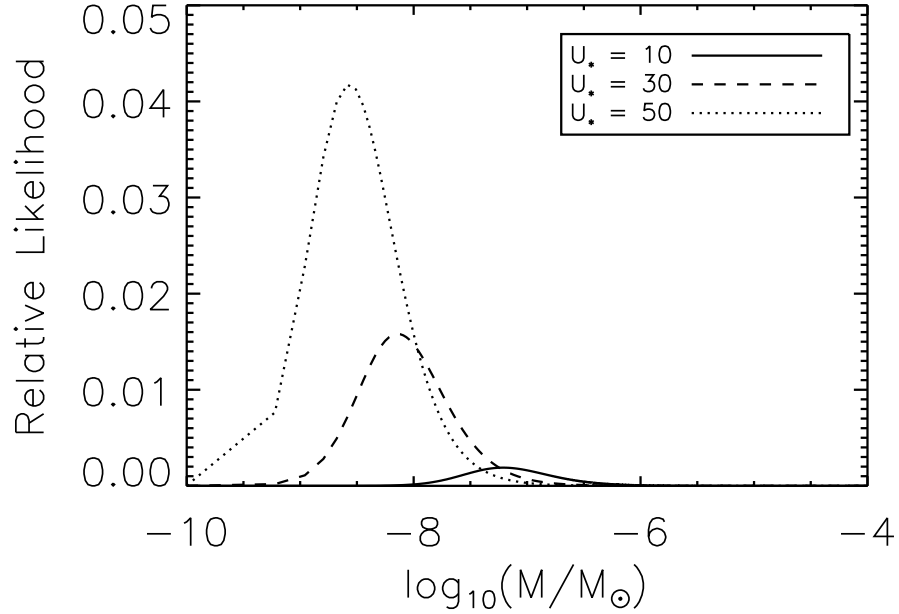
Figure 2.5 Lens mass relative likelihood for $t_{\text{event}} = 2$ hours, $R_* = 1R_\odot$, $L = 0.73$ kpc, $u_\lambda = 0.61$, and $A_{\text{limb}}(u_{\text{thresh}}, U_*) = 1.0007$ representing a median star in the Kepler field. The range of values for $U_* = 10, 30$, and 50 represents the range that could be measured in such a star. The curves here are normalized to have unit area under each curve, so that each curve represents the probability of each mass given the measured lightcurve parameters.

lenses have to be traveling slower in order to be detected for a given measured t_{event}). If a microlensing event was to be detected, then the probability distribution for the distance to the lens can be plotted for the particular stellar radius being monitored, just like in Figure 2.6. A bigger R_* will yield a distribution centered at lower x, while a smaller R_* will shift the distribution to higher x. We can then narrow down the most likely position of the lens based on the likelihood of detection at each distance for the particular star at which the event occurred. Overall, though, Figure 2.6 shows that it will not be easy to determine the distances to the lens.
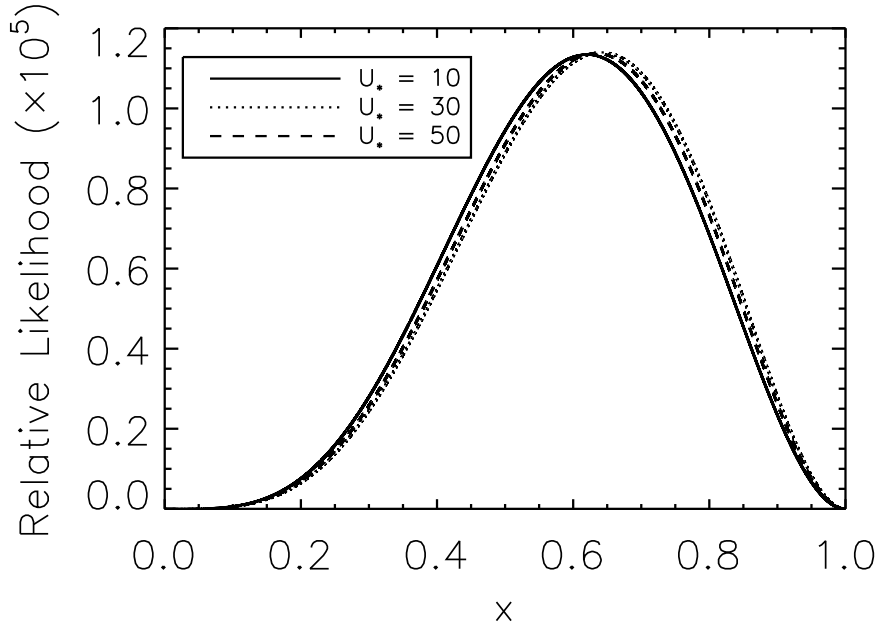
Figure 2.6 Lens distance relative likelihood for $t_{\mathrm{event}} = 2$ hours, $R_* = 1R_\odot$, $u_\lambda = 0.61$, and $A_{\mathrm{limb}}(u_{\mathrm{thresh}}, U_*) = 1.0007$ representing a median star in the Kepler field. The range of values for $U_* = 10, 30$, and 50 represents the range that could be measured in such a star. The curves here are normalized to have unit area under each curve.

2.7 Limitations

We turn now to considerations of what could be improved in upcoming missions, and what theoretical limitations the Kepler satellite has on detecting PBHs. As mentioned above, for the lower mass range of PBHs, the higher-velocity objects would not be detectable, because they result in magnifications that last too short a time. In Figure 2.7 we plot the maximum detectable velocity for a given PBH mass for a Kepler star with median parameter values of distance, radius, and A_{thresh}, calculated from the third quarter stars monitored. Throughout this section, by velocity we mean the velocity of the lens relative to the Earth-source line-of-sight in the direction perpendicular to the line-of-sight. As mentioned earlier, since

the Kepler stars are just out of the plane of the Milky Way disk, moving in the same direction as the Sun, we have assumed a negligible relative velocity between the Kepler satellite and the source stars. The Kepler satellite is therefore sensitive to PBH velocities which are radial in relation to center of the Galaxy. For a median type Kepler star, the v_c value of 220 km/s is on average detectable for masses above 2×10^{-7} solar masses. The lower-mass range events would be dominated by the projected radius of the star and therefore their maximum velocity curve approaches a constant value, but at the upper-mass range, the Einstein radii of the PBHs become important in detecting the event, and therefore more of the velocity distribution is detectable.
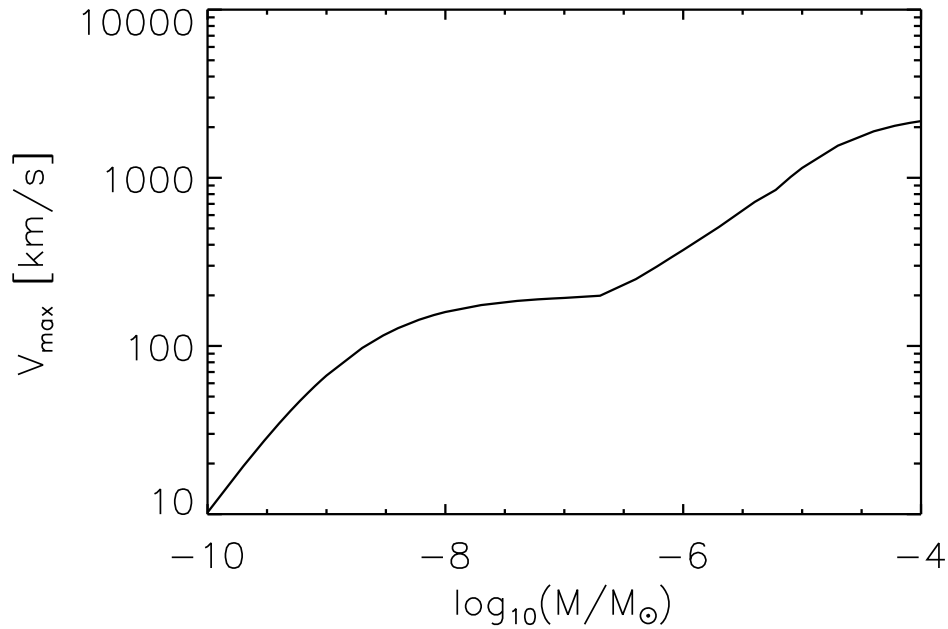
Figure 2.7 Maximum detectable transverse velocity, v_{max}, of PBHs, for a median type Kepler star with $R_* = 1R_\odot$, $L = 0.73$ kpc, $u_\lambda = 0.61$, and $A_{\mathrm{limb}}(u_{\mathrm{thresh}}, U_*) = 1.0007$, for a minimum $t_{\mathrm{event}} = 2$ hours.

In order to understand the limits on this detectable velocity, we calculated the optical depth, which determines how many measurements are needed

for any given PBH mass, and is defined as the number of PBHs inside a detectable microlensing tube (as defined in Griest 1991, with the addition of an x_{max} cutoff for the finite-source model). We therefore arrive at the equation $\tau = \pi(\rho/M)L \int_0^{x_{\text{max}}} u_{\text{thresh}}^2(x) r_{\text{E}}^2(x) dx$. A higher optical depth translates to a higher probability of detection. In Figure 2.8 we plot the optical depth, averaged over all the third quarter Kepler source stars. As can be seen, and as discussed in Paper I, the optical depth is now larger than the usual point-source one by a factor of u_{thresh}^2, which is dominated by the large U_*^2. The overall amplitude of the curve is also dominated by the average distance to the stars being monitored, whereas the shape of the curve at lower-mass PBHs is mostly governed by x_{max}, the detectable distance to the lens. This is set by the photometric accuracy of Kepler and cannot be changed.
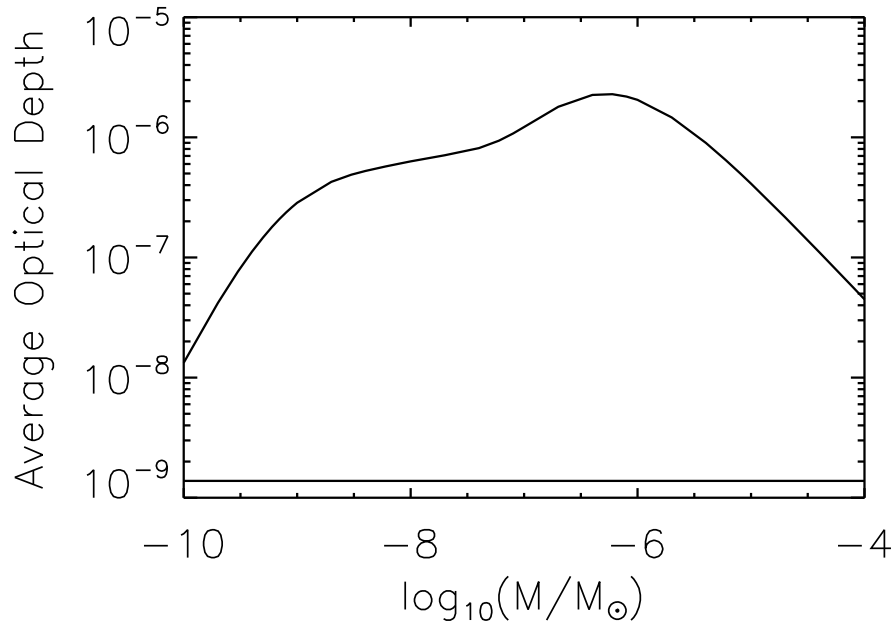
Figure 2.8 Average optical depth for the third quarter Kepler source stars being monitored. The horizontal line depicts the average optical depth if a point-source microlensing model is used for comparison.

Another limitation is related to our detection of events that last 2 hours or more, which is set by the Kepler satellite cadence. In Figure 2.9 we plot the average event duration, defined as $t_{\text{event}} = \tau/\Gamma$, averaged over all the third quarter Kepler stars being monitored. We can see that the average event duration is about 2 hours at around 10^{-8} solar masses. With the 2 hour selection criteria, we are therefore not able to detect most events for the smaller mass PBHs. Figure 2.9 shows that if events as short as 0.1 hours could be detected, one might be able to detect PBHs of masses down to $10^{-10} M_\odot$ or below. This could be improved upon by decreasing the Kepler satellite cadence when monitoring the stars.
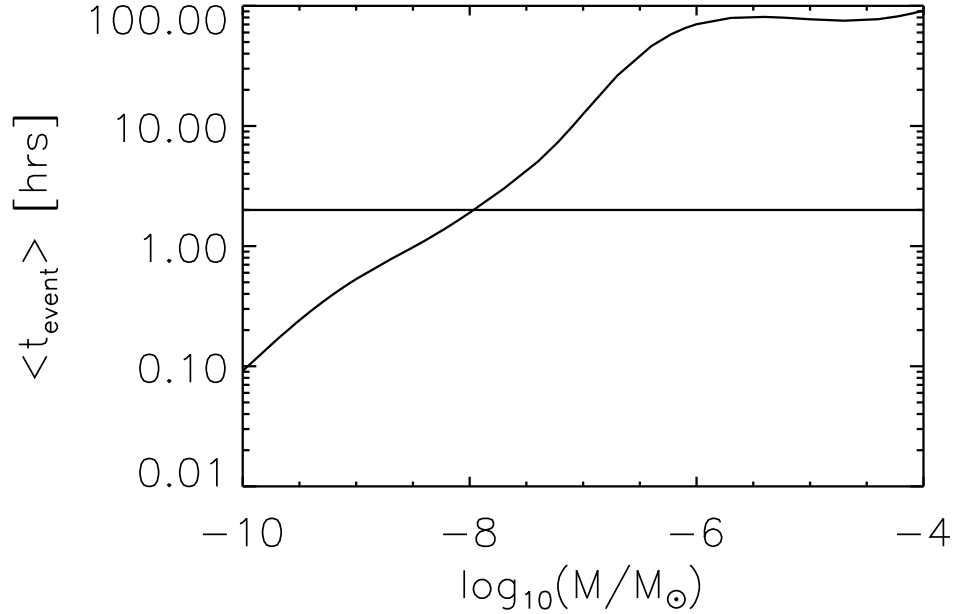
Figure 2.9 Average event duration, $< t_{\text{event}} >$, for the third quarter Kepler source stars being monitored. The horizontal line depicts $t_{\text{event}} = 2$ hours, which represents the minimum event duration required for a microlensing detection in the Kepler data.

Our theoretical detectable limits are due to both the threshold detection limit of Kepler and the cadence. The first cannot be changed, however we address

improvements to the second limitation in the next section.

2.8   Future Planned Missions

Kepler's extended mission of four additional years helps increase its sensitivity to lower-mass DM PBHs, as seen in Section 2.3. Here we address whether any possible additional measures could be undertaken during this extended mission to further increase this sensitivity. As seen in the previous section, in the analysis of the average microlensing event duration, cadence plays a huge role in these measurements. The Kepler camera actually takes one image every minute. Due to communication bandwidth, for most stars, the Kepler team adds up the one minute exposures into a 30 minute exposure before transmitting the data to Earth. These are called "long cadence" light curves and this is what is assumed in our calculations of the number of expected events and light curve characterization up to this point. However, for a selectable subset of stars, the entire one minute cadence ("short cadence") light curves are transmitted. Thus we wish to investigate the value for microlensing of the Kepler team returning short cadence data on a subset of stars. If we naively decrease the monitoring cadence to 1 min for all the Kepler source stars, for the full 780,000 star-years, the lower-mass DM PBH sensitivity increases by an order of magnitude, down to $2 \times 10^{-11} M_\odot$. Thus, while not possible due to bandwidth limitations, naively returning short cadence light curves for all the stars, would allow the exploration of one additional factor of 10 in the allowed PBH mass range. This could be an exciting possibility. However, when the cadence is decreased, the Poisson average error in each flux measurement increases. Thus with the set light gathering power of the Kepler telescope, a shorter cadence is offset by a larger A_{thresh}. In order to investigate this trade-off we redid our analysis assuming a 1 min cadence, but reducing the signal/noise for each flux measurement appropriately. Figure 2.10 shows the results of this analysis for 780,000 star-years with the same assumed stellar variability as in Section 2.3.

Although requiring short cadence for all the Kepler stars for the full mission is not achievable, this demonstrates that reducing the cadence time on the current source stars with the current light curve precision, would give only a modest increase in the sensitivity to lower-mass PBHs. However, if Kepler's aperture was large enough to maintain the current signal/noise at a one minute cadence, great improvement would be possible. In this we note that certain stars are far more valuable than others for detecting microlensing.
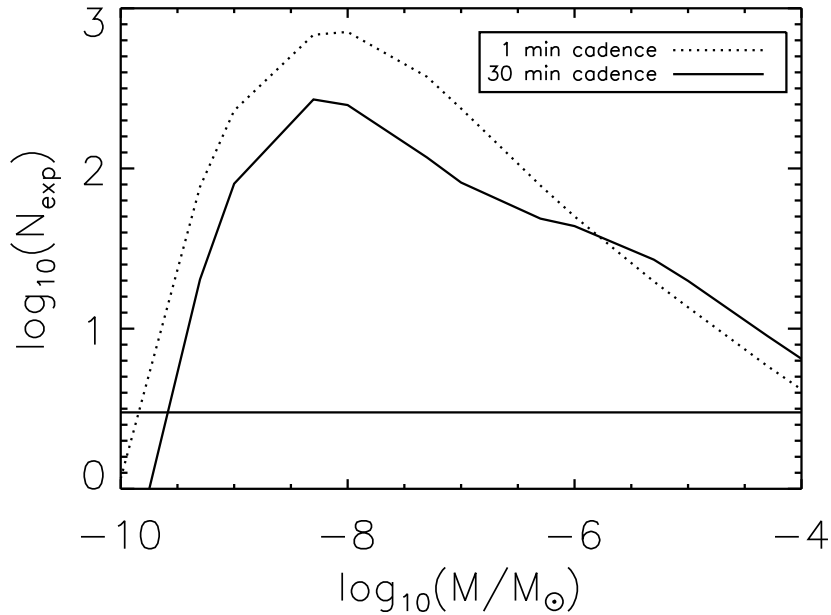
Figure 2.10 Total number of expected events for 780,000 star-years for 1 min and 30 min Kepler cadence monitoring times. The horizontal line shows the 95% confidence level limit if no events are detected.

We therefore address the characteristics of source stars and cadence times that would optimize this sensitivity in future missions similar to Kepler. Since 95% of the giant stars are seen to be variable, we focus on the dwarf stars, which would yield a higher number of less variable light curves for the same number of stars monitored. To investigate an optimal selection of stars for monitoring we

calculated the expected number of microlensing events for each non-variable dwarf star in the third quarter Kepler data. We plotted this per-star-N_{exp} versus other stellar parameters to see which correlated well with higher N_{exp}. In Figure 2.11, we show the best such correlation, N_{exp} vs. T_{eff}, where stars with higher T_{eff} are much more likely to return a detectable microlensing event. This figure shows that source stars with $T_{\mathrm{eff}} > 8000K$ are roughly 100,000 times more valuable for monitoring than stars with $T_{\mathrm{eff}} < 4000K$. There is some scatter in the points plotted, since we only apply a rough cut-off here to distinguish between the dwarf and giant stars based on the radius in the Kepler Input Catalog. We expect the giant stars to give a lower number for the expected number of events, for the same T_{eff} when compared to the dwarf stars, and these giant stars that have passed our rough cut-off may be what is contributing to this scatter. Overall, Figure 2.11 demonstrates that short cadence monitoring of a handful of carefully selected stars should be as valuable as large numbers of typical stars. The bandwidth problem, therefore, might be solved by long cadence monitoring of most stars but short cadence monitoring of a small sample.

Why does T_{eff} correlate so well with the expected number of lensing events? We see that for a point-source microlensing model detectability correlates well with luminosity; the more luminous stars give higher rates of predicted detections when the projected star radii and the lens Einstein radii are comparable. However, for these small PBH masses, the Einstein radii are much smaller than the projected star radii and the luminosity per unit area is more important, giving the upward trend with effective temperature.

In order to understand better the factors that influence the number of predicted events for a given star, we can make the following approximations. For light curves with 1% or better precision, as seen in Kepler, we can approximate $u_{\mathrm{thresh}} \approx U_*$. Also, for $R_*/R_\odot < 0.57\,(t_{\mathrm{event}}/1hr)\,(v_{\mathrm{c}}/220km/s)\,/x_{\mathrm{max}}$, we can approximate $\beta < 1$ and $\beta^2 g(\beta) \approx (3/8)\pi\beta^2$. Using these approximations in equation 1 of Paper I, with $x_{\mathrm{max}} < 1$ for $M = 10^{-10}M_\odot$, we arrive at the predicted rate of

Figure 2.11 Expected number of events per star-year for a PBH mass of $10^{-10} M_\odot$ with a 1 min cadence, for each non-variable dwarf star being monitored in the third quarter of the Kepler data, plotted with respect to T_{eff}.

detection for a given star (as derived in Appendix A.3)

$$\Gamma \approx 409.6\pi \frac{G^5 M^4 \rho}{c^{10} v_{\text{c}}^2} \frac{U_{*\text{max}}^{10}}{t_{\text{min}}^3} \frac{L^6}{R_*^6}, \tag{2.25}$$

where $U_{*\text{max}}$ corresponds to the maximum U_* detectable for a given A_{thresh} of a star. Calculating this for the appropriate ρ and v_{c}, we arrive at

$$\Gamma \approx 2.63 \times 10^{20} \left(\frac{L}{1\text{kpc}}\right)^6 \left(\frac{R_\odot}{R_*}\right)^6 \left(\frac{M}{M_\odot}\right)^4 \left(\frac{1\text{hr}}{t_{\text{min}}}\right)^3 \frac{1}{(A_{\text{thresh}}^2 - 1)^5} \frac{1}{\text{year}}. \tag{2.26}$$

Using the third quarter Kepler stars, we plot this approximation as a straight line in Figure 2.12 along with the actual rates calculated using our integral formulas. The approximation works very well for these low-mass PBHs and demonstrates how the stellar characteristics come into play in this calculation. As seen in Equation 2.26, a high stellar distance-to-radius ratio is important. The dependence of the rate on

the effective temperature is also readily explained by the fact that the distance is directly calculated from this value using $L = 1.19 \times 10^{-3} R_* (T_{\text{eff}}/T_\odot)^2 10^{0.2(V-A_{\text{V}}+B.C.)}$ where V is the apparent visual magnitude, A_{V} the extinction parameter, and B.C. the bolometric correction as in Paper I. We can see that the rate will be related to the effective temperature as $\Gamma \propto T_{\text{eff}}^{12}$. Also, decreasing the cadence will have a cubic effect on the rate expected, while maintaining a low A_{thresh} is also important, as expected. We can therefore predict, for example, that for a Kepler type mission, with 30 min cadence, in order to push the PBH mass limits down to $5 \times 10^{-11} M_\odot$, one would have to observe 160,000 dwarf stars with a $(L/1\text{kpc})(R_\odot/R_*)$ fraction of 3.15 or higher, while maintaining the 0.1% lightcurve precision. It seems therefore that pushing to smaller PBH masses in order to close the remaining PBH DM mass window will be difficult. However, if events were detected, a survey pointing towards or away from the Galactic center would provide us with more information about the DM distribution. We therefore address the WFIRST mission next.

2.8.1 WFIRST

NASA's Wide-Field Infrared Survey Telescope (WFIRST), is a proposed next-generation space observatory being designed to search for Dark Energy and extrasolar planets (Green et al., 2011). As the highest ranked large space mission recommendation in the Astronomy and Astrophysics 2010 Decadal Survey, it is being designed to perform Dark Energy measurements using Baryon Acoustic Oscillations, Type Ia Supernovae, and Weak Lensing. In addition, it will complement the Kepler mission with its microlensing search for extrasolar planets, targeting stars towards the galactic bulge. Here we address its value for PBH DM limits or characterization. The preliminary specifications are to monitor 2×10^8 stars with a cadence of 15 min and a 1% photometry precision (Bennett et al., 2010). It is especially exciting, as it will monitor the center of the Galaxy, and therefore could potentially provide insights into the DM distribution of the Milky Way. It will add
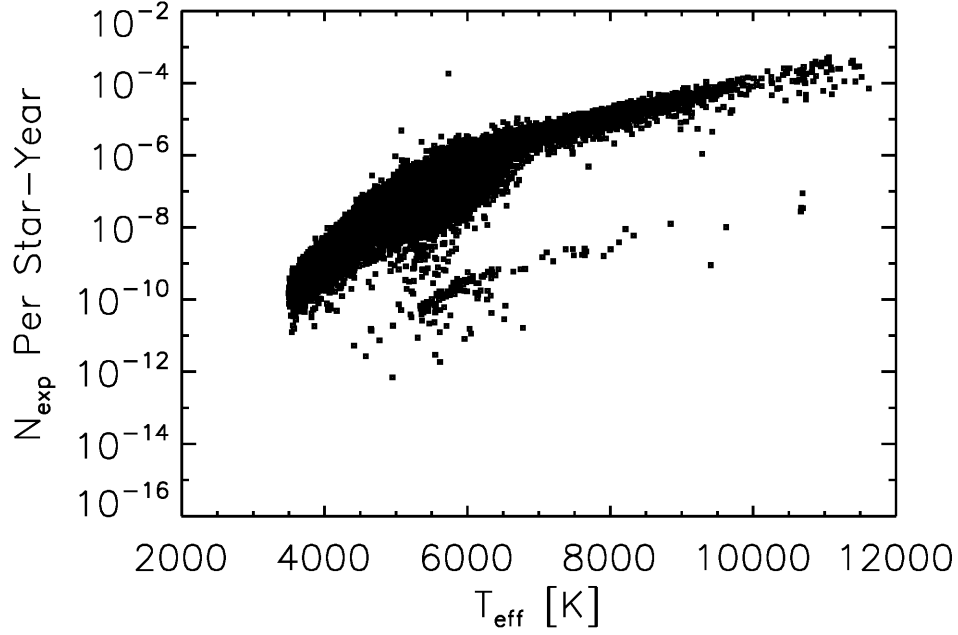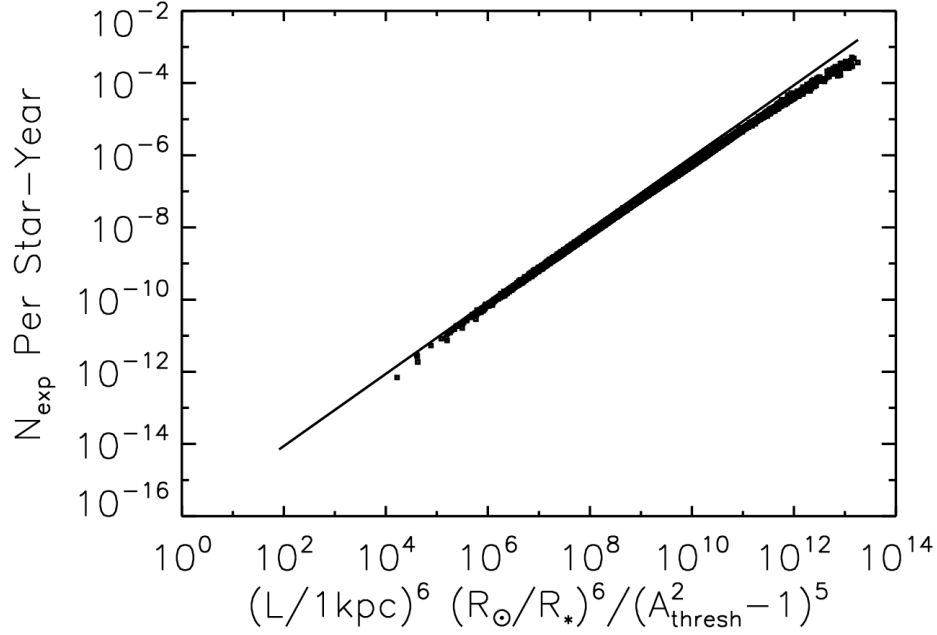
Figure 2.12 Expected number of events per star-year for a PBH mass of $10^{-10} M_\odot$ with a 1 min cadence, for each non-variable dwarf star being monitored in the third quarter of the Kepler data, plotted with respect to the stellar variables governing this number. The straight line represents the approximation in Equation 26.

to the existing DM dynamical constraints due to microlensing (Iocco et al., 2011). Here we provide a preliminary calculation for the number of expected events, if the stars being monitored are similar to those of Kepler, as well as assuming a simple DM distribution of the form

$$\rho(x) = \rho_0 \frac{a^2 + r_0^2}{a^2 + L^2(1-x)^2},\tag{2.27}$$

with $a = 5$ kpc. Following our analysis for the Kepler mission, we find the rate of detection,

$$\frac{d\Gamma}{dt_{\text{event}}} = \rho_0 \frac{a^2 + r_0^2}{M} L v_c^2 \int_0^{x_{\max}} dx \frac{1}{a^2 + L^2(1-x)^2} \beta^2 g(\beta).\tag{2.28}$$

In Figure 2.13 we plot the number of expected events for one year of monitoring

of Kepler-type stars (with $R_* \approx 1 R_\odot$) toward the galactic bulge ($L = 8$ kpc), with 25% of stars assumed to be variable, and ignoring transverse velocity. Alongside, we plot the approximation given in Equation 2.26 as a dashed line, demonstrating its usefulness for predicting microlensing rates for PBH lenses with masses less than $10^{-10} M_\odot$, as stated in the previous section.
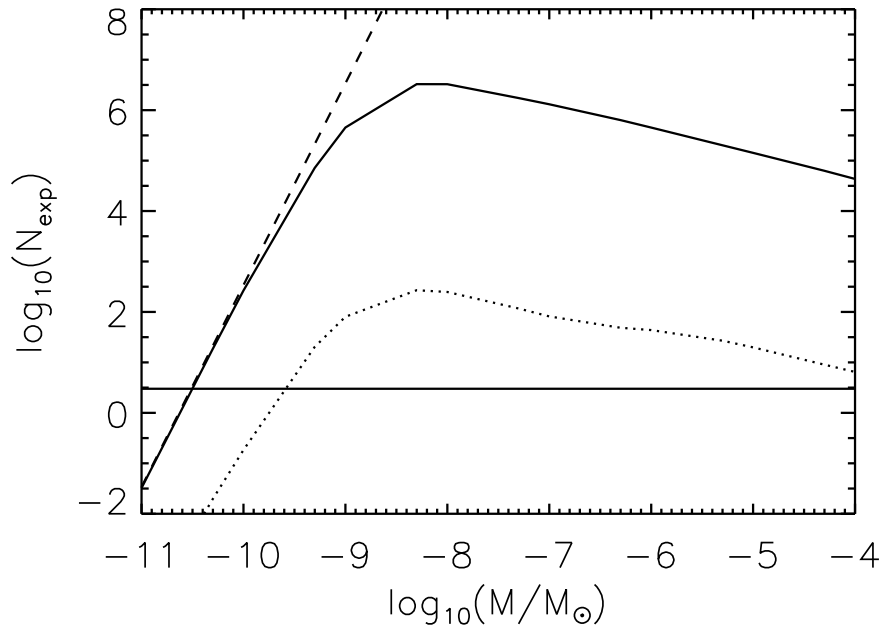
Figure 2.13 Total number of expected events towards the galactic bulge for a mission such as WFIRST. The dashed line represents the approximation of Equation 26, appropriate for PBH lens masses below $10^{-10} M_\odot$. The horizontal line shows the 95% confidence level limit if no events are detected. The dotted line represents the predicted Kepler microlensing limits as shown in Figure 3, for comparison.

This is a preliminary analysis, however, it demonstrates that WFIRST will complement Kepler in the same PBH mass range, providing a greater number of events, and exploring an additional order of magnitude of the PBH DM window. If the stars being monitored are larger than the Kepler type stars, the number of expected events will decrease, as predicted by Equation 2.26. Also, the transverse velocity of the source stars will have a sizable effect, as well as lensing due to other

stars. If PBHs are detected by Kepler, WFIRST will be able to study the DM characteristics, such as velocity and spatial distributions.

2.9 Conclusions

In this theoretical paper, we addressed the possibility of detecting or ruling out PBH DM using the microlensing of Kepler source stars in the largely unconstrained window between $5 \times 10^{-14} M_\odot$ and $2 \times 10^{-8} M_\odot$. Building upon Paper I, we introduced a more proper treatment of the population of source stars and their variability, including a finite-source microlensing framework which includes limb-darkening. Using this analysis, we found that the PBH DM mass constraints could be extended down to $2 \times 10^{-10} M_\odot$, two orders of magnitude below current limits and a third of a magnitude lower than our previous work. As mentioned, a proper Monte Carlo simulation will be needed to fully understand the experimental detection efficiency. We provide a limb-darkened microlensing framework which will be used to fit potential Kepler light curves, and which will help to distinguish between PBH's and stellar flares, the main source of experimental systematic error. Our analysis leaves us optimistic in being able to provide a probability for the masses of the lenses if any microlensing events are found, and therefore characterizing the DM and its epoch of formation. We found a very strong correlation between the rate of PBH detection for a given star and its effective temperature, providing an approximate expression for this rate for these low-mass PBHs. This should help in selecting stars to be monitored in future microlensing experiments. Using this approximation, it can be seen that fully closing the remaining PBH DM window using a microlensing method will be difficult, however sensitivity could potentially be improved by another order of magnitude using future planned missions, such as the WFIRST survey towards the galactic bulge. More analysis for this case is needed.

2.10   Acknowledgements

References

Agol, E. 2002, The Astrophysical Journal, 579, 430

Alcock, C., Allsman, R. A., Alves, D., Ansari, R., Aubourg, É., Axelrod, T. S., Bareyre, P., Beaulieu, J.-P., Becker, A. C., Bennett, D. P., Brehin, S., Cavalier, F., Char, S., Cook, K. H., Ferlet, R., Fernandez, J., Freeman, K. C., Griest, K., Grison, P., Gros, M., Gry, C., Guibert, J., Lachièze-Rey, M., Laurent, B., Lehner, M. J., Lesquoy, É., Magneville, C., Marshall, S. L., Maurice, É., Milsztajn, A., Minniti, D., Moniez, M., Moreau, O., Moscoso, L., Palanque-Delabrouille, N., Peterson, B. A., Pratt, M. R., Prévôt, L., Queinnec, F., Quinn, P. J., Renault, C., Rich, J., Spiro, M., Stubbs, C. W., Sutherland, W., Tomaney, A., Vandehei, T., Vidal-Madjar, A., Vigroux, L., & Zylberajch, S. 1998, The Astrophysical Journal Letters, 499, L9

Barnacka, A., Glicenstein, J.-F., & Moderski, R. 2012, Physical Review D, 86, 043001

Bennett, D. P., Anderson, J., Beaulieu, J. ., Bond, I., Cheng, E., Cook, K., Friedman, S., Gaudi, B. S., Gould, A., Jenkins, J., Kimble, R., Lin, D., Mather, J., Rich, M., Sahu, K., Shao, M., Sumi, T., Tenerelli, D., Udalski, A., & Yock, P. 2010, arXiv:1012.4486B

Borucki, W. J., Koch, D., Basri, G., Batalha, N., Brown, T., Caldwell, D., Caldwell, J., Christensen-Dalsgaard, J., Cochran, W. D., DeVore, E., Dunham, E. W., Dupree, A. K., Gautier, T. N., Geary, J. C., Gilliland, R., Gould, A., Howell, S. B., Jenkins, J. M., Kondo, Y., Latham, D. W., Marcy, G. W., Meibom, S., Kjeldsen, H., Lissauer, J. J., Monet, D. G., Morrison, D., Sasselov, D., Tarter, J., Boss, A., Brownlee, D., Owen, T., Buzasi, D., Charbonneau, D., Doyle, L., Fortney, J., Ford, E. B., Holman, M. J., Seager, S., Steffen, J. H., Welsh, W. F., Rowe, J., Anderson, H., Buchhave, L., Ciardi, D., Walkowicz, L., Sherry, W., Horch, E., Isaacson, H., Everett, M. E., Fischer, D., Torres, G., Johnson, J. A., Endl, M., MacQueen, P., Bryson, S. T., Dotson, J., Haas, M., Kolodziejczak, J., Van Cleve, J., Chandrasekaran, H., Twicken, J. D., Quintana, E. V., Clarke, B. D., Allen, C., Li, J., Wu, H., Tenenbaum, P., Verner, E., Bruhweiler, F., Barnes, J., & Prsa, A. 2010, Science, 327, 977

Carr, B. J., Kohri, K., Sendouda, Y., & Yokoyama, J. 2010, Physical Review D, 81, 104019

Ciardi, D., von Braun, K., Bryden, G., van Eyken, J., Howell, S. B., Kane, S. R., Plavchan, P., Ramírez, S. V., & Stauffer, J. R. 2011, The Astronomical Journal, 141, 108

Feng, J. L. 2010, Annual Review of Astronomy and Astrophysics, 48, 495

Frampton, P. H., Kawasaki, M., Takahashi, F., & Yanagida, T. T. 2010, Journal of Cosmology and Astroparticle Physics, 04, 023

Green, J., Schechter, P., Baltay, C., Bean, R., Bennett, D., Brown, R., Conselice, C., Donahue, M., Gaudi, S., Lauer, T., Perlmutter, S., Rauscher, B., Rhodes, J., Roellig, T., Stern, D., Sumi, T., Tanner, A., Wang, Y., Wright, E., Gehrels, N., Sambruna, R., & Traub, W. 2011, arXiv:1108.1374G

Griest, K. 1991, The Astrophysical Journal, 366, 412

Griest, K., Lehner, M. J., Cieplak, A. M., & Jain, B. 2011, Physical Review Letters, 107, 231101 (Paper I)

Hawking, S. 1971, Monthly Notices of the Royal Astronomical Society, 152, 75

Hawking, S. W. 1974, Nature, 248, 30

—. 1975, Communications in Mathematical Physics, 43, 199

Iocco, F., Pato, M., Bertone, G., & Jetzer, P. 2011, Journal of Cosmology and Astroparticle Physics, 11, 29

Kesden, M. & Hanasoge, S. 2011, Physical Review Letters, 107, 111101

Khlopov, M. Y. 2010, Research in Astronomy and Astrophysics, 10, 495

Koch, D. G., Borucki, W. J., Basri, G., Batalha, N. M., Brown, T. M., Caldwell, D., Christensen-Dalsgaard, J., Cochran, W. D., DeVore, E., Dunham, E. W., III, T. N. G., Geary, J. C., Gilliland, R. L., Gould, A., Jenkins, J., Kondo, Y., Latham, D. W., Lissauer, J. J., Marcy, G., Monet, D., Sasselov, D., Boss, A., Brownlee, D., Caldwell, J., Dupree, A. K., Howell, S. B., Kjeldsen, H., Meibom, S., Morrison, D., Owen, T., Reitsema, H., Tarter, J., Bryson, S. T., Dotson, J. L., Gazis, P., Haas, M. R., Kolodziejczak, J., Rowe, J. F., Cleve, J. E. V., Allen, C., Chandrasekaran, H., Clarke, B. D., Li, J., Quintana, E. V., Tenenbaum, P., Twicken, J. D., & Wu, H. 2010, The Astrophysical Journal Letters, 713, L79

Luo, Y., Hanasoge, S., Tromp, J., & Pretorius, F. 2012, The Astrophysical Journal, 751, 16

Paczynski, B. 1986, The Astrophysical Journal, 304, 1

Sing, D. K. 2010, Astronomy and Astrophysics, 510, A21

Witt, H. J. & Mao, S. 1994, The Astrophysical Journal, 430, 505

Zel'dovich, Y. B. & Novikov, I. D. 1966, Astronomicheskii Zhurnal, 43, 758

Chapter 3

Preliminary Constraints for Primordial Black Hole Dark Matter

3.1 Introduction

Following our theoretical predictions for the potential of the Kepler satellite to constrain or detect primordial black hole dark matter (PBH DM) in Chapter 2, we conduct a preliminary analysis of the first two years of publicly available data. As mentioned above, the Kepler satellite, which monitors ∼160,000 stars at a distance of 1 kpc for a total mission duration of 7.5 years, is surprisingly sensitive to lower mass PBH microlensing events. This is due to Kepler's photometric sensitivity of one part in 10,000 or better, allowing for magnification threshold detections of 0.1% or less, as well as the finite-source effects, due to the stars being relatively close by. As calculated in Cieplak & Griest (2013), this allows for a PBH sensitivity in the mass range of $2 \times 10^{-10} M_\odot$ to $2 \times 10^{-6} M_\odot$, a mass range that includes two orders of magnitude of an unexplored region (see (Carr et al., 2010) for a review). While the above sensitivity was a theoretical prediction, in

this analysis we look at the actual, experimental detection range of the first two years of publicly available light curves.

3.2 Data Description

The data which we are analyzing includes ∼160,000 light curves from Quarters 2-9, each containing 4,400 flux measurements taken over 90 days. Each flux measurement is a sum of 1 minute exposures that is transmitted every 30 minutes, to give a 30 minute cadence. We use the Kepler pipeline flux data. Since the Kepler team is searching for flux decrements which are the exact opposite of PBH signatures, we trust that their pipeline effectively optimizes the search for any flux decrements or magnifications. We therefore have the photometric flux measurements (pdcflux), the flux error (pdcfluxerror), and the quality flag (sap quality) for each point. The quality flag is set to a nonzero value if the data is suspect, such as during a detection of a cosmic ray.

3.3 Selection Criteria

We employ several selection criteria, which all have to be met for a PBH microlensing candidate lightcurve to qualify as a candidate. We define the magnification A to be the ratio of the flux at a given point, to the mean flux calculated from 300 points towards the middle of the lightcurve. Our first scan of the data requires 4 sequential points which lie 3σ above the mean flux. As mentioned in the previous analysis, we expect about 25% of the dwarf stars, and 95% of the giant stars to be variable (Ciardi et al., 2011). In order to avoid false positives due to stellar variability, we calculate the autocorrelation function, requiring the value at a 30 minute lag to be lower than 0.7, and we discard any stars which have more than 2 bumps detected. This effectively removes 34% of the dwarf stars and 91% of the giant stars, which is close to our expectations of the previous analysis.

Our assumption of Gaussian errors assumed in the previous analysis in Chapter 2 however is not quite accurate. After eliminating the variable stars as stated above, our selection criteria identifies 10,000 candidates, which is far too many, based on the expected number of events. Therefore, to avoid detecting bumps which arise out of the amount of overall variability in the lightcurve, which is not included in the measurement of photometric error, we ensure that the ratio $|A - 1|/\sigma$ during the bump is more than 5.5 times more significant than the same ratio before and after the bump. After investigating the variability in the data, we found that this requirement effectively measures whether the bump arises from the stars' noise levels which are not included in the Gaussian error assumption. After applying the above criteria, we find many stars which have bump detections, all at the same time across different light curves. We in effect get rid of these, since we suspect this arises due to instrumental effects during this time or due to the detrending software. We block this entire time from the remainder of the analysis as suspect.

After applying the main criteria cuts as above, we find a large number of bumps (on the order of 100) arising from one of our main sources of experimental systematic error which was unaccounted for in our previous theoretical calculations. These are stellar flares, which arise due to magnetic activity in stellar atmospheres. Walkowicz et al. (2011) analyzed stellar flares on M and K dwarf stars in the Kepler light curves, while Maehara et al. (2012) performed an analysis of flares on solar type stars, finding that they can release large amounts of magnetic energy on the order of hours. An example of such a stellar flare is pictured in Figure 3.1. As seen in this example, we expect these stellar flares to be asymmetric, rising fast, and declining in an exponential fashion. We are therefore able to fit these light curves to two fits, one being the stellar flare model with three parameters (t_0, the peak time, $A_{\max}$, the maximum amplitude of the flare, and λ, the exponential decay constant), the other being the microlensing fit model with four parameters (t_0, the time of closest approach, $\hat{t}$, the time it takes for the lens to cross the projected star radius,

$A_{\max}$, the maximum magnification, and $\epsilon_{\min}$, the minimum impact parameter in terms of the stellar radius). For the flare fit, we allow a quick rise consisting of one or two points to reach the the maximum amplitude. After such a fit, we eliminate any flares by requiring the chi-squared per degree of freedom for the microlensing fit to be lower than 75% of that for the flare star fit, where the requirement arises by inspection of each of the fits. This successfully removes longer duration flare events, however, there are still some bumps which pass these cuts but are suspected to be flares with a 2 hour duration. This might be due to the fact that since the 30 minute flux cadence is an integrated measurement, the maximum peak of the flare could be distributed between the two bins, giving rise to two points close to the maximum, and thereby mimicking a symmetric microlensing event. If this is taken into account, we in effect only have three points to which we can successfully fit a model. Due to the small number of points for fitting purposes, we change the minimum requirement of 4 sequential flux measurements 3σ above average to 5 sequential measurements. Also, to address the similar issue, where there might be a tail in the flare event in the points after the bump, we add an asymmetry statistic, where the absolute difference between the flux measured before the peak and after the peak, divided by the total flux above the median under the peak, has to be smaller than 17%. This makes sure we get rid of any asymmetric events, where the asymmetry might arise in the tails of the events and would not be seen in the bump.

Finally, if a stellar flare fit is not a best fit, we still require the lensing model to be a good fit in general. We therefore impose the criterion that the chi-squared per degree of freedom for the microlensing fit be less than 3.5, as well as for the chi-squared per degree of freedom under the peak to be less than 4 times that outside of the peak, so that the fit under the peak is only allowed to be slightly worse than the fit outside.

These criteria effectively remove the irreducible background of the stellar flares and any variability in the stars, as well as any instrumental effects. The
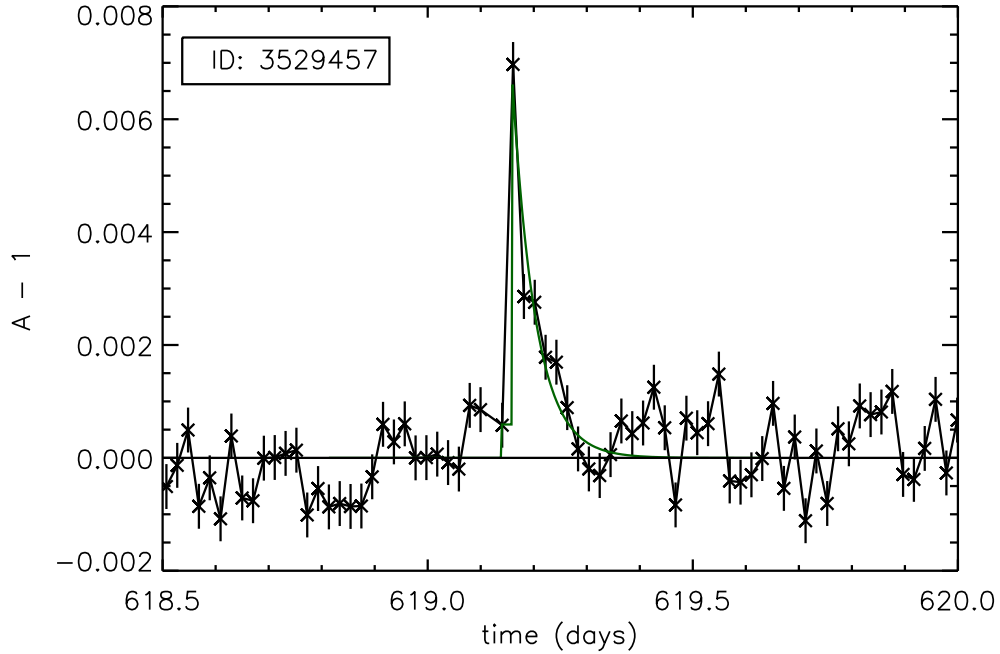
Figure 3.1 Example of a stellar flare seen in the Kepler light curves. The flare fit is show in green, while the ID of the star is shown in the upper left corner.

tightening of these constraints translates directly into the lowering of any potential limits on primordial black hole dark matter as discussed below. The requirements for the cuts therefore result from a balance between tightening the constraints enough to get rid of all possible background, while at the same time keeping the number of expected events high enough for potential primordial black hole dark matter limits. A summary of all the cuts is pictured in Table 3.1.

3.4 Comets

Applying these cuts to all the first two years of Kepler data, we obtain 17 candidate PBH events, all with symmetry requirements and fits consistent with a microlensing shape, as pictured in an example in Figure 3.2. However, when we plot the positions of these events in Figure 3.3, we can see that they lie along arcs

Table 3.1. Definitions of Statistics and Selection Criteria

Statistic	Definition
A_i	$\text{flux}_i / \langle \text{flux} \rangle$
σ_i	reported error of flux normalized by average flux
bump	sequence of 4 or more contiguous fluxes with $A_i - 1 \geq 3\sigma_i$
nbump	number of bumps in lightcurve
bumplen	number of contiguous fluxes with $A_i - 1 \geq 3\sigma_i$
lag1autocorr	$\frac{1}{N} \sum_{i=1}^{i=N} ((A_i - 1)(A_{i+1} - 1))$
bumpvar	$\sum |A_i - 1|/\sigma_i$ over points under bump
leftedgevar	$\sum |A_i - 1|/\sigma_i$ over 2 bumplen points
	starting 6 bumplen before bump
rightedgevar	$\sum |A_i - 1|/\sigma_i$ over 2 bumplen points
	starting 4 bumplen after bump
dof	number of data points within 5 bumplen of peak
	minus number of fit parameters
mlchi2dof	χ^2 of fit to microlensing shape divided by dof
fchi2dof	χ^2 of fit to exponential flare shape divided by dof
chi2in	χ^2 of microlensing fit for points with time, t_i,
	such that $t_0 - 1.5\hat{t} < t_i < t_0 + 1.5\hat{t}$
chi2out	χ^2 of microlensing fit for points with time,
	$t_0 - 6\hat{t} < t_i < t_0 + 6\hat{t}$, but not in chi2in
Nasy	number of points near peak time, t_0, for asymmetry;
	larger of 1.5λ and $2\hat{t}$
asymmetry	$\sum_{\text{Nasy points}} |A(t_0 - t_i) - A(t_0 + t_i)|/(\sum A(t_i) - \text{Nasy} A_{min})$

Selection Criterion	Purpose
$0 < \text{nbump} < 3$	remove variable stars and stars with no transient
$\text{bumplen} \geq 4$	level 1 trigger (significant bump)
$\text{bumplen} \geq 5$	remove short duration flare events
$\text{lag1autocorr} > 0.7$	remove obvious variable stars
$\text{bumpvar} > \frac{1}{2}5.5(\text{ leftedgevar} + \text{rightedgevar})$	signal to noise cut when reported errors are non-Gaussian
$\text{edgecriterion} > 0$	remove bumps that start or end in bad data
$\text{mlchi2dof} < 0.75 \text{ fchi2dof}$	microlensing fit significantly better than flare fit
$\text{mlchi2dof} < 3.5$	microlensing fit is not too bad
$\text{asymmetry} < 0.17$	remove short duration flare events
$\text{chi2in/chi2out} < 4$	remove events where χ^2_{dof} under peak is much worse than
	χ^2_{dof} outside peak area
$\text{asymmetry} < 0.17$	remove short duration flare events

or lines in the Kepler field. All of these objects are also detected only in Quarters 5 and 9, at the same time of year. Therefore, the Quarter 5 events suggest an object moving through the Kepler field at a constant speed of 16 arcseconds/hour, while the Quarter 9 distribution suggests two objects, moving along two lines.
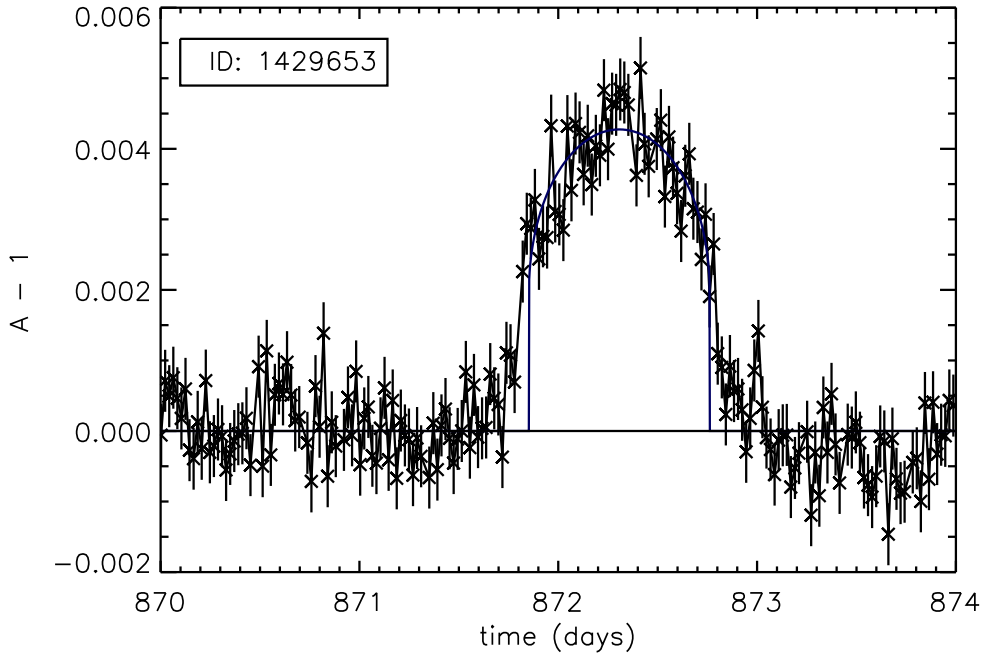
Figure 3.2 Example of a comet seen in the Kepler light curves. The microlensing fit is show in blue, while the ID of the star is shown in the upper left corner.

The Quarter 5 object's distance can be estimated, by approximating its movement on the sky as solely due to Kepler's motion around the Sun at 30 km/s. The distance can then be estimated to be about 10 AU. Using the amount of flux added to the lightcurve and the g magnitude of the source star, we calculate the g magnitude of the object as between 20 and 21.5. We then use the right ascension (RA) and declination (dec) of the background Kepler stars against which the object is visible to look up the possible object in the Minor Planet Center MPChecker (IAU, 2013). We performed a 300 arcmin radius search, since Kepler is in an Earth-trailing orbit, and the position seen by the telescope will be slightly offset from the
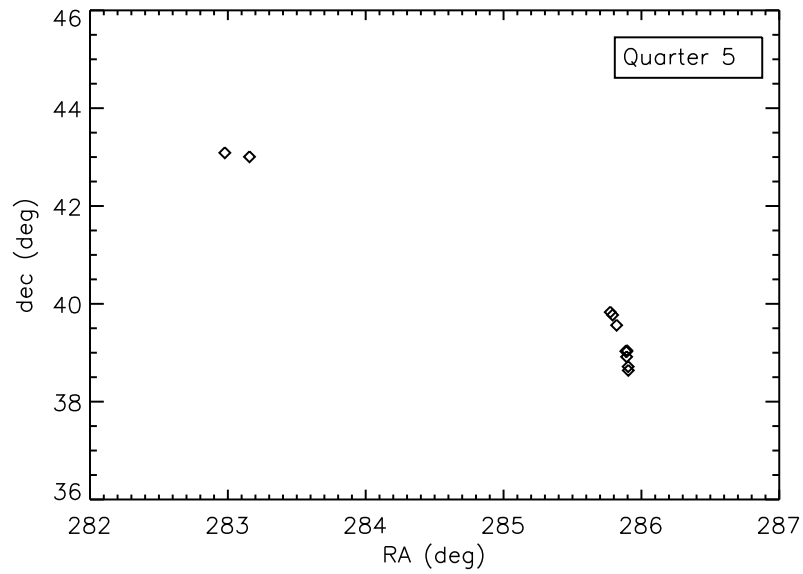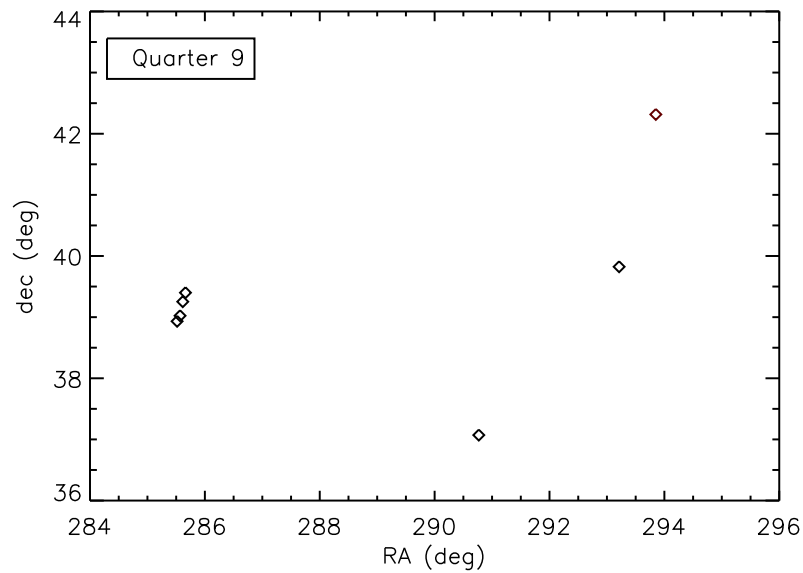
Figure 3.3 Position of the comets found in Quarter 5 (a) and Quarter 9 (b). The red diamond represents an event that did not pass all the cuts, however is pictured since it confirms the existence of a third comet.

RA and dec defined on Earth for the background stars. We find that in fact, this is a well-studied comet, which passes through the locations of our events, called comet C/2006 Q1 (McNaught) with offsets of up to 212 arcmin with respect to the stars' locations as seen by Earth. At the time it was passing through the Kepler field in Quarter 5, it was also in fact 10 AU away, confirming our predictions. All of our Quarter 5 events are therefore well explained by tracing this comet's path.

Similarly, Quarter 9 pictures two objects moving at constant angular speed. One of the events pictured did not pass all the cuts, however is pictured as a confirmation that there is in fact an object moving in a line across the field. We again looked these up in the Minor Planet Center MPChecker (IAU, 2013), and found that the slower moving comet does in fact correspond to C/2007 Q3 (Siding Spring), however we did not find any known comets which agreed with the position of the faster moving object. By obtaining the distance to the known comet, we can then do a conversion from the RA and dec measured from Earth to that which would be seen by Kepler, and we find that the known comet agrees in location with the slower moving object to within 100 arc seconds. We therefore are able to confirm this object's identity. Applying the same technique as above, we also found a g magnitude of 21.9 for the slower moving object, and a g magnitude of 21.9 for the faster moving object. Since the unknown comet is moving faster along the Kepler field, we cannot make the distant object approximation as with the previous comet. It is therefore probably a lot closer than the other two comets. Since we cannot identify it in any known comet database, we conclude that this could be a comet that has been previously undetected. Although not very efficient, we found that monitoring stellar light curves also produces potential comet discoveries. Table 4.1 lists the time, location, and magnitudes of the comets found.

After removing these events as comets, there are no PBH microlensing candidates that remain in the first two years of the analyzed Kepler data.

Table 3.2.   Comets in Kepler data

quarter	Kepler ID	time[a]	RA	dec	gmag[b]	comet
5	3527753	482.949	285.905	38.6395	21.3	C/2006 Q1
5	3628766	483.582	285.904	38.7161	21.4	C/2006 Q1
5	3833908	485.217	285.893	38.9171	20.8	C/2006 Q1
5	3937408	486.116	285.887	39.029	21.5	C/2006 Q1
5	3937430	486.106	285.894	39.0263	21.2	C/2006 Q1
5	3937432	486.259	285.894	39.0463	21.4	C/2006 Q1
5	4447346	490.591	285.82	39.5627	21.7	C/2006 Q1
5	4637389	492.379	285.791	39.7713	22.1	C/2006 Q1
5	4729654	492.880	285.774	39.8299	21.9	C/2006 Q1
5	7421340	530.305	282.978	43.0877	20.8	C/2006 Q1
5	7421791	528.762	283.157	43.0068	20.6	C/2006 Q1
9	1429653	872.332	290.769	37.0712	21.3	new
9	3833007	837.604	285.517	38.9324	21.9	C/2007 Q3
9	3936698	838.523	285.568	39.023	21.5	C/2007 Q3
9	4138614	840.608	285.615	39.2529	21.5	C/2007 Q3
9	4347043	842.049	285.662	39.4001	22.6	C/2007 Q3
9	4751561	879.688	293.212	39.8243	21.2	new
9	6870049*	886.968	293.851	42.3156	21.9	new

[a]Kepler days; convert to Julian date by adding 2454833

[b]Found by adding the bump peak flux to the source star magnitude. See text.

*Did not pass all cuts.

3.5 Limits on Primordial Black Hole Dark Matter

Since we do not detect any PBH microlensing candidates, we can put a limit on PBH DM in some mass range. To do this we utilize Equation 2.18 derived in the previous chapter. Since in the theoretical approach, we did not anticipate all the sources of background error listed above, we have to recalculate the number of expected events we would expect to recover with our new cuts.

We therefore need to calculate the new N_{exp} given by

$$N_{\text{exp}} = \int_0^{x_{\max}} \int_0^{u_{\text{thresh}}(x)} \int_0^\infty \epsilon(x, u_{\min}, v_{\text{t}}) \frac{d\Gamma}{dx du_{\min} dv_{\text{t}}} dv_{\text{t}} du_{\min} dx. \qquad (3.1)$$

In order to this, we use a Monte Carlo method. For each star, we calculate the maximum detectable values for the distance to the lens, x, the impact parameter at closest approach, $u_{\min}$, and the transverse velocity of the lens, v_{t}. We then generate random values for these parameters drawing from a uniform distribution in the allowed range of values, as well as a random time of the event, t_0. We generate 2000 such random fake events per star, calculating the magnification using the linear limb-darkening model described in Section 2.2.3 and applying this magnification to the existing data flux light curves, with the correct scaling of errors for each flux point. By inputting the fake events into the actual data, we are able to fully account for all the background events and data cuts to our calculation of efficiency. If the fake event passes through all the cuts, we calculate a microlensing rate for that event from Equation 2.19:

$$\frac{d\Gamma}{dx du_{\min} dv_{\text{t}}} = 4r_{\text{E}}(x) L \frac{\rho}{M} \frac{v_{\text{t}}^2}{v_{\text{c}}^2} e^{-v_{\text{t}}^2/v_{\text{c}}^2}. \qquad (3.2)$$

We then add the rates, in effect performing the integral above to get the number of expected events, N_{exp} for each star, at the end dividing by the total number of events inputted. This is done for 5000 stars in each quarter, averaged, and scaled up to the full number of stars in that quarter. The number of expected events is

then summed up over all the quarters. This in turn is redone for each PBH mass, resulting in millions of events per PBH mass point calculated.

Following the MACHO microlensing analysis (Alcock et al., 1996), after calculating the total number of expected events for each PBH mass, the upper limit for PBH DM halo fraction in the Milky Way is set by $3/N_{\mathrm{exp}}$ at 95% confidence level, since no events are detected. This is plotted in Figure 3.4 as the solid black line. We picture the previous MACHO microlensing limits which constrain PBH DM down to $2 \times 10^{-8} M_\odot$, and the recent femtolensing limits from Barnacka et al. (2012) on the lower mass range, which go up to $4 \times 10^{-14} M_\odot$. As can be seen, after utilizing two years of Kepler data, we can already constrain an additional order of magnitude below the MACHO limits, down to $2 \times 10^{-9} M_\odot$. Our sensitivity is not as good as expected in our theoretical predictions due to the addition of stellar flares and non-Gaussian errors, which were not included in our previous calculations. However, we are optimistic in obtaining further PBH mass coverage as the Kepler data continues to be analyzed. In the best case scenario we might be sensitive to another order of magnitude below the one set here with the full extended Kepler mission, however, future missions, such as WFIRST (Green et al., 2011), might further probe some of the remaining PBH mass range once the Kepler mission is finished (as discussed in the previous chapter).

3.6   Summary and Conclusion

We present the first constraints on a new range of PBH DM based on Kepler satellite data using the first two years of publicly available lightcurves. After a first look at the lightcurves, we find unexpected sources of background error, such as stellar flares, comets, cosmic rays, and non-Gaussian errors. We therefore introduce new cuts in order to eliminate this background, primarily increasing the number of required continuous points 3 sigma above average from 4 to 5. With these new requirements to eliminate background, we find no PBH microlensing
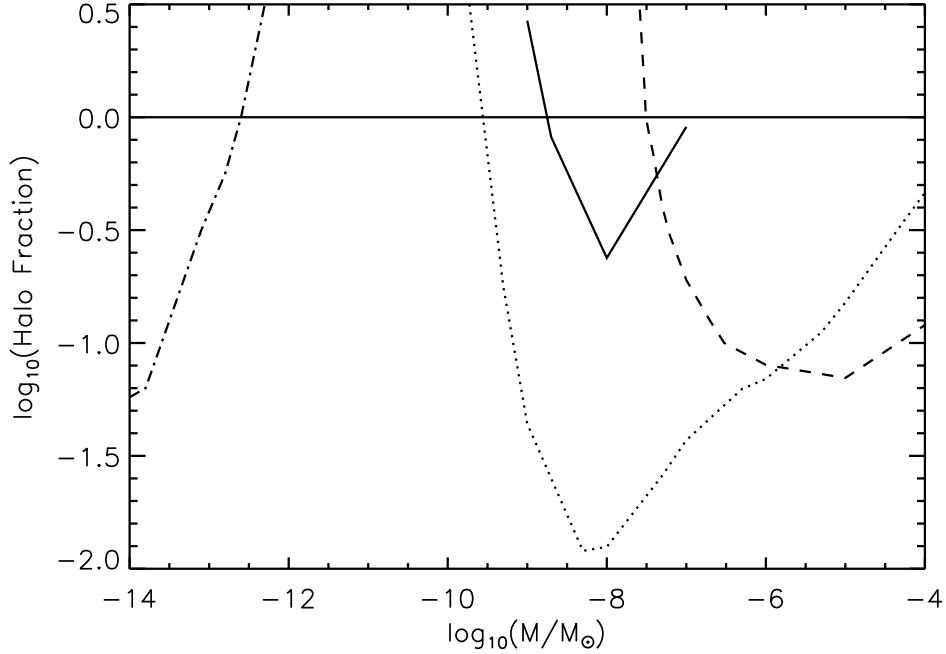
Figure 3.4 The 95% confidence level exclusion of PBH dark matter from the non-observation of PBHs. The area above the solid line is the new ruled out region based on Quarters 2-9 of the Kepler light curves. The dotted line is the theoretical limit from Chapter 2, the dashed line is previous best limit from the combined MACHO/EROS LMC microlensing surveys (Alcock et al. 1998), while the dash-dotted line represents the new limits from femtolensing (Barnacka et al. 2012). The horizontal line depicts a DM halo consisting entirely of PBHs.

candidates. In order to place constraints in the detectable PBH mass range, we therefore recalculate the number of expected events, using a Monte Carlo analysis with millions of inputted fake limb-darkened microlensing events. Based on this analysis, the PBH DM can be constrained a full order of magnitude below the existing MACHO limits, just based on the first two years of Kepler data. These constraints and sensitivity will further increase as the publicly available Kepler lightcurves are analyzed to include the full extended Kepler mission, and possible further improved with the upcoming WFIRST mission.

References

Alcock, C., Allsman, R. A., Alves, D., Axelrod, T. S., Becker, A. C., Bennett, D. P., Cook, K. H., Freeman, K. C., Griest, K., Guern, J., Lehner, M. J., Marshall, S. L., Peterson, B. A., Pratt, M. R., Quinn, P. J., Rodgers, A. W., Stubbs, C. W., Sutherland, W., & MACHO Collaboration. 1996, The Astrophysical Journal, 471, 774

Barnacka, A., Glicenstein, J.-F., & Moderski, R. 2012, Physical Review D, 86, 043001

Carr, B. J., Kohri, K., Sendouda, Y., & Yokoyama, J. 2010, Physical Review D, 81, 104019

Ciardi, D., von Braun, K., Bryden, G., van Eyken, J., Howell, S. B., Kane, S. R., Plavchan, P., Ramírez, S. V., & Stauffer, J. R. 2011, The Astronomical Journal, 141, 108

Cieplak, A. M. & Griest, K. 2013, The Astrophysical Journal, 767, 145

Green, J., Schechter, P., Baltay, C., Bean, R., Bennett, D., Brown, R., Conselice, C., Donahue, M., Gaudi, S., Lauer, T., Perlmutter, S., Rauscher, B., Rhodes, J., Roellig, T., Stern, D., Sumi, T., Tanner, A., Wang, Y., Wright, E., Gehrels, N., Sambruna, R., & Traub, W. 2011, arXiv:1108.1374G

IAU. 2013, Minor Planet Checker http://scully.harvard.edu/ cgi/CheckMP

Maehara, H., Shibayama, T., Notsu, S., Notsu, Y., Nagao, T., Kusaba, S., Honda, S., Nogami, D., & Shibata, K. 2012, Nature, 485, 478

Walkowicz, L. M., Basri, G., Batalha, N., Gilliland, R. L., Jenkins, J., Borucki, W. J., Koch, D., Caldwell, D., Dupree, A. K., Latham, D. W., Meibom, S., Howell, S., Brown, T. M., & Bryson, S. 2011, The Astronomical Journal, 141, 50

Chapter 4

Baryon Acoustic Oscillations in the Lyman-Alpha Forest

4.1 Introduction

The discovery of the accelerated expansion of the Universe by two separate Nobel-winning teams studying supernovae Ia (Riess et al., 1998; Perlmutter et al., 1999), has led to numerous astrophysical studies of this phenomenon called the dark energy. Supernovae Ia, having a known luminosity and redshift distance, can serve as "standard candles" providing a measurement of how fast they are moving away from us. Other such standard candles include cepheid variables at closer distances where the period of the stellar pulsations can be related to their luminosity, planetary nebulae using the assumption that all have similar maximum intrinsic brightness, the Tully-Fisher relation relating the rotation curve of a spiral galaxy to its intrinsic luminosity, etc. The same method can be applied with "standard rulers": objects of known size and redshift. These include ultra-compact radio sources, galaxy clusters which related Xray flux to cluster size, as well as statistical standard rulers, the most important of which are the Baryon Acoustic Oscillations (BAO) measurements.

4.2 Physics of Baryon Acoustic Oscillations

BAO are imprints on the matter distribution by sound waves in the primordial plasma in the early universe (Peebles & Yu, 1970; Sunyaev & Zeldovich, 1970). Quantum fluctuations after inflation produce initial overdensities of dark matter, radiation, and baryons. The photons and baryons evolve as a single fluid coupled by Thomson scattering. If a single overdensity is considered, the initial overdensity of this plasma will propagate outwards as an acoustic wave with a speed $c_s = c/\sqrt{3(1 + 3\rho_b/4\rho_\gamma)}$, where ρ_b and ρ_γ are the baryon and photon densities, respectively, and the ratio $3\rho_b/4\rho_\gamma$ comes about from the adiabatic initial conditions of the fluctuations. As the temperature of the universe drops, the electrons become bound to protons to form neutral hydrogen, and the photons decouple from the baryons and stream out freely. The characteristic size of how far these baryons travel due to radiation pressure can be calculated as $r_s = \int_0^{t(z_{drag})} c_s(1+z)dt \approx 150$ Mpc (Eisenstein & Hu, 1998), where z is the redshift. Since the recombination epoch does not exactly coincide with the epoch at which the baryons are released from any radiation pressure (there is still some Compton drag after the photons are released from the electrons), the integral upper limit is the time at which this drag epoch ends $t(z_{drag})$. The photons that stream out at the decoupling epoch is what is detected as the Cosmic Microwave Background (CMB).

The evolution of a single overdensity can be followed in Figure 4.1. As the baryon-photon plasma evolves in a spherical manner, the initial central dark matter density, not influenced by radiation pressure, is centralized in the middle. Eventually the dark matter falls into the baryons' gravitational wells and vice versa, which, after decoupling, produces a higher total matter density at the center of this spherical shell and a smaller total matter overdensity at $r_s \approx 150$ Mpc. The overlay of these spheres of matter overdensities produces the distribution of large scale structure that we see today. This characteristic length is therefore frozen into the matter distribution at the end of the drag epoch, and can be probed

statistically as a "standard ruler" over time.
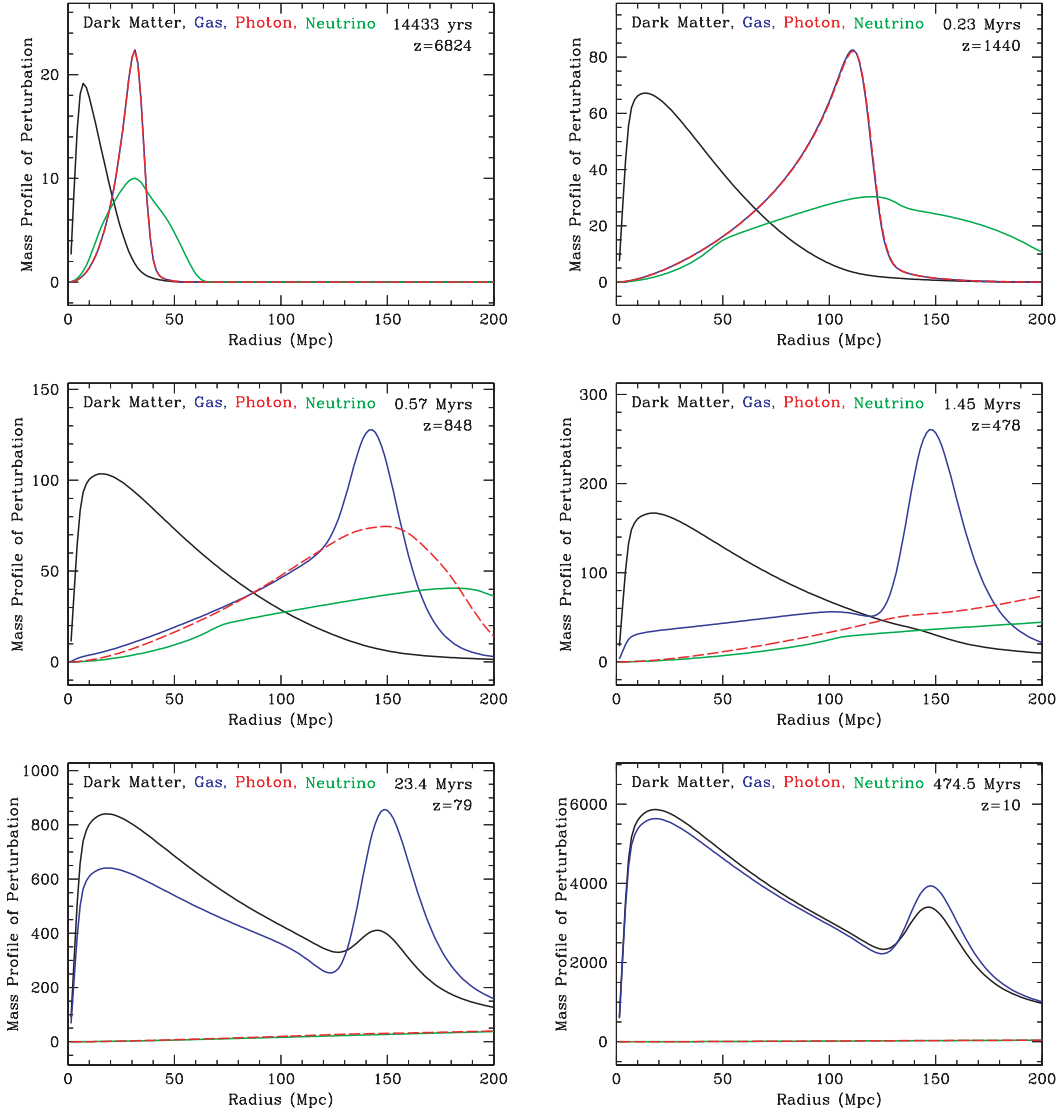
Figure 4.1 The evolution of a single overdensity - the mass radial profile vs the comoving radius. *Top left:* The baryons and photons travel outward as a single fluid, while the neutrinos stream out freely. *Top right:* The dark matter is pulled slightly outward due to gravitational interactions with the baryons. *Middle left:* The photons decouple at recombination. *Middle right:* The result is an overdensity of dark matter in the middle, and an overdensity of baryons in a shell. *Bottom left:* The baryons and dark matter eventually fall into each other's potential wells, resulting in the figure in the *Bottom right.* (Eisenstein et al., 2007)

4.3 Cosmological Parameters Measured with BAO

This standard ruler can therefore be probed in the tangential and the radial direction, giving potential constraints on the angular diameter distance, and the Hubble parameter, respectively. The Hubble parameter is defined as $H \equiv \dot{a}/a$, where a is the scale factor of the universe. Moreover, we can express the current radiation density, matter density, dark energy density, and a space-time curvature term, respectively as

$$\Omega_r = \frac{8\pi G \rho_r^{(0)}}{3H_0^2}, \quad \Omega_m = \frac{8\pi G \rho_m^{(0)}}{3H_0^2}, \quad \Omega_{DE} = \frac{8\pi G \rho_{DE}^{(0)}}{3H_0^2}, \quad \Omega_k = 1 - \Omega_r - \Omega_m - \Omega_{DE}.$$
(4.1)

Using these expressions, the Hubble parameter over time can be derived from the Friedmann equation as

$$H(z) = H_0 \sqrt{\Omega_m(1+z)^3 + \Omega_{DE}f(z) + \Omega_k(1+z)^2 + \Omega_{rad}(1+z)^4}$$
(4.2)

where $f(z)$ is the dimensionless dark energy density. This is related to the dark energy equation of state by

$$f(z) = exp(3 \int_0^z \frac{1 + w(z')}{1 + z'} dz'),$$
(4.3)

where $w(z) = w_0 + w_a z/(1+z)$ and $w = P_{DE}/\rho_{DE}$. From $H(z)$ it can be shown that in order to constrain $f(z)$ separate measurements of $H(z)$ and Ω_k are necessary. This is difficult to achieve with other standard rulers, however the BAO method provides separate measurements in the radial and tangential directions, giving $H(z)$ and $d_A(z)$, the angular diameter distance,

$$H(z) = \frac{c\Delta z}{r_{s\parallel}(z)},$$
(4.4)

$$d_A(z) = \frac{r_{s\perp}}{\Delta\theta(1+z)},$$
(4.5)

where $r_{s\parallel}(z)$ is the measured scale in the parallel direction, and $r_{s\perp}$ is the scale in the perpendicular direction. From this, the density parameter of curvature, Ω_k, is found to be

$$\Omega_k = \frac{(H(z)D'(z))^2 - H_0^2}{(H_0 D(z))^2} \tag{4.6}$$

with $D(z) = (c/H_0)(1 + z)d_A(z)$. Therefore, the BAO statistical determinations can potentially remove the degeneracy in the $H(z)$ and Ω_k measurements, providing a unique way to constrain the dark energy equation of state, not available with other standard ruler experiments.

4.4 Two-Point Statistics

4.4.1 Correlation Function

A way to detect the BAO scale in the matter distribution, is to use the correlation function, $\xi(r)$, which is related to the probability of finding overdensities at separation r above a random distribution. If one defines a matter overdensity as $\delta(r) = \rho(r)/\bar{\rho} - 1$, then the correlation function is defined as

$$\xi(r) = \langle \delta(y)\delta(y + r)\rangle \tag{4.7}$$

where the average is taken over all possible positions. If the distribution is random, then the correlation function is equal to zero. If it is positive, then the density at that separation is higher than a random distribution. The BAO signal therefore appears as a bump in the correlation function at $\sim$150 Mpc. (see lower panel of Figure 4.2 for different cosmologies)

4.4.2 Power Spectrum

Since the general relativistic equations are linear to first order, the initial cosmological perturbations are evolved by expanding them in terms of Fourier
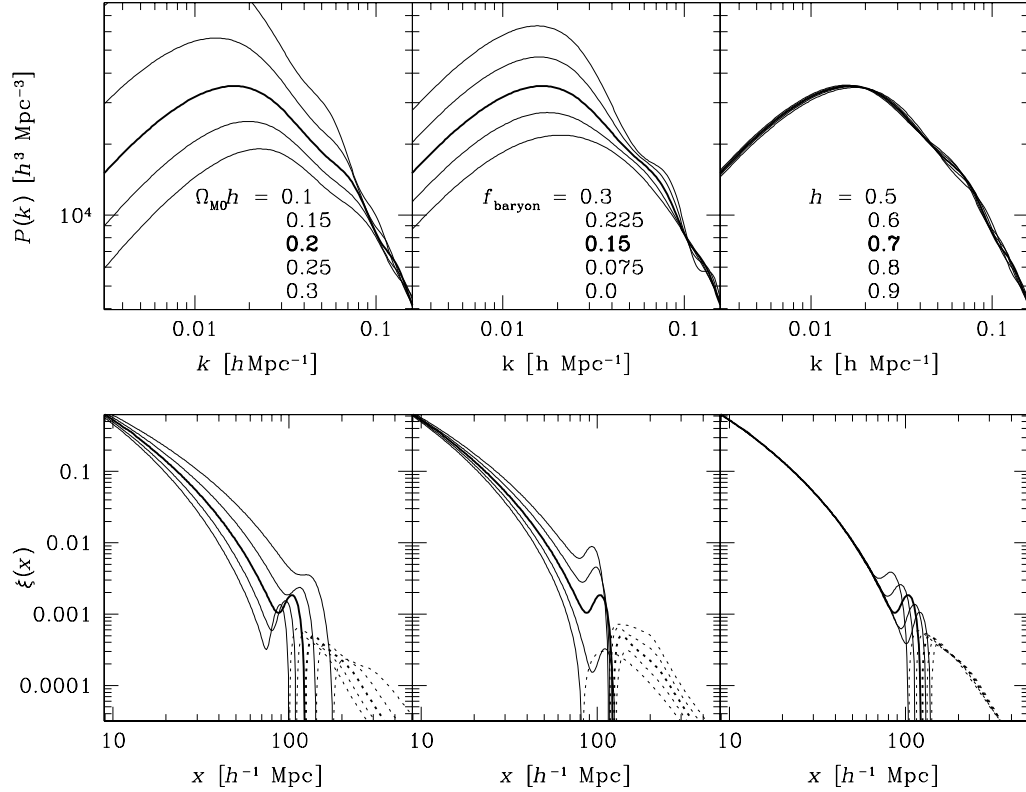
Figure 4.2 Power spectra and correlation functions in different cosmologies. *Upper panel:* BAO signal appearing as wiggles in the power spectrum. The left panel shows varying Ω_m, the middle, varying the baryon fraction $f_b = \Omega_b/\Omega_m$, while the right varying $h = H(z)/H_0$. *Lower panel:* BAO signal appearing as a peak in the correlation function, with varying cosmologies as for the upper panel. (Matsubara, 2004)

modes $\delta = \int e^{i\vec{k}\cdot\vec{r}}\delta_k d^3k$. The orthonormal modes then evolve independently. Their amplitude can then be described in terms of the power spectrum, defined as

$$\langle \delta_k \delta_{k'}^* \rangle = (2\pi)^3 P(\vec{k})\delta_D(\vec{k} - \vec{k'}). \tag{4.8}$$

If the field is statistically homogeneous, the modes are uncorrelated. The power spectrum and the correlation function are related by a Fourier transform:

$$P(\vec{k}) = \int \xi(\vec{r})e^{-i\vec{k}\cdot\vec{r}}dV. \tag{4.9}$$

The BAO signal therefore appears as a series of wiggles in the power spectrum (see upper panel of Fig 4.2). Also see Eisenstein et al. (2007) for a comparison of

Fourier and configuration space for BAO.

4.5 Measurements of BAO

4.5.1 Cosmic Microwave Background

As stated above, the Cosmic Microwave Background (CMB) arises from photons streaming towards us after decoupling from the hot plasma after recombination. Although not a direct probe of the matter fluctuations, the overdensities leave an imprint on the temperature fluctuations of the CMB. This is due to the fact that photons climbing out of deep gravitational wells (high overdensities) lose energy, becoming colder, while photons coming from underdensities gain energy, thus becoming hotter (Sachs & Wolfe, 1967). These temperature fluctuations can then be Fourier decomposed onto the two-dimensional last scattering surface, to obtain the power spectrum pictured in Figure 4.3. The wiggles that we see there-

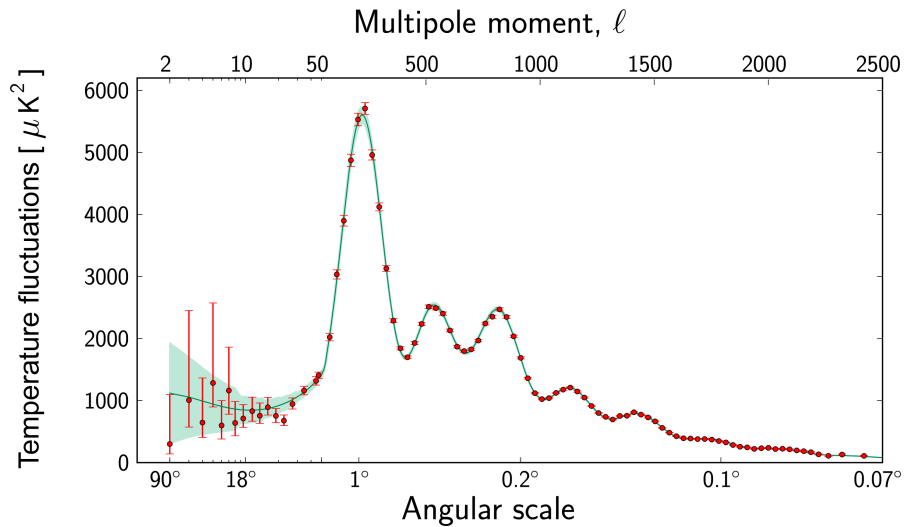**Figure 4.3** Two-dimensional power spectrum of the CMB temperature fluctuations as measured by the Planck satellite.(Planck Collaboration et al., 2013)

fore represent the acoustic oscillations at the moment of the photons decoupling. Although the BAO signal cannot be measured in 3D using the CMB, and therefore the degeneracy between $H(z)$ and Ω_k is not broken, the CMB does constrain the ratio of ρ_b/ρ_γ by obtaining an accurate photon density from the blackbody distribution of the CMB.

4.5.2 Matter Measurements

The CMB is a 2D measurement of the acoustic oscillation signal measured through the fluctuations in radiation temperature. However, since this is generated at the moment of decoupling, and not after the drag epoch, there are some differences between the radiation power spectrum and the matter power spectrum, as would be measured directly (see Figure 4.4 which pictures the peaks of the two spectra being out of phase due to velocity overshoot). The first detection of the BAO signal in the matter distribution is in the measurements of the luminous red galaxy distribution (see Figure 4.5). It has since been measured in the 6dF Galaxy Survey (Beutler et al., 2011), as well as WiggleZ (Blake et al., 2011) and updated SDSS-II data (Padmanabhan et al., 2012), and BOSS (Anderson et al., 2012). The distribution of these measurements with redshift can be seen in Figure 4.6. These measurements probe BAO at low redshift, however the BAO method really becomes powerful at higher redshift, since there is more volume to probe, and the evolution of the Fourier modes of the matter densities is more in the linear regime. Surveys of galaxies at these large volumes requires heavy telescope investment, when in fact any tracer of matter will do. 21 cm intensity mapping of neutral hydrogen is a focus of future planned radio telescopes, and could potentially measure the BAO scale at z > 6 (Mao & Wu, 2008; Rhook et al., 2009). Instead of resolving galaxies, this would map the intensity of this neutral hydrogen transition from all the galaxies over some volume.

Additionally, much focus has also been on the intergalactic medium (IGM)
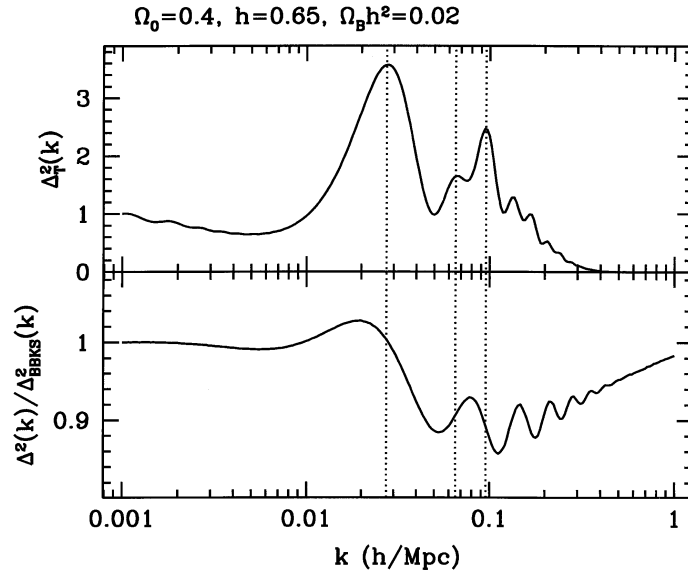
Figure 4.4 The difference between the CMB power spectrum (top panel) and matter power spectrum in large scale structure (bottom panel). Both panels picture the quantity $k^3 P(k)/2\pi^2$, with the trend taken out in the bottom panel. (Meiksin et al., 1999)

at lower redshifts in particular the neutral hydrogen which could be measured through the Lyman-alpha transition appearing in Quasar absorption spectra along the line of sight. This could be done with currently existing technology and low resolution spectra.

4.6 Measurements of BAO in the Lyman-Alpha Forest

4.6.1 Lyman-Alpha Forest

Quasars are among the most distant observable objects in the Universe and are thought to be very luminous active galactic nuclei. They are great cosmological
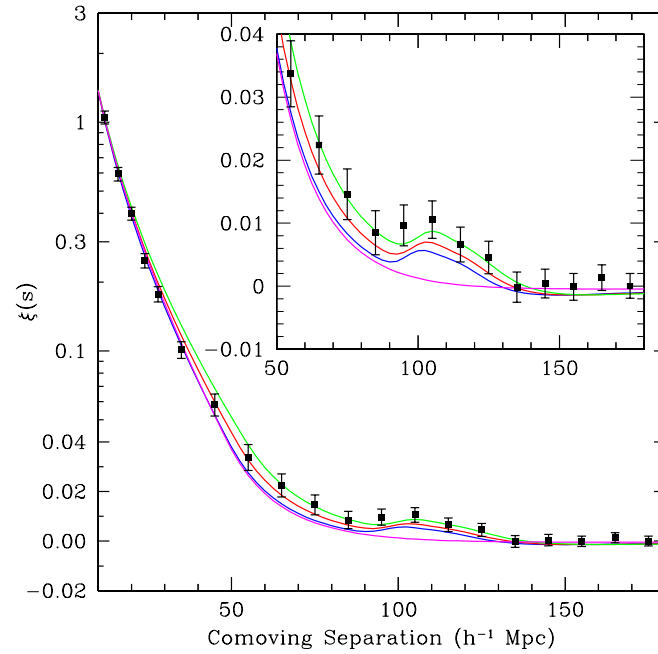
Figure 4.5 The first detection of the BAO peak in the SDSS survey Luminous Red Galaxy correlation function. (Eisenstein et al., 2005)

tools since they exist at high redshift and the light they emit probes any intervening gas as it travels towards us. The Lyman-alpha absorption of neutral hydrogen at 1216Åin particular has a large cross section. Therefore when the emission continuum of a quasar becomes redshifted to this wavelength, it will be absorbed by gas clouds along the line of sight even with small fractions of neutral hydrogen present. These series of absorption lines in a quasar spectrum are what is called the Lyman-alpha forest. In order for these lines to be visible through the Earth's atmosphere, the absorbing material has to be at redshifts of 1.7 or higher for the ultraviolet light to be redshifted to wavelengths which are not absorbed by the atmosphere. At very high redshifts the forest in turn becomes too opaque.

The relationship between Lyman-alpha absorption and the underlying matter density is nonlinear, however the physics is thought to be well-understood. The following closely follows Mo et al. (2010). The shape of each absorption line is a
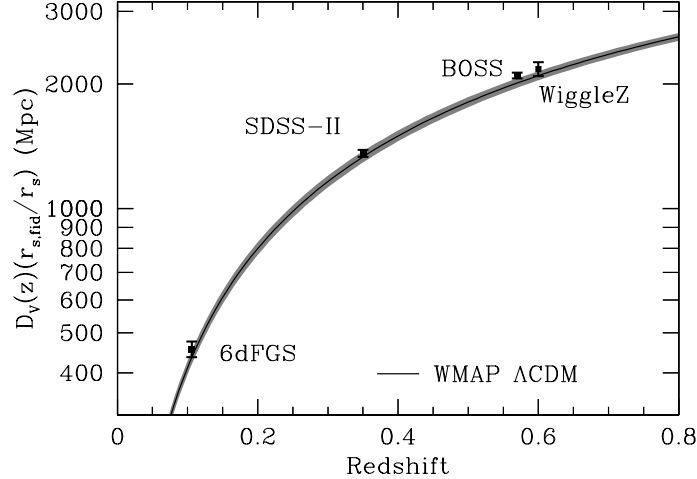
Figure 4.6 The BAO distance-redshift relation. For each measurement described in the text, the quantity $D_V(z) = [D_A(z)]^{2/3}[cz/H(z)]^{1/3}$ is plotted. The black line represents the WMAP7 ΛCDM prediction. The BOSS Lyα measurements are targeting redshifts of 2-3. (Weinberg et al., 2012)

convolution of a Lorentzian and a Gaussian profile. The Gaussian profile is due to Doppler broadening, due to the gas not being at rest with respect to the background. If the velocity distribution is Maxwellian, then the velocity distribution is

$$P(v)dv = \frac{1}{\sqrt{\pi}b}e^{-v^2/b^2}dv, \tag{4.10}$$

where b is the Doppler parameter and related to the velocity dispersion, $b = \sqrt{2}\sigma$. In general, $b^2 = 2k_BT/m + b_{turbulence}^2$. The Lorentzian profile is due to the natural broadening due to the finite lifetime of the excited state. It is described by

$$L(\nu) = \frac{1}{\pi}\left[\frac{\gamma}{(\nu - \nu_{12})^2 + \gamma^2}\right], \tag{4.11}$$

where $\gamma = A_{21}/4\pi$ and A_{21} is the spontaneous transition coefficient. The resulting

line profile is the Voigt profile

$$V(\nu) = \int_{-\infty}^{\infty} L\left[\nu\left(1 - \frac{v}{c}\right)\right] P(v) dv. \tag{4.12}$$

By fitting the Voigt profiles, the Doppler b parameters suggest a cold gas ($T \sim 10^4$K). The column densities for the Lyman-alpha forest range from 10^{12}cm^{-2}, for the resolution limit of high resolution spectra, to 10^{17}cm^{-2}, above which the gas becomes optically thick.

In order to measure a power spectrum which could be related to the underlying matter power spectrum, what is measured is the flux at each pixel. This is related nonlinearly to the optical depth by $F = e^{-\tau}$, which in turn can be expressed in terms of the neutral hydrogen density,

$$\tau(\nu_0) = \int_0^{\infty} n_{HI}(x)\sigma_{Ly\alpha}(\nu)\frac{dx}{1+z}, \tag{4.13}$$

$$\nu = \nu_0(1+z)\left[1 + \frac{v(x)}{c}\right],$$

where $\sigma_{Ly\alpha}$ is the Lyman-alpha absorption cross-section at frequency ν, given by the Voigt profile $V(\nu)$. The optical depth can be related to the underlying dark matter by performing evolving the gravitational equations, hydrodynamical, thermal, and ionization states of the gas, to give n_{HI}, v(x), and b(x).

However, one can understand the underlying physics by the following simple analysis. Since the gas dynamical time scales are much longer than recombination and ionization time scales, one can assume a photoionization equilibrium where

$$n_{HI}(x) = n_H^2(x)\alpha_{H+}(T)/\Gamma_{\gamma,HI}, \tag{4.14}$$

where α_{H+} is the recombination coefficient, whereas $\Gamma_{\gamma,HI}$ is the photoionization rate.

Additionally, assuming hydrogen traces the underlying baryon density, $n_H(x) = \overline{n}_H(x)[1 + \delta_b(x)]$. Also, assuming adiabatic expansion, $T = T_0(1 + \delta_b)^{\Gamma-1}$, $\Gamma \approx 5/3$, where T_0 and Γ depend on the thermal and ionization history of the gas. This

relationship is thought to have a $5 - 10\%$ scatter and increases for high densities (Hui & Gnedin, 1997). Furthermore, neglecting thermal broadening and radiation damping, one arrives at the Fluctuating Gunn-Peterson Approximation (FGPA) (Weinberg et al., 1997; Croft et al., 1998)

$$\tau(\nu_0) = 0.172(1 + \delta_b)^{2.7-0.7\Gamma} \left(1 + \frac{dv_{(x)}}{H(z)dz} \right)^{-1} \left(\frac{1+z}{4} \right)^6 \left(\frac{H(z)/H_0}{5.51} \right)^{-1} h^{-1} \times$$
$$\left(\frac{\Omega_b h^2}{0.0125} \right)^2 \left(\frac{T_0}{10^4 K} \right)^{-0.7} \left(\frac{\Gamma}{10^{-12} s^{-1}} \right)^{-1}, \qquad (4.15)$$

relating the Lyman-alpha optical depth directly to the underlying density field. The gas density field therefore traces the dark matter density field, down to the scale of the Jeans length, where the gas pressure supports gas against gravity. The above is a good approximation for low densities and high redshifts, however it ignores shock heated gas and thermal broadening. It does demonstrate how the Lyman-alpha forest flux can be treated as a continuous field sampled as pixels to calculate the correlation function or power spectrum which traces the dark matter power spectrum. Since pressure forces are subdominant on large scales, it is thought that the neutral hydrogen density closely traces the total matter on BAO scales.

4.6.2   Redshift Space Distortions and Bias

The picture is further complicated by redshift space distortions, which is the effect of the peculiar velocities of the gas on the estimated distance (redshift) of the gas. For example gas that is moving away from us towards an overdense region will appear farther than it actually is, while the gas on the other side of the overdensity will be moving towards us, and thus appearing closer. Depending on the size of the overdensity and the peculiar velocity, the overdensity will either appear elongated or squashed along the line of sight. This distorted power spectrum is therefore related to the underlying real space one by (Kaiser, 1987)

$$P_{redshift}(\overrightarrow{k}) = P_{real}(k) \left[1 + \beta \mu_{\overrightarrow{k}}^2 \right]^2 \qquad (4.16)$$

where $\mu_{\vec{k}} = \hat{z} \cdot \hat{k}$, the cosine of the angle between the line of sight and $\vec{k}$. The overdensities in redshift space appear larger than in real space. If we decompose these into Legendre polynomials, we obtain

$$\left[1 + \beta \mu_{\vec{k}}^2\right]^2 = \left[1 + \frac{2}{3}\beta + \frac{1}{5}\beta^2\right] P_0(\mu_{\vec{k}}) + \left[\frac{4}{3}\beta + \frac{4}{7}\beta^2\right] P_2(\mu_{\vec{k}}) + \frac{8}{35}\beta^2 P_4(\mu_{\vec{k}}).$$
(4.17)

Therefore blindly measuring P(k) averaged over all directions will actually be measuring

$$P^{(0)}_{redshift}(k) = \left[1 + \frac{2}{3}\beta + \frac{1}{5}\beta^2\right] P(k) = C_0 P(k).$$
(4.18)

Similarly, $\xi_0(r)_{redshift} = C_0 \xi_{real}(r)$.

In practice, there is also a linear bias b between the flux power spectrum and the underlying dark matter power spectrum, producing the final relationship

$$P_F(\vec{k}) = b^2 \left[1 + \beta \mu_{\vec{k}}^2\right]^2 P_{DM}(k).$$
(4.19)

Therefore, one needs to understand β, the redshift space parameter, which is influenced by how smooth the gas is in the IGM, the pressure, and the temperature history of the gas, as well as b, the bias parameter, influenced by the mean absorption level of the gas, in order to fully measure the underlying dark matter power spectrum. These are the main parameters which will have to be understood in order to fully account for the systematics of the BAO measurements in the Lyman-alpha forest. From here on b will now represent the bias parameter for the rest of the thesis, and not the Doppler parameter described in the previous section.

4.6.3 Past Studies, Detection, and Motivation

White (2003) first suggested the possibility of measuring BAO in the Lyman-alpha forest in the SDSS survey, while McDonald & Eisenstein (2007) estimated the potential of such a survey specifically for BOSS, basing their analysis on previous studies by McDonald (2003) on lower scales. McDonald (2003) was the first to

calculate the b and β parameters using hydro-PM simulations, where the temperature - density relation is assumed as above, and shocks and temperature evolution of the gas is ignored. He obtained the values of $\beta \sim 1.47$ and $b \sim 0.13$ at $z \sim 2.25$ which have since been used for mock quasar spectra. Slosar et al. (2009) presented the first simulations of the BAO scale in the Lyman-alpha forest using N-body dark-matter-only simulations, and using the above FGPA by matching the amplitude of the optical depth with that of the observed mean flux in quasar spectra data. They found that the Lyman-alpha flux provides a good tracer of the dark matter density field on the BAO scale, with $\beta \sim 1$ and a scale-invariant bias of $b \sim 0.2$. Subsequently this was followed by White et al. (2010) with similar simulations, but with better resolution. Their results follow the previous scale-invariant bias measurements.

There has also been much progress in terms of experimental results. Slosar et al. (2011) reported the first 3D correlation function measurement of the flux in the quasar absorption spectra from the BOSS survey. He found a lower preferred β (0.44-1.2) and a higher measurement of b than those predicted by the above simulations. This was postulated to be due to the presence of Damped-Lyman-alpha systems, which skew the Lyman-alpha forest measurements, metal lines, gas that is smoother than expected, or a misunderstanding in the modeling of pressure in the hydro-PM codes.

The first BAO detection in the Lyman-alpha forest from the BOSS survey quasar spectra was announced by Busca et al. (2013) late last year. The position of the peak was announced as a 4σ measurement. The position of the peak was well-modeled, however their mock spectra generated by FGPA did not fully model the shape of the peak. The measurement of the BAO peak was improved to 5σ by Slosar et al. (2013) earlier this year.

Due to such advancements in the measurement of the BAO peak in the Lyman-alpha forest, our main motivation is to fully understand any systematics involved in such a measurement, so that the method could be further developed

with better precision. We are especially interested in understanding the bias of the flux with respect to the underlying density field at the BAO scale, the redshift distortion parameter β which is determined by the temperature history of the gas, as well as the shape and position of the BAO peak. While b and β determine the large-scale power, their values are set from small scale physics, which can more fully be probed with large hydrodynamic simulations which include shock heating and temperature evolution of the gas. Using such a simulation the temperature-density approximation can be fully probed at the BAO scale. This will aid in modeling the shape of the BAO peak, in order to better fit for the position of the peak, thus improving the precision of the measurement. We therefore analyze a full hydrodynamic simulation of the Lyman alpha forest to better understand the effect of the FGPA approximation at the BAO scale, as well as any systematics involved, building upon the work done with hydro-PM and dark-matter-only simulations described above.

4.6.4   Simulations

For our analysis we use hydrodynamic cosmological simulations run by M. Norman, P. Paschos, and R. Harkness, using the code ENZO (Norman et al., 2007). The code evolves dark matter, primordial hydrogen and helium gas in an expanding universe with periodic boundary conditions. The baryonic matter is modeled by Euler equations, evolving on a grid. Energy source and sinks are included due to radiative cooling and heating, as well as changes in the ionization state of the gas. The Piecewise Parabolic Method (PPM) is used for the ideal gas dynamics, and the species abundance is solved by integrating the rate equations which include the radiative and collisional processes. The radiation fields, which control the ionization state of the gas, are evolving but spatially homogeneous. The dark matter is evolved as a collisionless phase fluid, obeying the Vlasov-Poisson equation, using the particle-mesh algorithms for the collisionless N-body dynamics.

The baryonic and dark matter components are coupled through a gravitational field, and the gravitational potential is computed by solving the Poisson equation using FFTs. See Norman et al. (2007) for a full description of ENZO.

We have two simulations, both with a flat ΛCDM cosmology, with WMAP5 concordance parameters: $\Omega_b = 0.043$, $\Omega_{DM} = 0.207$, $\Omega_\Lambda = 0.75$, h =0.72, $\sigma_8 = 0.8$, n=0.95. The initial conditions were read in as a Gaussian random field using the baryon and dark matter transfer functions generated by CAMB (Lewis et al., 2000) at a redshift of 99. One simulation evolves the baryons on a 2048^3 grid with a resolution of 330 kpc, with 614.4 comoving Mpc on a side. The dark matter is evolved as 2048^3 particles. The second simulation is the same, but with better resolution, using a 4096^3 grid, with 165 kpc resolution. The larger simulation therefore approaches the resolution needed to resolve the gas, while at the same time maintaining 4 modes on the BAO scale inside the volume. The data dumps were generated at three redshifts: z=3, z=2.74, and z=2.5, with seven cubes per redshift dump, representing the dark matter, baryons, neutral hydrogen densities, the three cubes for the gas peculiar velocities, and temperature of the gas. In order to understand all the analysis involved, we start with the smaller simulation which is less computation intensive.

Synthetic neutral hydrogen spectra were generated using the method developed by Zhang et al. (1997), where the optical depth is computed from equation 3.12, ignoring the Lorentzian contribution due to the low column densities of neutral hydrogen at these redshifts. Also parametrizing to order v/c, the optical depth can be generated by

$$\tau_\nu(z) = \frac{c^2 \sigma_0}{\sqrt{\pi} \nu_0} \int_z^{z_0} \frac{n_{HI}(z')}{b} \frac{a^2}{\dot{a}} \exp\left\{ -\left[(1+z')\frac{\nu}{\nu_0} - 1 + \frac{v}{c} \right]^2 \frac{c^2}{b^2} \right\} dz \qquad (4.20)$$

(Zhang et al., 1997; Bi et al., 1995). The integrated optical depth is therefore computed using this equation along the line of sight.

We start the analysis by looking at the smaller resolution simulation, and generating 5000 spectra distributed randomly on the face of the cube, with the

lines running parallel along the side of the cube, with 2048 pixels each. The mean
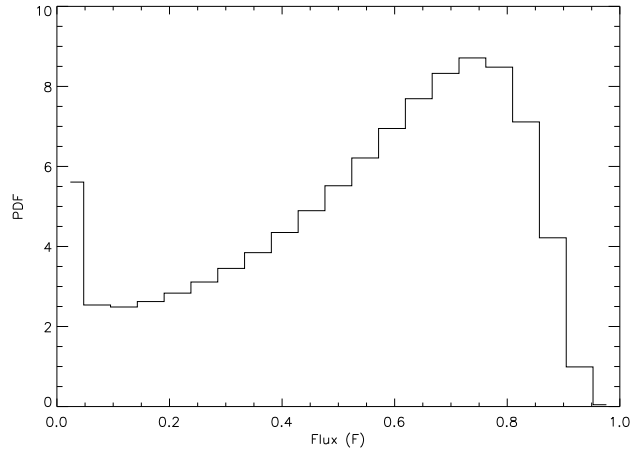

Figure 4.7 The flux PDF, binned in equal flux bins, where $F = e^{-\tau}$ at $z = 3$.

flux as measured in the 5000 lines of sight is $\bar{F} = 0.54$, which is in close agreement, although slightly smaller than that predicted by observations (McDonald et al., 2005) where $\ln \bar{F}(z) = \ln(0.8) \left[(1+z)/3.25 \right]^{3.2}$. The flux Probability Distribution Function (PDF) is also pictured in Figure 4.7. The PDF seems more evolved than that of smaller ENZO simulations at the same redshifts (Regan et al., 2007).

4.6.5 Work in Progress: Correlation Functions

We proceed to calculate the three-dimensional correlation function for the dark matter and gas densities over the whole cube. We have developed two ways in which to do this. The first way is to calculate a Fourier Transform along the line-of-sight for each sightline, multiply two sight lines together, while keeping track of their perpendicular separation, and then Fourier Transform back the result. This effectively calculates the correlation function in the parallel direction, and allows us to then multiply all the points together along the perpendicular direction, binning them into bins of width equal to the length of the box divided by the number of pixels. We then sum the resulting products in each bin, keeping track of the

number of the products per bin. This in effect gives us a correlation function in two dimensions, so we then proceed to again bin the correlation function into a full-angular averaged correlation function. The second way is the brute-force method, which is more computationally intensive. It is done by calculating the product of each pair of points, summing them and averaging per separation bin. Both yield the same results at the BAO scale in our periodic box simulation. The correlation functions computed by using the first method are pictured in Figure 4.8 and Figure 4.9.
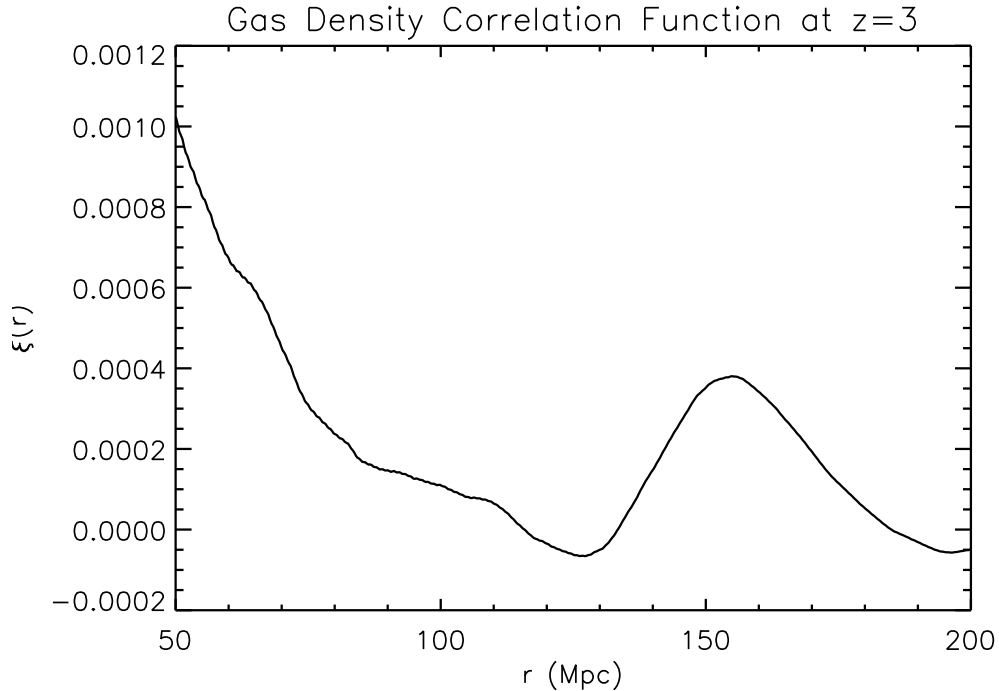
Figure 4.8 The gas density correlation function, using all the pixels in the cube which amounts to 2048^2 sightlines.

We can see that the gas density traces the dark matter density very closely. We measure the BAO peak of the dark matter correlation function at 155.1 Mpc, while the gas density peak at 154.8 Mpc. This is done by fitting a Gaussian fit to the BAO peak for each measurement. As expected, the gas and dark matter density at these scales trace each other very well, however, as will be addressed later, the
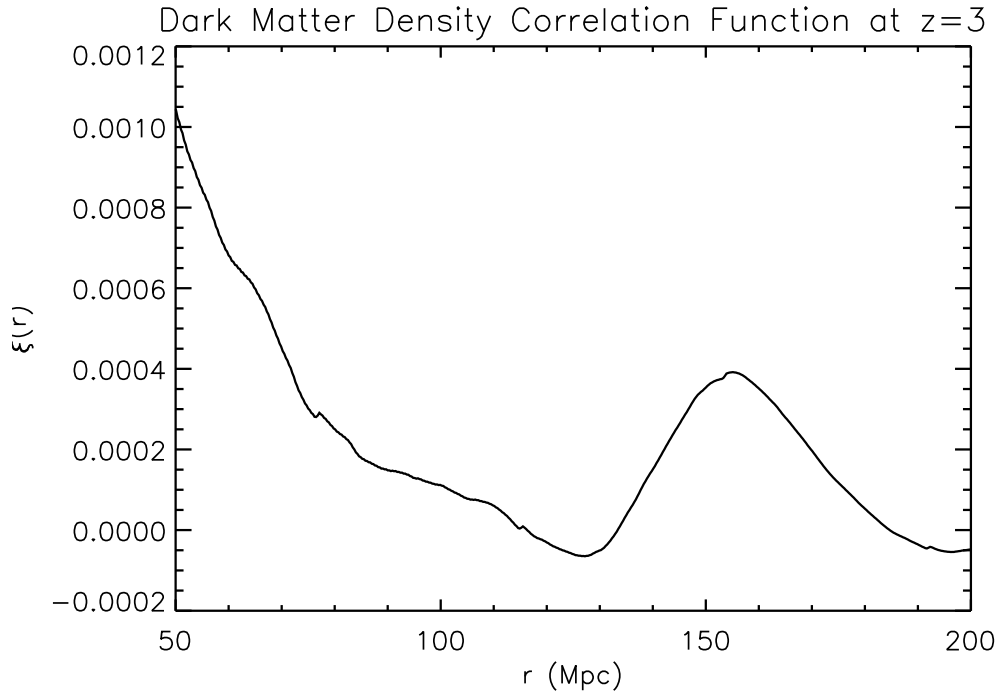
Figure 4.9 The dark matter density correlation function, using all the pixels in the cube which amounts to 2048^2 sightlines.

overall scale of the BAO peak seems too high in both of the cubes as compared to linear theory. Due to the question of validity of the results of the simulations, we do not proceed to compute the errors on this BAO peak measurement. In order to understand the significance of the detection of the peak, there are two ways in which error bars could be computed. The first way is a boot-strap method through random sampling of the lines of sight with replacement, recomputing the correlation function using the remaining sample, and iterating this multiple times to understand the scatter. The second way is to calculate the standard deviation at each point based on the number of pairs that go into each point in the correlation function. This would however underestimate the true error.

We next calculate the three-dimensional correlation function of the flux of the 5000 lines of sight we generate as described in the previous section. This now includes the peculiar velocities and therefore the redshift-space distortions.

The shape of the peak has changed dramatically, however the BAO peak is still measured at 155.1 Mpc. Assuming that the flux - dark matter relationship is not influenced by the original dark matter BAO peak being higher than expected (as will be discussed later), it seems that the position of the peak does not change between the flux and underlying dark matter correlation functions, providing for a robust BAO position measurement. For a more precise measurement however, the shape of the peak itself would have to be modeled, and fit properly in order to ensure accuracy. For this it is clear that the differences between Figure 4.9 and Figure 4.10 have to be fully understood by studying the bias and redshift space distortion parameters.
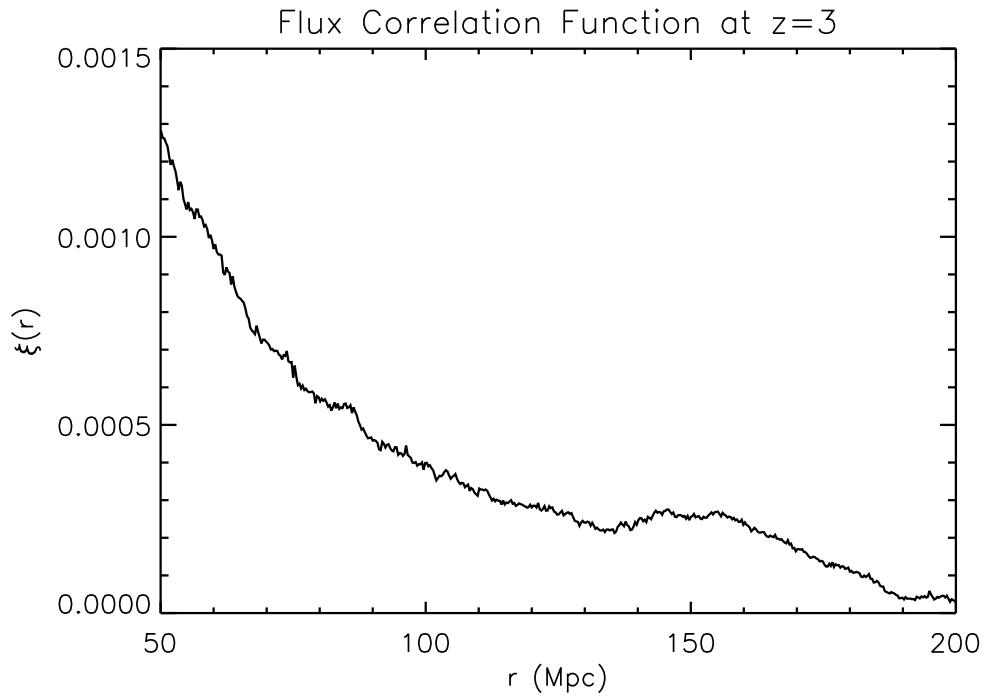
Figure 4.10 The flux correlation function, using 5000 sightlines.

4.6.6 Work in Progress: Bias and Redshift Space Distortion Parameters

If we plot the ratio of the three-dimensional flux correlation function to the underlying dark matter, we obtain in effect the value of $b^2 \left[1 + 2/3\beta + 1/5\beta^2\right]$, which is plotted in Figure 4.11. Whereas previous studies (Slosar et al., 2009;
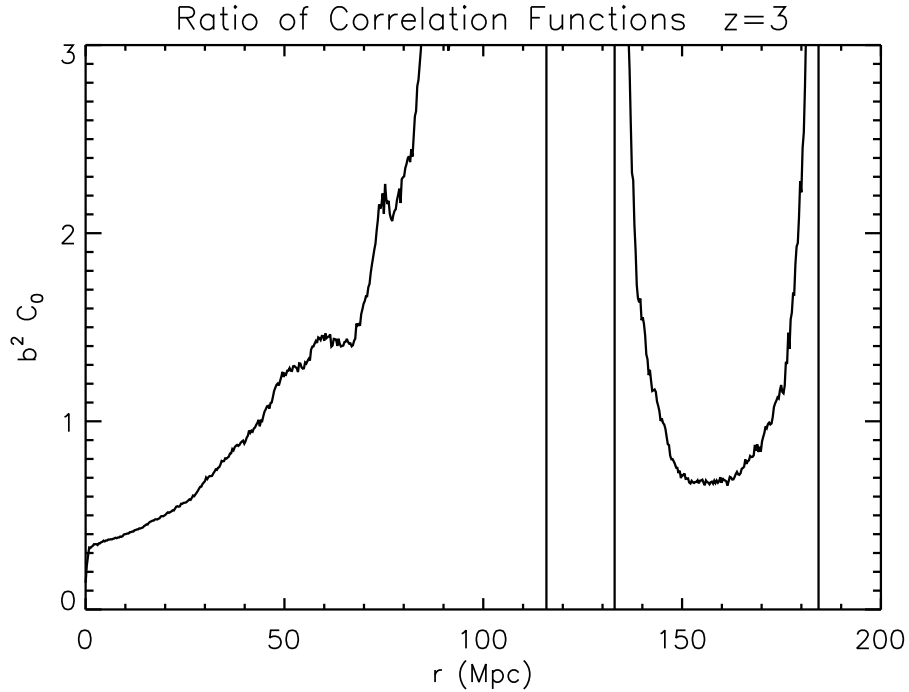
Figure 4.11 The ratio of the angular-averaged flux to dark matter correlation functions.

White et al., 2010) found the values of b and β to be scale independent, we see that they widely vary, with less variance on smaller scales and just around the BAO scale. Provided this conclusion remains, after the dark matter BAO peak problem is resolved, this would be an interesting result for the BAO measurements. If we assume $\beta \sim 1$ as seen in the previous studies, we find that $b \sim 0.27$ on small scales in agreement with the above measurements. However, as can be seen, this varies widely as we go to higher scales. Since we cannot quite trust the results of

this simulation, the analysis would have to be redone more carefully in a future simulation with starting conditions which more closely match theory (see below).

4.6.7   Work in Progress: Power Spectra

We next calculate the three dimensional power spectra for four of the cubes, the dark matter, gas density, neutral hydrogen density, truncated neutral hydrogen density expressed as $1 - e^{-\delta_{HI}}$, and temperature in Figure 4.12. This is done by performing a three-dimensional Fast Fourier Transform (FFT), taking the absolute value squared at each point, and binning the result similarly to the angular-averaged correlation function. This results in the full three dimensional power spectrum with respect to k [1/Mpc], where $k_{\min} = 2\pi/(\text{length of box in Mpc})$. We
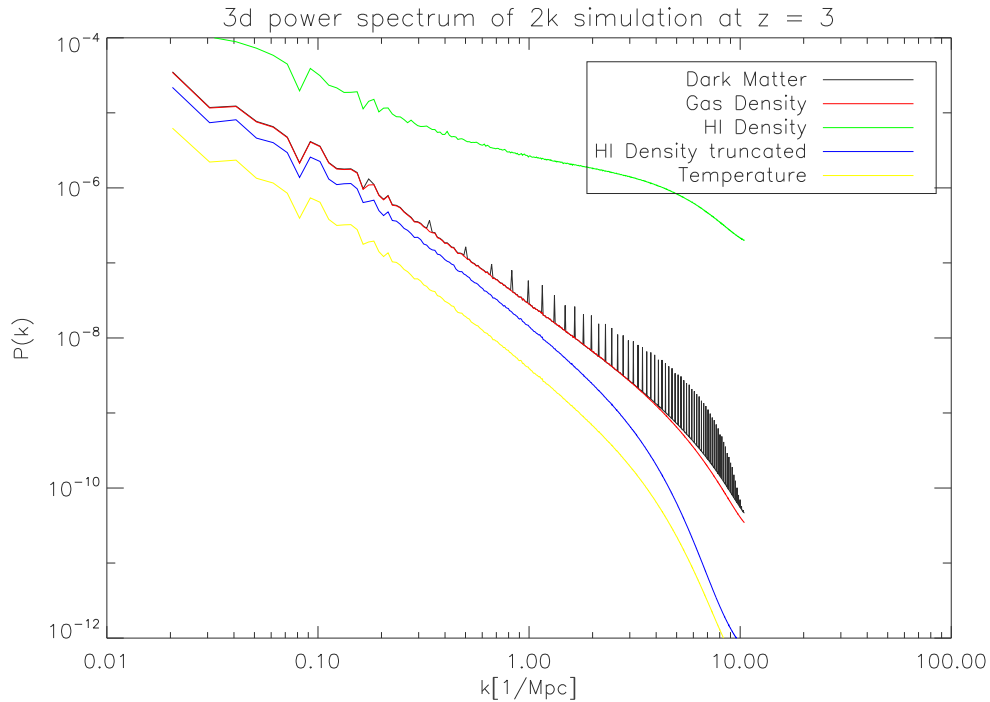

Figure 4.12 The angular-averaged power spectrum for dark matter, gas density, neutral hydrogen density, truncated neutral hydrogen density expressed as $1 - e^{-\delta_{HI}}$, and temperature for the full 2048^3 simulation at redshift $z = 3$.

can see that the gas density, and the truncated neutral hydrogen density follow the

dark matter density very well at large scales, with some constant bias factor. The scale-dependent parameter β which we find above arises from the transformation from the neutral hydrogen density field to the flux field when peculiar velocities are taken into account.

4.6.8 Work in Progress: Complications

However, in order to trust our results, we need to address some challenges we have encountered with our simulations. The first of them is already pictured in Figure 4.12. We see a series of peaks in the dark matter power spectrum pictured as the black line. This was, we found a defect in the dark matter tile boundaries of the simulation. Since the dark matter is not evolved on a grid in ENZO, like the baryons are, the dark matter particle positions and velocities are the true state simulation variables, however, when the dark matter density was computed for output purposes, there was an incorrect treatment at the boundaries. This has since been fixed in the ENZO output.

There is however another complication we encountered, having to do with the dark matter as well. In Figure 4.13 we picture again the dark matter three dimensional power, however this time along with the linear theory predicted by the CAMB program (Lewis et al., 2000). We do this by inputting initial conditions of the simulation into the CAMB setup, which evolves the total linear matter power spectrum. The normalization is adjusted to give the value of σ_8 inputted into the simulation (which is the normalization of the matter power spectrum on scales of $8h^{-1}\mathrm{Mpc}$ at the current redshift). There is also a factor of $(2\pi/(\text{length of box in Mpc}))^3$ difference between the power spectrum calculated from the ENZO box using the IDL definition of FFT which we use, and the power spectrum result of the CAMB program.

Whereas a tilt in the power spectrum is expected due to nonlinear evolution over time, the amplitude seen in the wiggles are a lot bigger than that expected by

Figure 4.13 The angular-averaged power spectrum for dark matter and baryons for the full 2048^3 simulation at redshift $z = 3$, compared to that predicted by linear theory as calculated by the program CAMB.

linear theory. If we plot the dark matter correlation function against that predicted by CAMB in Figure 4.14, we also find a BAO peak that is bigger in amplitude than that predicted by linear theory. Since the BAO is at the scales that are large enough to be described by linear theory, especially at redshift of $z = 3$, we do not expect such a big discrepancy.

We therefore decided to probe further, and investigate the conditions at the initial redshift dump of the simulation, which we plot in Figure 4.15 and Figure 4.16. One can see that even in the initial conditions, without any time for nonlinear evolution to take place, the dark matter does not follow the dark matter power spectrum that was inputted into the simulation.

Figure 4.14 The angular-averaged correlation function for dark matter for the full 2048^3 simulation at redshift $z = 3$, compared to that predicted by linear theory as calculated by the program CAMB.

4.6.9 Future Work and Tests

After many tests, we decided to rerun the initial conditions to the simulation from scratch and sent the exact initial conditions to Professor Michael Norman's group to rerun the code. To our surprise, the new simulation, with the same set of initial parameters as before, returned the correct dark matter power spectrum as predicted by linear theory! This new simulation is pictured in Figure 4.17. The normalization of the power spectrum is correct as well. Our conclusion is therefore that in the previous simulation, the baryon power spectrum must have been read in twice, for the dark matter as well.

We are therefore hopeful that a new simulation can be rerun with the BAO peak matching the linear theory in the dark matter to test the results we obtained. As part of future work, we will also test to see whether the 4k simulation, with
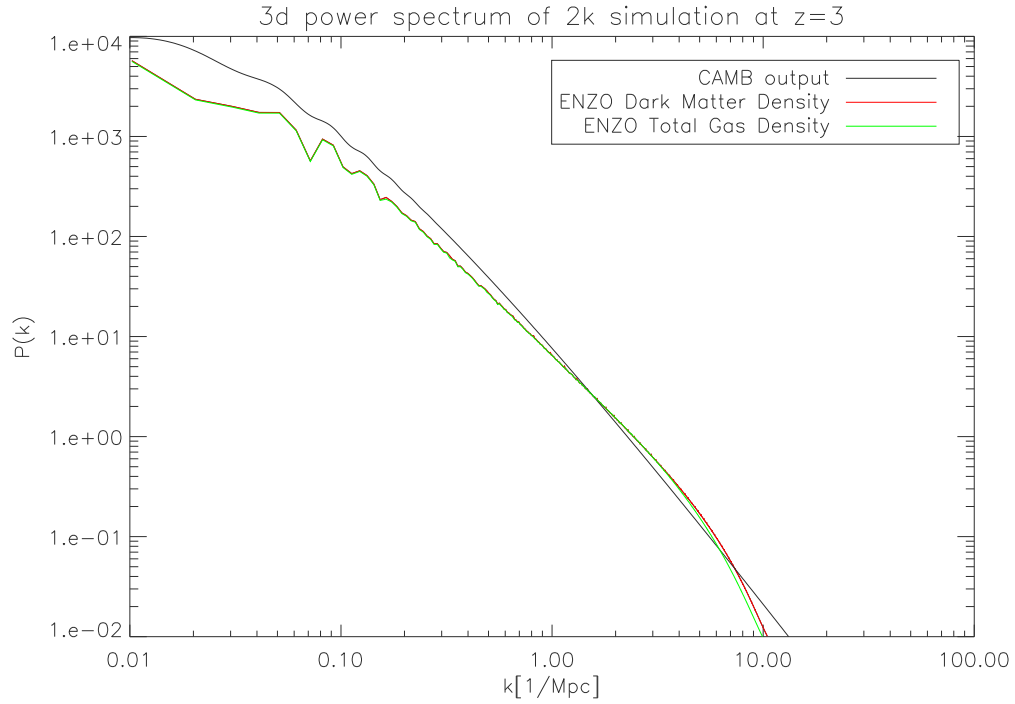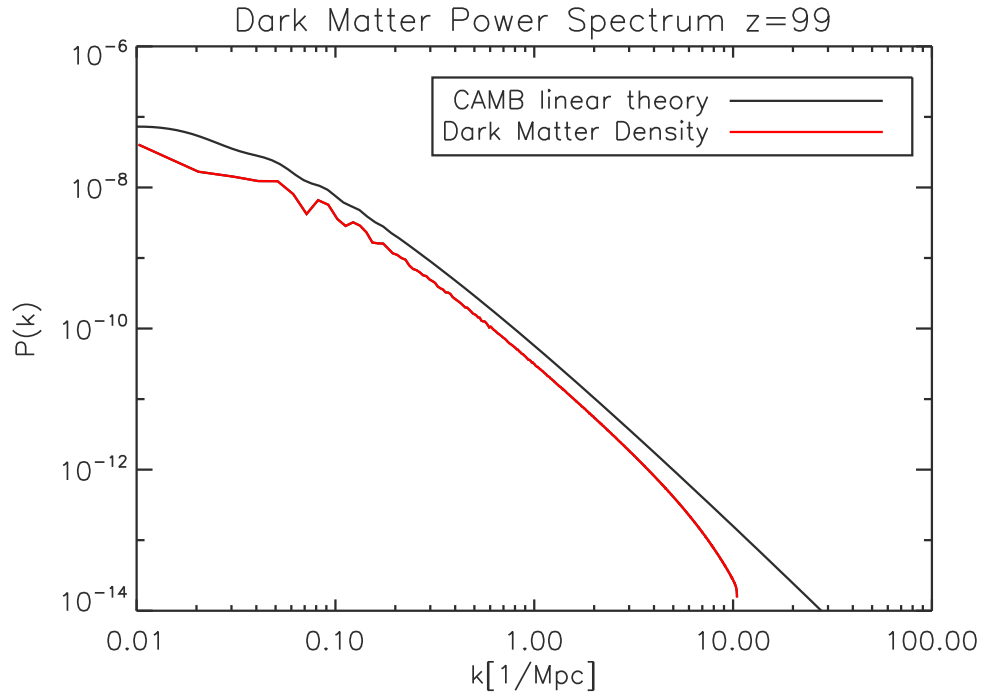
Figure 4.15 The angular-averaged power spectrum for dark matter for the full 2048^3 simulation at redshift $z = 99$, compared to that predicted by linear theory as calculated by the program CAMB.

higher precision, has the same problem with the BAO peak not matching the expected one.

4.7   Conclusion

In this chapter we have set out to understand the underlying systematic effects of a Baryon Acoustic Oscillations measurement in the Lyman-alpha forest in Quasar absorption lines. Although in the past, there has been much analysis of this measurement using dark matter only simulations, our aim is to fully understand the bias and redshift space parameters, set by small scale physics of the gas, which can more fully be probed with hydrodynamic simulations. Using the hydrodynamic ENZO simulations, we have calculated the dark matter and flux correlation
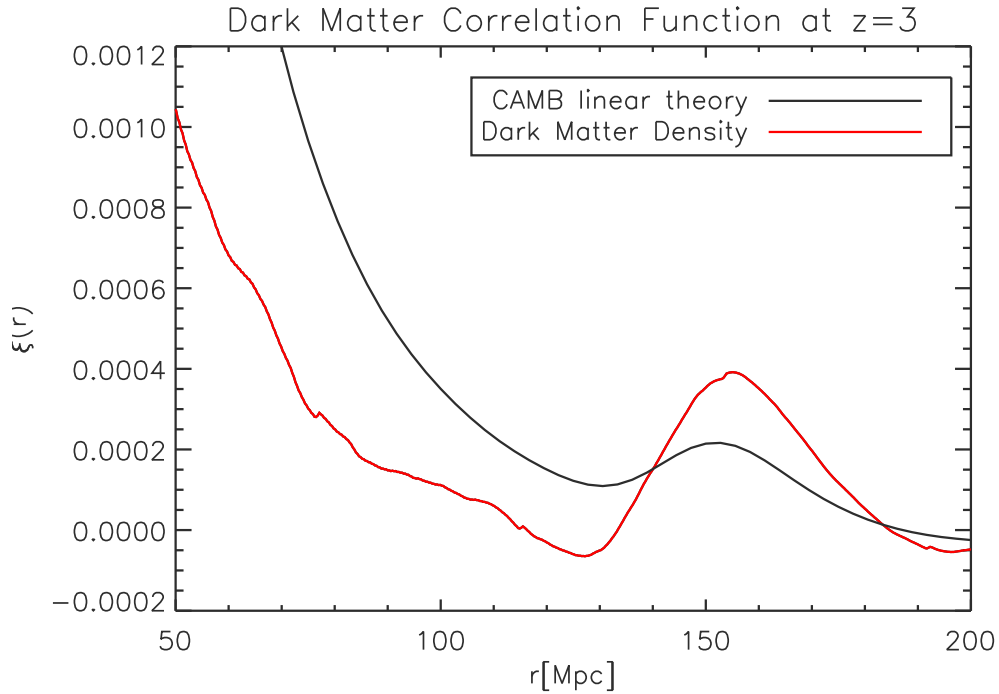
Figure 4.16 The angular-averaged correlation function for dark matter for the full 2048^3 simulation at redshift $z = 99$, compared to that predicted by linear theory as calculated by the program CAMB.

functions and found that the measurement of the BAO peak in the absorption lines traces that of the underlying dark matter. We have also attempted to calculate the bias and redshift space parameters, however such an analysis will have to be redone in the future, with a more robust simulation which more accurately traces the expected theory. We have set initial conditions for such a simulation, and we hope that we will be able to contribute to a better understanding of the shape and size of the BAO peak in the Lyman-alpha forest. This measurement by the BOSS collaboration (Busca et al., 2013; Slosar et al., 2013) is already a contributing dark energy standard ruler measurement at intermediate redshifts, and increasing its accuracy will further increase our knowledge of the expansion history of our Universe.
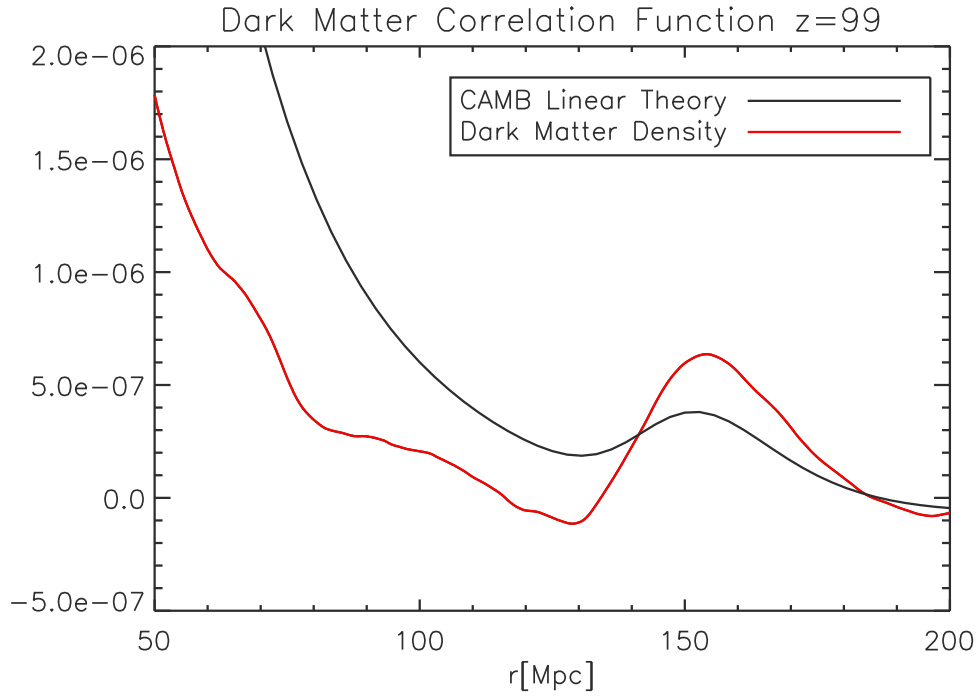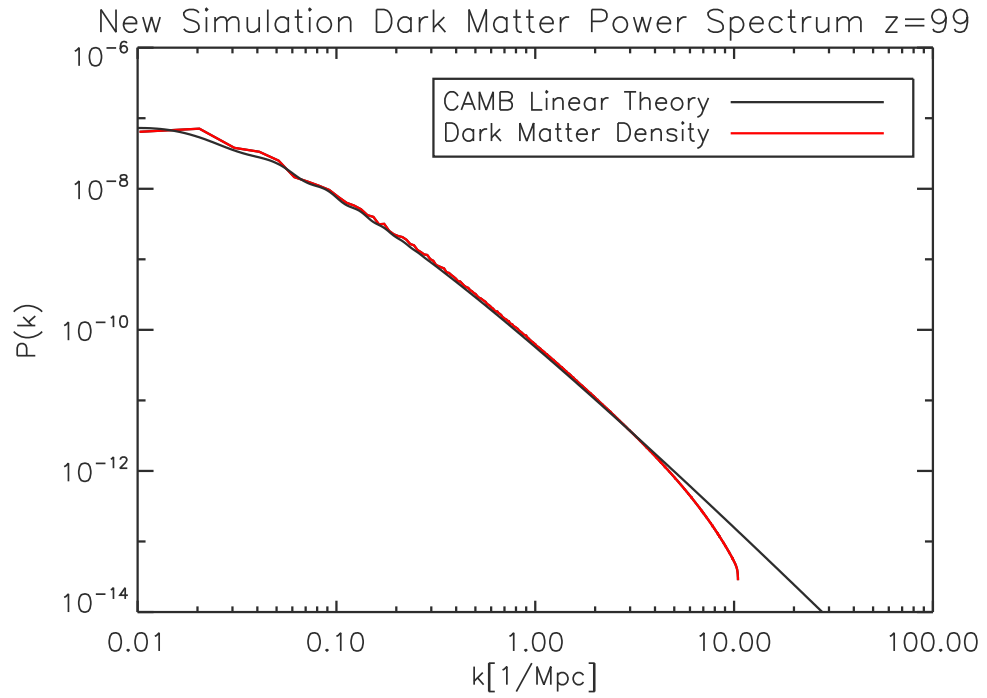
Figure 4.17 The angular-averaged correlation function for dark matter for the new full 2048^3 simulation at redshift $z = 99$, compared to that predicted by linear theory as calculated by the program CAMB.

References

Anderson, L., Aubourg, E., Bailey, S., Bizyaev, D., Blanton, M., Bolton, A. S., Brinkmann, J., Brownstein, J. R., Burden, A., Cuesta, A. J., da Costa, L. A. N., Dawson, K. S., de Putter, R., Eisenstein, D. J., Gunn, J. E., Guo, H., Hamilton, J.-C., Harding, P., Ho, S., Honscheid, K., Kazin, E., Kirkby, D., Kneib, J.-P., Labatie, A., Loomis, C., Lupton, R. H., Malanushenko, E., Malanushenko, V., Mandelbaum, R., Manera, M., Maraston, C., McBride, C. K., Mehta, K. T., Mena, O., Montesano, F., Muna, D., Nichol, R. C., Nuza, S. E., Olmstead, M. D., Oravetz, D., Padmanabhan, N., Palanque-Delabrouille, N., Pan, K., Parejko, J., Pâris, I., Percival, W. J., Petitjean, P., Prada, F., Reid, B., Roe, N. A., Ross, A. J., Ross, N. P., Samushia, L., Sánchez, A. G., Schlegel, D. J., Schneider, D. P., Scóccola, C. G., Seo, H.-J., Sheldon, E. S., Simmons, A., Skibba, R. A., Strauss, M. A., Swanson, M. E. C., Thomas, D., Tinker, J. L., Tojeiro, R., Magaña, M. V., Verde, L., Wagner, C., Wake, D. A., Weaver, B. A., Weinberg, D. H., White, M., Xu, X., Yèche, C., Zehavi, I., & Zhao, G.-B. 2012, Monthly Notices of the Royal Astronomical Society, 427, 3435

Beutler, F., Blake, C., Colless, M., Jones, D. H., Staveley-Smith, L., Campbell, L., Parker, Q., Saunders, W., & Watson, F. 2011, Monthly Notices of the Royal Astronomical Society, 416, 3017

Bi, H., Ge, J., & Fang, L.-Z. 1995, The Astrophysical Journal, 452, 90

Blake, C., Kazin, E. A., Beutler, F., Davis, T. M., Parkinson, D., Brough, S., Colless, M., Contreras, C., Couch, W., Croom, S., Croton, D., Drinkwater, M. J., Forster, K., Gilbank, D., Gladders, M., Glazebrook, K., Jelliffe, B., Jurek, R. J., Li, I.-H., Madore, B., Martin, D. C., Pimbblet, K., Poole, G. B., Pracy, M., Sharp, R., Wisnioski, E., Woods, D., Wyder, T. K., & Yee, H. K. C. 2011, Monthly Notices of the Royal Astronomical Society, 418, 1707

Busca, N. G., Delubac, T., Rich, J., Bailey, S., Font-Ribera, A., Kirkby, D., Le Goff, J.-M., Pieri, M. M., Slosar, A., Aubourg, É., Bautista, J. E., Bizyaev, D., Blomqvist, M., Bolton, A. S., Bovy, J., Brewington, H., Borde, A., Brinkmann, J., Carithers, B., Croft, R. A. C., Dawson, K. S., Ebelke, G., Eisenstein, D. J., Hamilton, J.-C., Ho, S., Hogg, D. W., Honscheid, K., Lee, K.-G., Lundgren, B., Malanushenko, E., Malanushenko, V., Margala, D., Maraston, C., Mehta,

K., Miralda-Escudé, J., Myers, A. D., Nichol, R. C., Noterdaeme, P., Olmstead, M. D., Oravetz, D., Palanque-Delabrouille, N., Pan, K., Pâris, I., Percival, W. J., Petitjean, P., Roe, N. A., Rollinde, E., Ross, N. P., Rossi, G., Schlegel, D. J., Schneider, D. P., Shelden, A., Sheldon, E. S., Simmons, A., Snedden, S., Tinker, J. L., Viel, M., Weaver, B. A., Weinberg, D. H., White, M., Yèche, C., & York, D. G. 2013, Astronomy and Astrophysics, 552, A96

Croft, R. A. C., Weinberg, D. H., Katz, N., & Hernquist, L. 1998, The Astrophysical Journal, 495, 44

Eisenstein, D. J. & Hu, W. 1998, The Astrophysical Journal, 496, 605

Eisenstein, D. J., Seo, H.-J., & White, M. 2007, The Astrophysical Journal, 664, 660

Eisenstein, D. J., Zehavi, I., Hogg, D. W., Scoccimarro, R., Blanton, M. R., Nichol, R. C., Scranton, R., Seo, H.-J., Tegmark, M., Zheng, Z., Anderson, S. F., Annis, J., Bahcall, N., Brinkmann, J., Burles, S., Castander, F. J., Connolly, A., Csabai, I., Doi, M., Fukugita, M., Frieman, J. A., Glazebrook, K., Gunn, J. E., Hendry, J. S., Hennessy, G., Ivezić, Z., Kent, S., Knapp, G. R., Lin, H., Loh, Y.-S., Lupton, R. H., Margon, B., McKay, T. A., Meiksin, A., Munn, J. A., Pope, A., Richmond, M. W., Schlegel, D., Schneider, D. P., Shimasaku, K., Stoughton, C., Strauss, M. A., SubbaRao, M., Szalay, A. S., Szapudi, I., Tucker, D. L., Yanny, B., & York, D. G. 2005, The Astrophysical Journal, 633, 560

Hui, L. & Gnedin, N. Y. 1997, Monthly Notices of the Royal Astronomical Society, 292, 27

Kaiser, N. 1987, Monthly Notices of the Royal Astronomical Society, 227, 1

Lewis, A., Challinor, A., & Lasenby, A. 2000, The Astrophysical Journal, 538, 473

Mao, X.-C. & Wu, X.-P. 2008, The Astrophysical Journal Letters, 673, L107

Matsubara, T. 2004, The Astrophysical Journal, 615, 573

McDonald, P. 2003, The Astrophysical Journal, 585, 34

McDonald, P. & Eisenstein, D. J. 2007, Physical Review D, 76, 063009

McDonald, P., Seljak, U., Cen, R., Shih, D., Weinberg, D. H., Burles, S., Schneider, D. P., Schlegel, D. J., Bahcall, N. A., Briggs, J. W., Brinkmann, J., Fukugita, M., Ivezić, Ž., Kent, S., & Vanden Berk, D. E. 2005, The Astrophysical Journal, 635, 761

Meiksin, A., White, M., & Peacock, J. A. 1999, Monthly Notices of the Royal Astronomical Society, 304, 851

Mo, H., van den Bosch, F. C., & White, S. 2010, Galaxy Formation and Evolution (Cambridge University Press)

Norman, M. L., Bryan, G. L., Harkness, R., Bordner, J., Reynolds, D., O'Shea, B., & Wagner, R. 2007, ArXiv e-prints

Padmanabhan, N., Xu, X., Eisenstein, D. J., Scalzo, R., Cuesta, A. J., Mehta, K. T., & Kazin, E. 2012, Monthly Notices of the Royal Astronomical Society, 427, 2132

Peebles, P. J. E. & Yu, J. T. 1970, The Astrophysical Journal, 162, 815

Perlmutter, S., Aldering, G., Goldhaber, G., Knop, R. A., Nugent, P., Castro, P. G., Deustua, S., Fabbro, S., Goobar, A., Groom, D. E., Hook, I. M., Kim, A. G., Kim, M. Y., Lee, J. C., Nunes, N. J., Pain, R., Pennypacker, C. R., Quimby, R., Lidman, C., Ellis, R. S., Irwin, M., McMahon, R. G., Ruiz-Lapuente, P., Walton, N., Schaefer, B., Boyle, B. J., Filippenko, A. V., Matheson, T., Fruchter, A. S., Panagia, N., Newberg, H. J. M., Couch, W. J., & Supernova Cosmology Project. 1999, The Astrophysical Journal, 517, 565

Planck Collaboration, Ade, P. A. R., Aghanim, N., Armitage-Caplan, C., Arnaud, M., Ashdown, M., Atrio-Barandela, F., Aumont, J., Baccigalupi, C., Banday, A. J., & et al. 2013, ArXiv e-prints

Regan, J. A., Haehnelt, M. G., & Viel, M. 2007, Monthly Notices of the Royal Astronomical Society, 374, 196

Rhook, K. J., Geil, P. M., & Wyithe, J. S. B. 2009, Monthly Notices of the Royal Astronomical Society, 392, 1388

Riess, A. G., Filippenko, A. V., Challis, P., Clocchiatti, A., Diercks, A., Garnavich, P. M., Gilliland, R. L., Hogan, C. J., Jha, S., Kirshner, R. P., Leibundgut, B., Phillips, M. M., Reiss, D., Schmidt, B. P., Schommer, R. A., Smith, R. C., Spyromilio, J., Stubbs, C., Suntzeff, N. B., & Tonry, J. 1998, The Astronomical Journal, 116, 1009

Sachs, R. K. & Wolfe, A. M. 1967, The Astrophysical Journal, 147, 73

Slosar, A., Font-Ribera, A., Pieri, M. M., Rich, J., Le Goff, J.-M., Aubourg, É., Brinkmann, J., Busca, N., Carithers, B., Charlassier, R., Cortês, M., Croft, R., Dawson, K. S., Eisenstein, D., Hamilton, J.-C., Ho, S., Lee, K.-G., Lupton, R., McDonald, P., Medolin, B., Muna, D., Miralda-Escudé, J., Myers, A. D., Nichol, R. C., Palanque-Delabrouille, N., Pâris, I., Petitjean, P., Piškur, Y., Rollinde, E., Ross, N. P., Schlegel, D. J., Schneider, D. P., Sheldon, E., Weaver, B. A., Weinberg, D. H., Yeche, C., & York, D. G. 2011, Journal of Cosmology and Astroparticle Physics, 9, 1

Slosar, A., Ho, S., White, M., & Louis, T. 2009, Journal of Cosmology and Astroparticle Physics, 10, 19

Slosar, A., Iršič, V., Kirkby, D., Bailey, S., Busca, N. G., Delubac, T., Rich, J., Aubourg, É., Bautista, J. E., Bhardwaj, V., Blomqvist, M., Bolton, A. S., Bovy, J., Brownstein, J., Carithers, B., Croft, R. A. C., Dawson, K. S., Font-Ribera, A., Le Goff, J.-M., Ho, S., Honscheid, K., Lee, K.-G., Margala, D., McDonald, P., Medolin, B., Miralda-Escudé, J., Myers, A. D., Nichol, R. C., Noterdaeme, P., Palanque-Delabrouille, N., Pâris, I., Petitjean, P., Pieri, M. M., Piškur, Y., Roe, N. A., Ross, N. P., Rossi, G., Schlegel, D. J., Schneider, D. P., Suzuki, N., Sheldon, E. S., Seljak, U., Viel, M., Weinberg, D. H., & Yèche, C. 2013, Journal of Cosmology and Astroparticle Physics, 4, 26

Sunyaev, R. A. & Zeldovich, Y. B. 1970, Astrophysics and Space Science, 7, 3

Weinberg, D. H., Miralda-Escude, J., Hernquist, L., & Katz, N. 1997, The Astrophysical Journal, 490, 564

Weinberg, D. H., Mortonson, M. J., Eisenstein, D. J., Hirata, C., Riess, A. G., & Rozo, E. 2012, ArXiv e-prints

White, M. 2003, in The Davis Meeting On Cosmic Inflation

White, M., Pope, A., Carlson, J., Heitmann, K., Habib, S., Fasel, P., Daniel, D., & Lukic, Z. 2010, The Astrophysical Journal, 713, 383

Zhang, Y., Anninos, P., Norman, M. L., & Meiksin, A. 1997, The Astrophysical Journal, 485, 496

Chapter 5

Conclusion

This thesis presents examples of astrophysical approaches to probing the nature of dark matter and dark energy. There are many dark matter candidates currently proposed, from weakly interacting massive particles (WIMPs), to axions and sterile neutrinos (Feng, 2010). Many of these particle candidates are being targeted with expensive direct and indirect searches, as well astrophysical surveys, with little success. Primordial black holes (PBHs), therefore, as the only non-particle candidate, and one that does not require any physics beyond the Standard Model, deserve increased attention. In Chapter 2 of this thesis we therefore focused on making theoretical predictions for the possibility of constraining a significant portion of the remaining PBH dark matter mass window using the already existing Kepler satellite. We found that the microlensing of Kepler source stars provides for the possibility of constraining up to 40% of the remaining mass range, due to the extreme photometric precision of the telescope, as well as the proximity of the Kepler source stars. This allows for the detection of small mass black holes down to $2 \times 10^{-10} M_\odot$. In Chapter 3 we implemented our formalism in the analysis of the first two years of publicly available Kepler lightcurves. Even though we found many background sources of error which were not accounted for in our predicted sensitivity calculation, we successfully constrained the mass range by a full one

order of magnitude below the previous MACHO/EROS microlensing survey limits (Alcock et al., 1998), down to $2 \times 10^{-9} M_\odot$. No PBH candidate events have been found so far, however we will continue to extend this monitoring of Kepler data for possible microlensing events as it becomes publically available. In addition, we also provided approximations in Chapter 2 for future star selection, as well as predictions for planned missions, such as WFIRST. It seems that with Kepler, and WFIRST, we will be able to close a majority of the window left, however, leaving a full two orders of magnitude not targeted. Short cadence monitoring of stars with improved photometric precision will come upon the backgrounds of stellar flares, which become more prominent at shorter time scales, while monitoring stars farther away becomes increasingly difficult while maintaining this precise photometry. New methods, such as extending the limits from lensing of Gamma Ray Bursts, might therefore have to come into play to address the remaining primordial black hole mass range. The detection or exclusion of PBH dark matter would also provide a powerful indication of early Universe physics, constraining the amplitude of fluctuations allowed during the radiation era or the possibility of multiple periods of accelerated expansion during that time, allowing for PBH production.

The late-time measurements of the accelerated expansion of the Universe are the focus of current dark energy astrophysical surveys. Although many models predict a constant equation of state with $w = -1$, any deviation from this would indicate a departure from the current standard cosmology picture. It is therefore important to track this number over time, with great precision. Measurements of the Cosmic Microwave Background (CMB) at high redshifts, and supernovae at low redshifts, are now being complemented with lensing measurements, and Baryon Acoustic Oscillations (BAO), which can be measured in multiple matter probes over time (Weinberg et al., 2012). Although dark energy is thought to have become dominant at redshifts of 1 and lower, it is important to track the evolution of the Universe at intermediate redshifts as well. 21 cm probes of neutral hydrogen

will thus target matter distribution at redshifts of 12 and lower with future radio telescopes (Wyithe et al., 2007), however currently, the BOSS team is already measuring BAO at redshifts of 2-3 with low resolution quasar spectra (Busca et al., 2013; Slosar et al., 2013). In Chapter 4 we investigated the possible systematic effects of this measurement using full scale hydrodynamic simulations. We have found the location of the peak in the Lyman-alpha forest is a robust measurement of the underlying total matter BAO peak, however we were not able to fully model the shape and size of the peak due to some challenges with the simulations. We have laid out the groundwork for such an analysis with a future simulation which will more accurately model the full initial conditions of the BAO dark matter distribution. Such a full hydrodynamic analysis will be crucial to understanding the uncertainties involved in such a measurement, since the bias and redshift space distortion parameters which are present in the conversion between the flux and dark measurements, are set by the gas physics in the Intergalactic Medium, which can be modeled by just such a simulation. In the future the full modeling of the BAO peak shape will be needed to increase the precision of the BAO measurement in the Lyman-alpha forest. This will especially be true for the continuing BOSS data analysis, as well as the upcoming BigBOSS survey (Schlegel et al., 2011) which will extend the number of quasar absorption lines measured from tens of thousands to millions. The combination of supernovae, BAO, weak lensing, clusters, and CMB will provide powerful insight into dark energy models in the near future. Although the measurements might just provide us with a more precise value of w centered around -1, as we map the matter distribution of the Universe over time with future surveys, such as WFIRST, Euclid, or LSST (Weinberg et al., 2012), we might encounter even further surprises, just like the discovery of dark energy was a mere fifteen years ago.

With such multiple approaches to the measurements of dark energy and dark matter we are continuing to provide new insight into the nature of the other 95% of the Universe.

References

Alcock, C., Allsman, R. A., Alves, D., Ansari, R., Aubourg, É., Axelrod, T. S., Bareyre, P., Beaulieu, J.-P., Becker, A. C., Bennett, D. P., Brehin, S., Cavalier, F., Char, S., Cook, K. H., Ferlet, R., Fernandez, J., Freeman, K. C., Griest, K., Grison, P., Gros, M., Gry, C., Guibert, J., Lachièze-Rey, M., Laurent, B., Lehner, M. J., Lesquoy, É., Magneville, C., Marshall, S. L., Maurice, É., Milsztajn, A., Minniti, D., Moniez, M., Moreau, O., Moscoso, L., Palanque-Delabrouille, N., Peterson, B. A., Pratt, M. R., Prévôt, L., Queinnec, F., Quinn, P. J., Renault, C., Rich, J., Spiro, M., Stubbs, C. W., Sutherland, W., Tomaney, A., Vandehei, T., Vidal-Madjar, A., Vigroux, L., & Zylberajch, S. 1998, The Astrophysical Journal Letters, 499, L9

Busca, N. G., Delubac, T., Rich, J., Bailey, S., Font-Ribera, A., Kirkby, D., Le Goff, J.-M., Pieri, M. M., Slosar, A., Aubourg, É., Bautista, J. E., Bizyaev, D., Blomqvist, M., Bolton, A. S., Bovy, J., Brewington, H., Borde, A., Brinkmann, J., Carithers, B., Croft, R. A. C., Dawson, K. S., Ebelke, G., Eisenstein, D. J., Hamilton, J.-C., Ho, S., Hogg, D. W., Honscheid, K., Lee, K.-G., Lundgren, B., Malanushenko, E., Malanushenko, V., Margala, D., Maraston, C., Mehta, K., Miralda-Escudé, J., Myers, A. D., Nichol, R. C., Noterdaeme, P., Olmstead, M. D., Oravetz, D., Palanque-Delabrouille, N., Pan, K., Pâris, I., Percival, W. J., Petitjean, P., Roe, N. A., Rollinde, E., Ross, N. P., Rossi, G., Schlegel, D. J., Schneider, D. P., Shelden, A., Sheldon, E. S., Simmons, A., Snedden, S., Tinker, J. L., Viel, M., Weaver, B. A., Weinberg, D. H., White, M., Yèche, C., & York, D. G. 2013, Astronomy and Astrophysics, 552, A96

Feng, J. L. 2010, Annual Review of Astronomy and Astrophysics, 48, 495

Schlegel, D., Abdalla, F., Abraham, T., Ahn, C., Allende Prieto, C., Annis, J., Aubourg, E., Azzaro, M., Baltay, S. B. C., Baugh, C., Bebek, C., Becerril, S., Blanton, M., Bolton, A., Bromley, B., Cahn, R., Carton, P. ., Cervantes-Cota, J. L., Chu, Y., Cortes, M., Dawson, K., Dey, A., Dickinson, M., Diehl, H. T., Doel, P., Ealet, A., Edelstein, J., Eppelle, D., Escoffier, S., Evrard, A., Faccioli, L., Frenk, C., Geha, M., Gerdes, D., Gondolo, P., Gonzalez-Arroyo, A., Grossan, B., Heckman, T., Heetderks, H., Ho, S., Honscheid, K., Huterer, D., Ilbert, O., Ivans, I., Jelinsky, P., Jing, Y., Joyce, D., Kennedy, R., Kent, S., Kieda, D., Kim, A., Kim, C., Kneib, J. ., Kong, X., Kosowsky, A., Krishnan, K.,

Lahav, O., Lampton, M., LeBohec, S., Le Brun, V., Levi, M., Li, C., Liang, M., Lim, H., Lin, W., Linder, E., Lorenzon, W., de la Macorra, A., Magneville, C., Malina, R., Marinoni, C., Martinez, V., Majewski, S., Matheson, T., McCloskey, R., McDonald, P., McKay, T., McMahon, J., Menard, B., Miralda-Escude, J., Modjaz, M., Montero-Dorta, A., Morales, I., Mostek, N., Newman, J., Nichol, R., Nugent, P., Olsen, K., Padmanabhan, N., Palanque-Delabrouille, N., Park, I., Peacock, J., Percival, W., Perlmutter, S., Peroux, C., Petitjean, P., Prada, F., Prieto, E., Prochaska, J., Reil, K., Rockosi, C., Roe, N., Rollinde, E., Roodman, A., Ross, N., Rudnick, G., Ruhlmann-Kleider, V., Sanchez, J., Sawyer, D., Schimd, C., Schubnell, M., Scoccimaro, R., Seljak, U., Seo, H., Sheldon, E., Sholl, M., Shulte-Ladbeck, R., Slosar, A., Smith, D. S., Smoot, G., Springer, W., Stril, A., Szalay, A. S., Tao, C., Tarle, G., Taylor, E., Tilquin, A., Tinker, J., Valdes, F., Wang, J., Wang, T., Weaver, B. A., Weinberg, D., White, M., Wood-Vasey, M., Yang, J., Yeche, X. Y. C., Zakamska, N., Zentner, A., Zhai, C., & Zhang, P. 2011, ArXiv e-prints

Slosar, A., Iršič, V., Kirkby, D., Bailey, S., Busca, N. G., Delubac, T., Rich, J., Aubourg, É., Bautista, J. E., Bhardwaj, V., Blomqvist, M., Bolton, A. S., Bovy, J., Brownstein, J., Carithers, B., Croft, R. A. C., Dawson, K. S., Font-Ribera, A., Le Goff, J.-M., Ho, S., Honscheid, K., Lee, K.-G., Margala, D., McDonald, P., Medolin, B., Miralda-Escudé, J., Myers, A. D., Nichol, R. C., Noterdaeme, P., Palanque-Delabrouille, N., Pâris, I., Petitjean, P., Pieri, M. M., Piškur, Y., Roe, N. A., Ross, N. P., Rossi, G., Schlegel, D. J., Schneider, D. P., Suzuki, N., Sheldon, E. S., Seljak, U., Viel, M., Weinberg, D. H., & Yèche, C. 2013, Journal of Cosmology and Astroparticle Physics, 4, 26

Weinberg, D. H., Mortonson, M. J., Eisenstein, D. J., Hirata, C., Riess, A. G., & Rozo, E. 2012, ArXiv e-prints

Wyithe, S., Loeb, A., & Geil, P. 2007, ArXiv e-prints

Appendix A

Derivation of Microlensing Formulas

A.1 Finite-Source with Linear Limb-Darkening Formula

Equation 2.13 can be derived starting with equation 2.12:

$$A_{\text{limb}}(u, U_*) = \left(\int_0^{U_*} 2\pi U'_* I_{\text{b}}(U'_*) dU'_* \right)^{-1} \int_0^{U_*} \frac{\partial (A_{\text{fs}}(u, U'_*) \pi U'^2_*)}{\partial U'_*} I_{\text{b}}(U'_*) dU'_*. \quad \text{(A.1)}$$

The first integrand can then be evaluated as follows:

$$
\begin{aligned}
\int_0^{U_*} 2\pi U'_* I(U'_*) dU'_* &= \pi U'^2_* I(U'_*) \mid_0^{U_*} - \int_0^{U_*} \pi U'^2_* \frac{\partial I(U'_*)}{\partial U'_*} dU'_* \\
&= \pi U_*^2 (1 - u_\lambda) + \pi u_\lambda \frac{1}{U_*} \int_0^{U_*} \frac{U'^3_*}{\sqrt{U_*^2 - U'^2_8}} dU'_* \\
&= \pi U_*^2 (1 - u_\lambda) + \frac{2}{3} \pi u_\lambda U_*^2 \\
&= \pi U_*^2 \left(1 - \frac{1}{3} u_\lambda \right). \quad \text{(A.2)}
\end{aligned}
$$

The second integrand, as stated in the text, has a peak at $u = U'_*$, which causes problems with convergence when integrating numerically. However, by correctly treating the integral boundaries, we can omit this problem by the following

$$\int_0^{U_*} \frac{\partial A_{\text{fs}}(u, U'_*)\pi U'^2_*}{\partial U'_*} I(U'_*) dU'_* = A_{\text{fs}} \pi U^2_*(1 - u_\lambda)$$

$$+ \pi u_\lambda \frac{1}{U_*} \int_0^{U_*} A_{\text{fs}}(u, U'_*) \frac{U'^3_*}{\sqrt{U^2_* - U'^2_*}} dU'_* \quad \text{(A.3)}$$

with the substitution of $U'^2_* = U^2_* - z^2$ and $2U'_* dU'_* = -2z dz$

$$\int_0^{U_*} A_{\text{fs}}(u, U'_*) \frac{U'^3_*}{\sqrt{U^2_* - U'^2_*}} dU'_* = \int_0^{U_*} A_{\text{fs}}(u, \sqrt{U^2_* - z^2})(U^2_* - z^2) dz. \quad \text{(A.4)}$$

This expression removes the problem of numerical convergence. Putting the two integrands together, we arrive at equation 2.13:

$$A_{\text{limb}}(u, U_*) = \left(\pi U^2_*(1 - u_\lambda/3)\right)^{-1} \times$$

$$\left[A_{\text{fs}}(u, U_*)\pi U^2_*(1 - u_\lambda) + (\pi u_\lambda/U_*) \int_0^{U_*} A_{\text{fs}}(u, \sqrt{U^2_* - z^2})(U^2_* - z^2) dz \right]. \quad \text{(A.5)}$$

.

A.1.1   Maximum Magnification for a Finite-Source Linear Limb-Darkening Model

In order to derive A_{max} in Equation 2.16, we start with

$$A_{\text{fs}}(0, U_*) = \frac{\sqrt{4 + U^2_*}}{U_*} \quad \text{(A.6)}$$

and, following the above derivation for the second integrand,

$$A_{\text{fs}}(0, U_*)\pi U^2_*(1 - u_\lambda) = \pi U_* \sqrt{4 + U^2_*}(1 - u_\lambda), \quad \text{(A.7)}$$

while,

$$\int_0^{U_*} A_{\text{fs}}(0, \sqrt{U_*^2 - z^2})(U_*^2 - z^2)dz = \int_0^{U_*} \frac{\sqrt{4 + U_*^2 - z^2}}{\sqrt{U_*^2 - z^2}}(U_*^2 - z^2)dz$$

$$= \int_0^{U_*} \sqrt{U_*^2 - z^2}\sqrt{4 + U_*^2 - z^2}dz$$

$$= \frac{2}{3}\sqrt{4 + U_*^2}\left[(2 + U_*^2)\,E[\sqrt{U_*^2/(4 + U_*^2)}]\right.$$

$$\left. -2K[\sqrt{U_*^2/(4 + U_*^2)}]\right]. \tag{A.8}$$

Putting the expressions together we arrive at,

$$A_{\max} = A_{\text{limb}}(0, U_*)$$

$$= \frac{A_{\max_{\text{fs}}}}{1 - u_\lambda/3}$$

$$\times \left\{1 - u_\lambda + (2u_\lambda/3U_*^2)\left[(2 + U_*^2)E\left[\sqrt{U_*^2/(4 + U_*^2)}\right]\right.\right.$$

$$\left.\left. - 2K\left[\sqrt{U_*^2/(4 + U_*^2)}\right]\right]\right\}. \tag{A.9}$$

A.2 Derivation of the Expression for the Number of Expected Events

We can derive the differential event rate used in Equation 2.18 following the setup in (Griest, 1991). We assume a Maxwellian velocity distribution of dark matter:

$$f(v)d^3v = e^{-v^2/v_c^2}\frac{1}{\pi^{3/2}v_c^3}d^3v, \tag{A.10}$$

with $v_c \approx 220$ km/s. Then the differential rate of detection is just the flux of primordial black holes (PBHs) through the microlensing tube (as defined in (Griest, 1991)):

$$d\Gamma = \frac{nd^3x}{dt}f(v)d^3v, \tag{A.11}$$

where $n = \rho/M$ is the number density of PBHs, $d^3x = v_t \cos\theta dt dS$ is the cylindrical segment of the microlensing tube through which the PBH passes, $dS = u_{\mathrm{thresh}} r_{\mathrm{E}}(x) d\alpha L dx$ is the surface element of the microlensing tube with L being the distance from the observer to the source star, x the ratio of the distance to the lens with respect to L, and α running from 0 to 2π, while $f(v)d^3v = f(v)v_t dv_x dv_t d\theta$ is the distribution of PBH velocities in cylindrical coordinates. θ here is the angle between the normal to the surface element dS and the transverse velocity of the PBH. We thus obtain the expression:

$$d\Gamma = \frac{\rho u_{\mathrm{thresh}} r_{\mathrm{E}}(x)}{\pi M} \frac{v_t^2}{v_c^2} e^{-v_t^2/v_c^2} \cos\theta dv_t d\theta d\alpha L dx. \tag{A.12}$$

Finally, integrating over α and performing a change of variables where $\cos\theta = \sqrt{1 - u_{\mathrm{min}}^2/u_{\mathrm{thresh}}^2}$ with the variables defined as in the text,

$$d\Gamma = 4 r_{\mathrm{E}}(x) L \frac{\rho}{M} \frac{v_t^2}{v_c^2} e^{-v_t^2/v_c^2} dv_t du_{\mathrm{min}} dx. \tag{A.13}$$

A.3 Derivation of the Approximation for Future Star Selection

We can derive the approximation for future star selection for the small primordial black hole masses (PBHs), starting with Equation 2.17

$$\frac{d\Gamma}{dt_{\mathrm{event}}} = \frac{\rho}{M} L v_c^2 \int_0^{x_{\mathrm{max}}} dx \beta'^2 g(\beta'). \tag{A.14}$$

For small PBHs on the order of $10^{-10} M_\odot$, the projected star radius dominates the lightcurve. Therefore we can make the approximation that $u_{\mathrm{thresh}} \approx U_*$. Also, for dwarf stars, whenever $R_*/R_\odot < 0.57 \left(t_{\mathrm{event}}/1hr\right)\left(v_c/220km/s\right)/x_{\mathrm{max}}$, one can approximate $\beta < 1$ and $\beta^2 g(\beta) \approx (3/8)\pi\beta^2$. This leaves us with the expression:

$$\frac{d\Gamma}{dt_{\mathrm{event}}} = \frac{\rho}{M} L v_c^2 \int_0^{x_{\mathrm{max}}} dx \frac{3}{8}\pi\beta^2. \tag{A.15}$$

Since now $\beta = 4r_{\mathrm{E}}^2 u_{\mathrm{thresh}}^2/(t_{\mathrm{event}}^2 v_c^2) \approx 4x^2 R_*^2/(t_{\mathrm{event}}^2 v_c^2)$, we have

$$\frac{d\Gamma}{dt_{\mathrm{event}}} = \frac{6}{5}\pi \frac{\rho}{M} \frac{1}{v_c^2} \frac{R_*^4}{t_{\mathrm{event}}^4} x_{\mathrm{max}}^5 L. \tag{A.16}$$

Integrating over t_{event} from the minimum microlensing time detectable, t_{min} to infinity,

$$\frac{d\Gamma}{dt_{\mathrm{event}}} = \frac{2}{5}\pi \frac{\rho}{M} \frac{1}{v_c^2} \frac{R_*^4}{t_{\mathrm{min}}^5} x_{\mathrm{max}}^5 L. \tag{A.17}$$

For these small PBHs, we know that $x_{\mathrm{xmax}} < 1$, so we can estimate $x_{\mathrm{xmax}} \approx 4GMLU_*^2/(R_*^2 c^2)$, arriving at Equation 2.25

$$\Gamma \approx 409.6\pi \frac{G^5 M^4 \rho}{c^{10} v_c^2} \frac{U_{*\mathrm{max}}^{10}}{t_{\mathrm{min}}^3} \frac{L^6}{R_*^6}. \tag{A.18}$$

Additionally, using the values of $\rho \approx 0.3$ GeV cm^{-3} and $v_c \approx 220$ km/s, as well as $U_{*\mathrm{max}} = 2/\sqrt{A_{thresh}^2 - 1}$, we arrive at Equation 2.26:

$$\Gamma \approx 2.63 \times 10^{20} \left(\frac{L}{1\mathrm{kpc}}\right)^6 \left(\frac{R_\odot}{R_*}\right)^6 \left(\frac{M}{M_\odot}\right)^4 \left(\frac{1\mathrm{hr}}{t_{\mathrm{min}}}\right)^3 \frac{1}{(A_{\mathrm{thresh}}^2 - 1)^5} \frac{1}{\mathrm{year}}. \tag{A.19}$$

References

Griest, K. 1991, The Astrophysical Journal, 366, 412